2013

ELECTRON TRANSPORT IN LOW-DIMENSIONAL NANOSTRUCTURES - THEORETICAL STUDY WITH APPLICATION

Xiaoliang Zhong
Michigan Technological University

ELECTRON TRANSPORT IN LOW-DIMENSIONAL NANOSTRUCTURES – THEORETICAL STUDY WITH APPLICATION

By

Xiaoliang Zhong

A DISSERTATION

Submitted in partial fulfillment of the requirements for the degree of

DOCTOR OF PHILOSOPHY

In Physics

MICHIGAN TECHNOLOGICAL UNIVERSITY

2013

This dissertation has been approved in partial fulfillment of the requirements for the Degree of DOCTOR OF PHILOSOPHY in Physics.

Department of Physics

Dissertation Advisor: *Dr. Ravindra Pandey*

Committee Member: *Dr. Donald Beck*

Committee Member: *Dr. Loredana Valenzano*

Committee Member: *Dr. Max Seel*

Department Chair: *Dr. Ravindra Pandey*

Contents

List of Figures

x

List of Tables

Preface

This thesis is submitted in partial fulfillment of the requirements for Degree of Doctor of Philosophy in Physics. It includes work performed during my Ph.D. study. My advisor on the research projects is Ravindra Pandey.

In my Ph.D. study, I have worked on applying density functional theory methods in calculating electronic properties of graphene-related materials and bio-sensors.

In the first project I investigated the effect of single-atom doping on the electronic transport properties of C_{60} fullerene[1]. This project was proposed by Dr. Kah Chun Lau, our former group member. I did the modeling and performed the calculations. My advisor guided me doing the calculations and analysis. Dr. Shashi P. Karna from US Army Research Laboratory and my advisor wrote the paper. Dr. Alexandre Reily Rocha gave me valuable suggestion in applying the calculation methods. Chapter 3 is about this work and is reprinted with permission from (The Journal of Physical Chemistry Letters, 1, 1584 (2010)). Copyright (2010) American Chemical Society.

In the next project I studied the effect of strain on a graphene-BN bilayer system[2]. This project was proposed by Dr. Yoke Khin Yap, a professor in my department. I did the modeling and performed the calculations. My advisor helped me doing the analysis and wrote the paper. Chapter 5 is about this work and is reprinted with permission from (Physical Review B, 83, 193403 (2011)). Copyright (2011) American Physical Society.

Then I moved to studying the stacking dependent electronic structure and transport properties of bilayer graphene nanoribbons[3]. This project was proposed by Dr. Ranjit Pati, a professor in my department. I did the modeling and performed the calculations. My advisor and Dr. Karna helped me doing the analysis. I wrote part of the paper and my advisor wrote part of it. Chapter 4 is about this work and is reprinted with permission from (Carbon, 50, 784 (2012)). Copyright (2012) Elsevier.

After that, I focused on the electronic structure and quantum transport properties of trilayers formed from graphene and boron nitride[4]. This project was proposed by Dr. Ralph Scheicher, an assistant professor in Department of Physics and Astronomy, Uppsala University. I did the modeling and performed part the calculations. Dr. Rodrigo G. Amorim, my colleague, performed part the calculations. I, Rodrigo, my advisor and Dr. Karna did the analysis together. I wrote part of the paper and my advisor wrote part

of it. Chapter 6 is about this work and is reprinted with permission from (Nanoscale, 4, 5490 (2012)). Copyright (2012) The Royal Society of Chemistry.

Later I turned to studying the interaction of nucleobases with silicon nanowires[5]. This project was proposed by Dr. Craig Friedrich, a professor in Department of Mechanical Engineering and Multi-Scale Technologies Institute, Michigan Technological University. I and William J. Slough, my colleague, did the modeling and performed the calculations together. My advisor and William J. Slough helped me doing the analysis. I wrote part of the paper and my advisor wrote part of it. Chapter 7 is about this work and is reprinted with permission from (Chemical Physics Letters, 553, 55 (2012)). Copyright (2012) Elsevier.

Acknowledgments

I thank Prof. Ravindra Pandey, my PhD advisor. I am very lucky to be able to work with him. He always supports me as his student. He has given me energy, promoting me from the ground state to an excited state. He has taught me a lot of things, not only in research but also in personal life. I have learnt from him that happiness is important. Sometimes I would think he is pushing me too hard, but every time I improve myself in this way. And I also thank Mrs. Aparna Pandey, my advisor's wife. She has invited the students including me several times to their house, eating together. This helps me feel at ease.

Thanks to Prof. Donald Beck, Prof. Loredana Valenzano and Prof. Max Seel for being my advisory committee members and giving me helpful advice in my study and research.

Thanks to Prof. Yoke Khin Yap. He is glad to share with me his insights from experiment, which helps me make my research work more realistic.

Thanks to Prof. Ralph Scheicher, Prof. Qiang Sun, Prof. Craig Friedrich, Wil Slough, Rodrigo Amorim and Radhakrishnan Balu, my collaborators. I wonder how much work I could have done without the collaboration with them.

Thanks to Dr. Haiying He. I could not be at Michigan Tech now but for her help. When I first came to Houghton, she gave me detailed help in both life and research.

Thanks to Chunhui Liu and Saikat Mukhopadhyay, my colleagues. Chunhui is a chemist, who helped me understand some physics in terms of chemistry. Saikat is a biologist. We usually learn from each other by arguing. And Dr. S. Gowtham, our former group member. He is very helpful in solving my computational problems.

Thank my parents for giving me life. They are too selfless to me. No matter at what time and under what circumstances, they support me. I thank my brother, who is 13 years older than me. He always gives me valuable advice when I feel confused.

Finally, I thank my wife, Dongwei Xu. We find support from each other. I feel relaxed to be with her. She has helped me in many aspects, from swimming to driving, from inserting an equation in a document to cooking. And, she is a good friend.

Abstract

Graphene as a carbon monolayer has attracted extensive research interest in recent years. My research work within the frame of density functional theory has suggested that positioning graphene in proximity to h-BN may induce a finite energy gap in graphene, which is important for device applications. For an AB-stacked graphene/BN bilayer, a finite gap is induced at the equilibrium configuration. This induced gap shows a linear relationship with the applied strain. For a graphene/BN/graphene trilayer, a negligible gap is predicted in the ground state due to the overall symmetry of the system. When an electric field is applied, a tunable gap can be obtained for both AAA and ABA stackings.

Enhanced tunneling current in the AA-stacked bilayer nanoribbons is predicted compared to either single-layer or AB-stacked bilayer nanoribbons. Interlayer separation between the nanoribbons is shown to have a profound impact on the conducting features. The effect of boron or nitrogen doping on the electronic transport properties of C_{60} fullerene is studied. The BC_{59} fullerene exhibits a considerably higher current than the pristine or nitrogen doped fullerenes beyond the applied bias of 1 V, suggesting it can be an effective semiconductor in p-type devices.

The interaction between nucleic acid bases - adenine (A), guanine (G), cytosine (C), thymine (T) and uracil (U) - and a hydrogen-passivated silicon nanowire (SiNW) is investigated. The binding energy of the bases with the SiNW shows the order: G > A~C~T~U. This suggests that the interaction strength of a hydrogen passivated SiNW with the nucleic acid bases is nearly the same-G being an exception. The nature of the interaction is suggested to be electrostatic.

Chapter 1   Introduction

In this section I will talk about the background of my PhD research work at Michigan Tech. In my PhD program I have been primarily doing research on two material species, i.e., graphene related materials and silicon nanowire-based biosensors. Most of the research work was done by employing density functional theory (DFT) and non-equilibrium Green's function (NEGF) methods. In the first part the idea is to find a way to induce a finite energy gap in graphene, which is gapless in the pristine form. To achieve this goal, I have virtually designed hybrid-layered structures formed from graphene and h-BN (hexagonal boron nitride), as well as engineering graphene strips which are essentially one-dimensional (1D) structures. The research goal of the second part was to understand the biosensing mechanism of silicon nanowires with respect to DNA/RNA nucleic bases.

1.1 Graphene related materials

Graphene is a two-dimensional monoatomic layer system which has attracted great research interest due to its remarkable electronic properties [6-8]. For example, the electron mobility of graphene can reach as high as 10^6 cm^2/Vs at room temperature, which is about 70 times higher than that of silicon[9]. This high electron mobility, combined with the ability to well integrate with other materials, makes graphene a promising material for high-frequency analogue electronics[9]. A pristine graphene monolayer can be cut into elongated strips to form 1D structures, referred to as graphene nanoribbons (GNR) which can be terminated by either armchair or zigzag edges. GNRs can be either metallic or semiconducting depending on the type and width of edges [10]. Recently, the stability of edge states and edge magnetism in graphene nanoribbons were discussed, arguing that the intrinsic magnetism of GNRs may not be stable at room temperature [11].

Graphene's honeycomb lattice can be described in terms of a sp^2 hybridized network of carbon atoms. Being a single-atom-thick layer, the ideal 2D graphene is a zero-gap semiconductor, with electronic valence and conduction bands associated with π and π^*

bands derived from the p_z-orbitals crossing at Dirac points in the reciprocal space[6]. On the other hand, the practical realization of a graphene-based switchable device, such as a transistor, depends on the availability of a semiconducting graphene. Since the absence of a gap is directly linked to the equivalence of the two carbon sublattices in graphene, removing this equivalence can lead to a gap being opened, changing the electronic properties of graphene. The opening of the gap in graphene can be achieved in a number of ways, e.g., through doping[12,13], edge functionalization[14] and chemical composition of the substrate[15-17]. In recent years, considerable efforts have been made to find approaches for developing an electrically tunable band gap in graphene[18].

Positioning graphene in proximity to hexagonal boron nitride (h-BN), which has lattice constant similar to graphene but distinguishable sublattices consisting of boron and nitrogen atoms, has been suggested as a suitable way to introduce inequivalence in the graphene lattice and thus open a gap. A gap of 53 meV was predicted for graphene deposited on h-BN substrate[17]. The hybrid graphene/BN bilayer also shows the band gap tunability in the presence of strain or electric field[2,19-21]. Nevertheless, some of the experimental[22,23] and theoretical[24] investigations have shown that graphene on the bulk BN substrate behaves like a suspending zero-gap material. These contrasting observations can be understood in terms of a competition between the induced intraplanar strains and the interfacial interactions for the graphene/BN system. For example, lattice constants of graphene and a BN monolayer match with each other in a bilayer superlattice[25], while difference in the lattice constants of the graphene and the bulk BN substrate[22,24] is about 1.6%. If graphene should comply with the lattice of (invariable) BN substrate, the strain-induced energy penalty in graphene is likely to be relatively large which will keep two carbon sublattices globally symmetric yielding zero-gap. For the case of a bilayer superlattice, on the other hand, both graphene and BN compromise to match the lattice constant with each other forming the so-called 'commensurate' bilayer configuration, and the relatively small strain induced energy penalty can be thoroughly compensated by the interlayer binding[25] leading to globally asymmetric carbon sublattices of graphene.

Another carbon allotrope is represented by fullerene, which can work as molecular nanoscale electronic devices[26]. Experimental and theoretical studies aimed at

understanding the underlying physics of molecular and nanoelectronic devices[27,28] have begun to shed light on electron transport mechanisms through molecules and engineered nanomaterials and help identifying appropriate molecular and nano-scale architectures for effective functional elements in electronic devices. Among others, carbon fullerene is one of the most stable and well-known nano-scale molecular structures. Furthermore, its structure and electron transport properties have been the subject of extensive studies for its potential applications as spin valves[29,30] and electro-mechanic amplifiers[31] to name just a couple. Carbon fullerenes are composed of a sheet of linked hexagonal rings separated by pentagonal (sometimes heptagonal) rings that help curve the structure into a spherical empty cage. By far the most common one is the Buckminster fullerene, C_{60}, discovered accidently at Rice University in the late 1980's[32]. It has a high symmetry of icosahedra I_h in which all the C atoms are equivalent with sp^2 hybridization. C_{60}, however, does not exhibit "superaromaticity", i. e. the electrons in the hexagon rings do not delocalize over the molecule. Therefore C_{60} often acts as a semiconductor quantum dot with an energy gap of about 1.5 eV[33].

1.2 Silicon nanowire-based biosensors

Silicon is the second most abundant element in the Earth's crust and dominates the modern industry. Silicon nanowires (SiNWs), with a diameter of ~10 nm are an interesting family of one-dimensional nanoscale materials[34] which can be seamlessly coupled with existing devices based on silicon [35]. Furthermore, the size and doping level of SiNWs can easily be controlled during the synthesis process [34,36,37], making them an attractive host material for the next generation of sensing devices at nanoscale [38-41]. The central idea is that a change in conductivity can be detected as a response to a variation of surface electric potential [42-44]. This scheme enables sensing applications of SiNW based field-effect transistors since the change in electric potential induced by the binding of a target molecule to the surface of the semiconducting substrate is analogous to a change in the applied gate voltage.

Chapter 2   Theoretical Methods

2.1 Density functional theory

2.1.1 Overview

Density functional theory (DFT) is a quantum mechanical theoretical method represented as a computational approach to study the electronic structure of many-body systems. DFT can describe the ground-state properties of materials. It is widely used in physics, chemistry and materials science. DFT has been applied to the studies of bulk, surfaces, molecules and atoms. Within this theory, the properties of materials can be determined by their electron density. DFT has been widely used in simulations in solid-state physics since the 1970s. Nevertheless, DFT was only considered to be accurate enough for quantum chemistry calculations after the 1990s when the exchange and correlation functionals were greatly refined. In many cases calculations based on DFT can give results in reasonable agreement with experimental values. On the other hand, DFT is not as computationally expensive as the traditional Hartree-Fock theory which is based on many-electron wavefunctions[45].

Although DFT calculations have achieved great success, it has intrinsic limitations which at the moment include describing intermolecular interactions (van der Waals (vdW) forces), excited states, transition states, strongly-correlated systems, and accurate estimation of band gaps of semiconductors. As such, modifications on the exchange-correlation functional[46,47] or methods beyond ground-state treatment[48]   are being developed.

2.1.2 The method

The tenet of DFT is based on the two Hohenberg-Kohn (H-K) theorems. The first Hohenberg and Kohn theorem states that, for non-degenerate ground states, the external potential is determined, to within an additive constant, by the electron density[49]. In this way the N-electron many-body problem with 3N spatial coordinates is reduced to a

problem with 3 spatial coordinates. The second H-K theorem states that the ground state total energy can be obtained variationally. The electron density minimizing the total energy corresponds to the exact ground-state density.

Within the framework of Kohn-Sham DFT (KS DFT)[50], the interacting electron problem is reduced to a tractable non-interacting electron problem in an effective potential. For a non-interacting system, the wavefunction can be written as a Slater determinant of atomic orbitals. This effective potential includes the external potential and the Coulomb potential, e.g, the exchange and correlation effects. The major difficulty in KS DFT is the modeling of the exchange and correlation interactions. Local density approximation (LDA) is the simplest yet widely used approximation, which is usually derived from a uniform electron gas model[51].

In the Born–Oppenheimer approximation[52], the nuclei are kept frozen. The electrons then feel a static external potential V. The wavefunction of the N-electron $\Psi(\vec{r}_1, \ldots, \vec{r}_N)$ satisfies the time-independent Schrödinger equation

$$\hat{H}\Psi = [\hat{T}+\hat{V}+\hat{U}]\Psi = [\sum_i^N -\frac{\hbar^2}{2m}\nabla_i^2 + \sum_i^N V(\vec{r}_i) + \sum_{i<j}^N U(\vec{r}_i,\vec{r}_j)]\Psi = E\Psi \quad , \quad (2.1)$$

Where $\hat{T}$ is the kinetic energy, $\hat{V}$ is the potential energy due to the positively charged nuclei, $\hat{U}$ is the lectron-electron interaction energy. $\hat{T}$ and $\hat{U}$ are universal for any N-electron system while $\hat{V}$ is system dependent. Due to the $\hat{U}$ term this many-body equation can not be separated into single-particle equations.

Alternatively, KS DFT can turn the many-body problem with $\hat{U}$ to a single-electron problem without $\hat{U}$. The key element in the KS DFT method is the electron spatial density $n(\vec{r})$,

$$n(\vec{r}) = N\int d^3r_2 \int d^3r_3 \ldots \int d^3r_N \Psi^*(\vec{r}, \vec{r}_2, \ldots, \vec{r}_N)\Psi(\vec{r}, \vec{r}_2, \ldots, \vec{r}_N). \quad (2.2)$$

In principle, for a given ground-state electron density $n_0(\vec{r})$, it is possible to calculate the corresponding ground-state wavefunction $\Psi_0(\vec{r}_1, \vec{r}_2, \ldots, \vec{r}_N)$. Thus, all properties of the system related to electrons are functional of $n_0(\vec{r})$. Therefore, for an electron distribution $n(\vec{r})$, the expectation value of the total energy is

$$E = E[n] = < \Psi[n] \mid \hat{T} + \hat{V} + \hat{U} \mid \Psi[n] > . \tag{2.3}$$

Among the three terms $\hat{T}$ and $\hat{U}$ are universal, while the energy related to $\hat{V}$ can be written as

$$E_v[n] = \int V(\vec{r}) n(\vec{r}) d^3 r . \tag{2.4}$$

The variational minimization of the total energy yields the ground-state density $n_0(\vec{r})$.

The Kohn-Sham equation of the non-interacting system is

$$[-\frac{\hbar^2}{2m} \nabla^2 + V_s(\vec{r})] \phi_i(\vec{r}) = \varepsilon_i \phi_i(\vec{r}) . \tag{2.5}$$

where V_s is the effective potential, while the density is given by

$$n(\vec{r}) = \sum_i^N \mid \phi_i(\vec{r}) \mid^2 . \tag{2.7}$$

In detail,

$$Vs(\vec{r}) = V(\vec{r}) + \int \frac{e^2 n_s(\vec{r}')}{\mid \vec{r} - \vec{r}' \mid} d^3 r' + V_{xc}[n_s(\vec{r})] , \tag{2.8}$$

where the first term is the external potential (including that of the nuclei), the second term is the Hartree energy, the third term is the exchange-correlation (XC) energy. This last term XC accounts for all the many-body effects originating from identical particles (Fermions), and it has no classic counterpart. The KS equation can be solved iteratively.

The simplest approximation to the XC energy is the local density approximation (LDA). Mathematically, the corresponding XC energy only depends on the local density $n(\vec{r})$:

$$E_{XC}^{LDA}[n] = \int \varepsilon_{XC}(n)n(\vec{r})d^3r .$$

(2.9)

Generalized gradient approximation[53] (GGA) takes into account the gradient of density,

$$E_{XC}^{GGA}[n] = \int \varepsilon_{XC}(n, \vec{\nabla}n)n(\vec{r})d^3r .$$

(2.10)

In general, GGA can yield good results for molecular geometries and ground-state energies. Including a component of the exact XC energy calculated by Hartree-Fock method[54] (the hybrid functionals) we can better evaluate the XC energy.

2.1.3 Pseudopotential

In the pseudopotential (PP) approach, the total energy of the ground state is given as,

$$E_{tot} = T + E_{ion}\{\rho^v\} + E_{ee}\{\rho^v\} + E_{xc}\{\rho^v\} ,$$

(2.11)

where the various terms represent the kinetic energy, the coulomb interaction of the ions with the valence electrons (in the form of PP), the valence electrons with the valence electrons, and the exchange and correlation energy, respectively. The core contribution is completely neglected.

Specifically, these potential terms are,

$$E_{ion} = \int V^{PS}(\vec{r})\rho^v(\vec{r})d^3r ,$$

(2.12a)

$$E_{ee} = \frac{1}{2}\int \frac{\rho^v(\vec{r}')\rho^v(\vec{r})}{|\vec{r}' - \vec{r}|}d^3r'd^3r ,$$

(2.12b)

$$E_{xc} = \int \varepsilon_{xc}[\rho^v(\vec{r})]\rho^v(\vec{r})d^3r .$$

(2.12c)

All interactions between core and valence electrons, including Coulomb and exchange correlation interactions, are transferred to the pseudopotential, V^{PS}. The application of pseudopotential method in fact implies a linearization of these interactions, i.e., the corresponding potential energy is proportional to the (local) valence electron density. However, while Coulomb interactions are linear, exchange interactions are explicitly non-linear. If the core and valence electron densities are spatially well separated, this linearization would not induce any serious errors. On the other hand, if there is significant overlap between core and valence electrons, the linearization of exchange interaction will lead to systematic error in the calculated total energy.

2.2 Electronic transport theory

Section 2.2.1, section 2.2.3 and section 2.2.4 are digested from a book written by Supriyo Datta[55].

2.2.1 Preliminary concepts

2.2.1.1 Two-dimensional electron gas (2-DEG)

One kind of mesoscopic conductor is based on n-type GaAs – intrinsic AlGaAs ($Al_xGa_{1-x}As$) heterojunction, forming a thin 2D conducting layer (~100 Å) at the interface. The band gaps of intrinsic GaAs and intrinsic AlGaAs are 1.43 eV and 1.43-2.16 eV, respectively. Due to bands bending, the Fermi level lies inside the conduction band at the interface, inducing electrons sharply peaked near the interface – a good 2D electron gas (**2-DEG**). The donor atoms in the AlGaAs layer and the conduction electrons are spatially separated (modulation-doping), leading to a large mobility. The carrier density is about $2\times10^{11}/cm^2$ to $2\times10^{12}/cm^2$.

This 2-DEG features an extremely low scattering rate. The mobility μ, defined as the ratio of the drift velocity to the electric field, provides a direct measure of the momentum relaxation time as limited by impurities and defects. Mobility measurement using the Hall effect is a basic characterization tool for semiconducting films. The momentum relaxation time is calculated as

$$\tau_m = \frac{\mu m}{|e|}.$$ (2.13)

One compromise: a pristine semiconductor has higher mobility but fewer conduction electrons, while a doped semiconductor has smaller mobility but more conduction electrons.

Electronic conduction in semiconductors takes place either by electrons in the conduction band or holes in the valence band. In mesoscopic system experiments, electron flow usually dominates.

2.2.1.2 Effective mass and density of states

In GaAs-AlGaAs heterostructures at low electric field, a single-band effective mass equation is usually adequate to describe the electron dynamics in conduction band. The effect of periodic lattice potential is incorporated in the effective mass m. Electrons in a 2-DEG can move freely in the xy plane but not in the z direction. The confinement along z induces discrete subbands with different cutoff energies. Usually in semiconductors at low temperatures only the lowest subband is occupied. In contrast, in a 10 nm thick metallic film due to the high electron density tens of subbands are occupied and it is more like a 3D conductor. The following single-(sub)band effective mass equation describes the dynamics of electrons in a 2-DEG.

$$[E_s + \frac{(i\hbar\nabla + eA)^2}{2m} + U(x, y)]\Psi(x, y) = E\Psi(x, y),$$ (2.14)

where E_s is the cut-off energy of the lowest sub-band, A is the vector potential, m is the effective mass of electron. The discontinuity of bands at interface is incorporated into E_s. If U is constant, the wave functions along x and y are just plane waves. A typical value of the effective mass of GaAs is 0.07 (times the free electron mass), if we assume U=0 (2-DEG) then the two-dimensional density of states is constant for all energies exceeding the subband cut-off E_s, approximately $2.9\times10^{10}/(cm^2\ meV)$.

If further in the y direction there is some confinement potential, the energies will be also quantized in y. Consider a rectangular conductor, the thickness (in z direction) is very small, say 5-10 nm. Then the z-subbands are far apart, about 100 meV. The confinement in the y direction is relatively weak so the corresponding subband spacing is quite small. In this chapter we assume that under normal conditions only the lowest z subband is occupied while a number of y subbands are occupied, which are referred to as transverse modes.

One can talk about Fermi energy (E_f) only for a system at equilibrium, and electrons fill in the available states according to Fermi distribution. Away from equilibrium, quasi-Fermi level (F_n) is appropriate which can be position dependent and states group dependent (such as electrons and holes). There are two limits of electron distribution inside the band ($E > E_s$) for the single band model described above. One is the high temperature limit (non-degenerate limit), i.e., $\exp[E_s-E_f]/k_BT \gg 1$. The occupation possibility at E_s is much smaller than one. Another is the low temperature limit (degenerate limit), i.e., $\exp[E_s-E_f]/k_BT \ll 1$. In the low temperature limit, the Fermi distribution function can be simplified to a step function, and the occupation possibility at E_s is almost one. Note at non-zero Kelvin, E_f is not the highest occupied energy, and when temperature increases E_f slightly decreases. 300 K ~ 26 meV. In this chapter we will mainly talk about degenerate conductors.

At low temperatures the conductance is determined entirely by electrons with energy close to Fermi energy. The wavenumber of such electrons is referred to as the Fermi wavenumber (k_f):

$$E_f - E_s = \frac{\hbar^2 k_f^2}{2m}. \tag{2.15}$$

Since E_s is the cut-off energy of the lowest band and we assume U=0 (see, single-band effective mass equation), E_f-E_s is the kinetic energy of electrons at Fermi level. The Fermi wavenumber of a 2D degenerate conductor at equilibrium can be calculated as

$$k_f = \sqrt{2\pi n_s} ,$$ (2.16)

where n_s is the equilibrium electron density per unit area. Note $k_f \sim \sqrt{n_s}$.

2.2.1.3 Characteristic lengths

A conductor usually shows ohmic behavior if its dimensions are much larger than certain characteristic lengths, namely, the de Broglie wavelength λ_f, the mean free path L_m and the phase-relaxation length L_ϕ. Using equation (2.16), the de Broglie wavelength is

$$\lambda_f = \sqrt{2\pi / n_s} .$$ (2.17)

For an electron density of $n_s = 5 \times 10^{11}/cm^2$ (2-DEG), λ_f is about 35 nm.

An electron in a perfect crystal moves as if it were in vacuum but with an effective mass. When impurities, lattice vibrations (phonons) and other electrons lead to 'collisions' the electron is scattered from one state to another, losing its initial momentum. The mean free path L_m and momentum relaxation time τ_m (the average time in which an electron loses its original momentum) are related as

$$L_m = v_f \tau_m .$$ (2.18)

For instance, if $n_s = 5 \times 10^{11}/cm^2$ and we assume the momentum relaxation time is 100ps, $L_m = 30 \ \mu m$.

Suppose initially we have a beam of electrons, and at some point the electrons are separated into two beams, each moving along a separate path. Later at some other point the two beams combine together. If the phases of the two beams are changed when they travel along the two paths, when they join together they will interfere with each other either constructively or destructively. Rigid scatterers such as fixed impurities don't contribute to phase-relaxation, while fluctuating scatterers such as phonons and other electrons do. Long wavelength phonons are less effective in destroying phase, since they

11

are more delocalized in space and tend to affect different paths in the same way. Thus the phase relaxation time of phonon is frequency dependent, i.e.,

$$\tau_\varphi \sim (\tau_c / \omega^2)^{1/3}, \tag{2.19}$$

where τ_c is the collision time, ω is the phonon frequency.

At low temperatures phonons are suppressed and electron-electron scattering dominates phase relaxation. An electron with a small excess energy Δ (=E-E$_f$) has very few states to scatter down into since most states below it are already full. For this reason, the scattering is strongly suppressed by the exclusion principle as Δ tends to zero. In a 2-DEG the relation takes the form as

$$\frac{\hbar}{\tau_\varphi} \sim \frac{\Delta^2}{E_f}[\ln(\frac{E_f}{\Delta}) + c], \tag{2.20}$$

where c is a constant. Note that when Δ increases τ_ϕ decreases, indicating an enhanced phase relaxation. However if the mobility of the 2D conductor is low ($\hbar/\tau_m > k_B T$), τ_ϕ has an additional component which depends linearly on temperature.

$$\text{If } \tau_\phi \leq \tau_m \text{ then } L_\varphi = v_f \tau_\varphi, \tag{2.21a}$$

$$\text{If } \tau_\phi > \tau_m \text{ then } L_\varphi^2 = v_f^2 \tau_m \tau_\varphi / 2. \tag{2.21b}$$

The diffusion coefficient is given by

$$D = v_f^2 \tau_m / 2. \tag{2.22}$$

Thus

$$L_\varphi^2 = D\tau_\varphi \, (\text{If } \tau_\phi > \tau_m). \tag{2.23}$$

If $n_s = 5 \times 10^{11}/cm^2$, $v_f = 3 \times 10^7 cm/s$.

2.2.2 Single molecular energy level model

Current is one kind of flux of matter, so normally it corresponds to ***non-equilibrium*** states. In this section the coherent transport is considered, i.e., with no energy transfer.

A typical model to describe electron transport through a molecule is a sandwiched structure, *i.e.* a molecule connected to left and right metal leads. There are several parameters to describe the whole system regarding electron transport: the energy levels of the isolated molecule, the chemical potential of the metal leads, and the coupling between molecule and leads.

For simplicity, we assume that the molecule has only a single energy level ε_0, and it's ***not change*** when connected to leads. The chemical potential of metal leads is defined as μ_0. In the Smeagol program package, μ_0 of the left and right lead are the same. When a bias V is applied, the potential of left lead becomes $\mu_L=\mu_0+V/2$ and that of the right lead is $\mu_R=\mu_0-V/2$, forming a bias window $[\mu_0-V/2, \mu_0+V/2]$. The coupling to the left and right lead is depicted by Γ_L and Γ_R respectively, *i.e.* the hopping probabilities are $\Gamma_L/\hbar$ and $\Gamma_R/\hbar$. The stronger the coupling the quicker the electron flows from (to) the electrode into (from) the molecule.
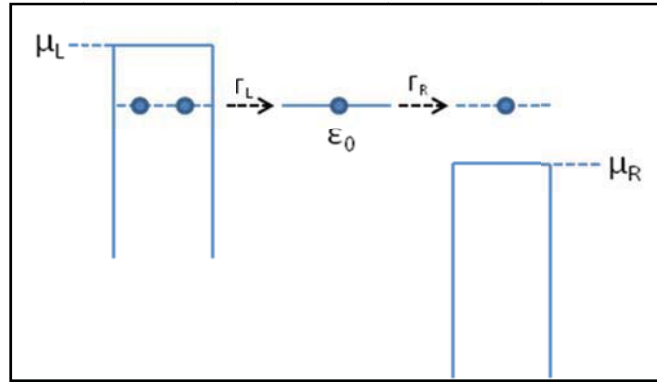
Figure 2.1 Diagram illustrating the molecular energy level ε_0 lying between μL and μR.

There are three kinds of energy alignment between molecule and leads, *i.e.* ①$\varepsilon_0 > \mu_L > \mu_R$, ②$\mu_L > \varepsilon_0 > \mu_R$, and ③$\mu_L > \mu_R > \varepsilon_0$. Only the second case allows electron transport

from left lead to molecule, and then from molecule to right lead (Figure 2.1). Current is suppressed in the other two cases, since either the molecular energy level is empty (①) or there are no empty states available in the right lead (③).

By this simple model, the time-averaged non-equilibrium charge on the molecule N (the population) can be calculated self-consistently. As a consequence, the calculated current is

$$I = \frac{2e}{h} \frac{\Gamma_L \Gamma_R}{\Gamma_L + \Gamma_R} (f(\varepsilon_0, \mu_L) - f(\varepsilon_0, \mu_R)) \tag{2.24}$$

where f is the Fermi distribution.

There are several features of the calculated current. 1. As long as the molecular state lies outside of the bias window, there is no current. The size of the gap (the bias range within which there is no current) is given by $4|\mu_0 - \varepsilon_0|$. This is to say, the current is suppressed with a small bias unless $\mu_0 = \varepsilon_0$ (rarely!). When chemical potential of leads (μ_0) is far from the molecular energy level (ε_0), the gap is large. 2. When the bias is equal to $2|\mu_0 - \varepsilon_0|$ (half the gap), current quickly jumps to the maximum value

$$I_{max} = \frac{2e}{h} \frac{\Gamma_L \Gamma_R}{\Gamma_L + \Gamma_R} \tag{2.25}$$

Note that I_{max} is independent of the energy levels of electrodes and molecule, and only relates to the coupling!

A more realistic model can be considered by including changes to the Hamiltonian arising from changes in the occupation of the molecular energy level, *i.e. the charging effect* in the framework of a single energy level model.

A simple approximation is to assume that the energy level has the following form

14

$$\varepsilon = \varepsilon_0 + U_{SCF}, \tag{2.26}$$

where the molecular energy level shift is given by

$$U_{SCF} = U \times (N - 2f(\varepsilon_0, \mu_0)) \tag{2.27}$$

U_{SCF} is the correction of the molecular energy level, due to the change of electron population on the molecule, including classical electrostatic potential and possibly quantum electron-electron interactions. N denotes the non-equilibrium electron population on molecule while $2f(\varepsilon_0, \mu_0)$ denotes the electron population when no bias is applied. This equation assumes a linear relationship between energy change and population change (charging effect) with U being the coefficient.

When charging effect is included, the change of *I-V* characteristics is: when the bias is increased to $2|\mu_0 - \varepsilon_0|$ current doesn't jump to I_{max} quickly, rather, it increases from zero linearly, until goes to I_{max} at $2|\mu_0 - \varepsilon_0| + 2U$. Note I_{max} is still given by equation (2), i.e. it's still solely dependent on the coupling!

Another interesting consequence of charging effect is, if $\Gamma_L \neq \Gamma_R$, I-V curve is asymmetric, *i.e.* the response of current under positive bias is different from that under negative bias. A more realistic description of this model might eventually lead to *rectification*!

2.2.3 The conductance

2.2.3.1 Resistance of a ballistic conductor

The conductance of a macroscopic conductor is inversely proportional to the length of the conductor. However, experiments indicate the measured conductance approaches a value of G_c (contact conductance) when the length of the conductor is much smaller than the mean free path L_m. We always assume that the contacts are much more conducting than the conductor to be measured so that the applied voltage drops entirely across the

conductor. G_c is referred to as the contact conductance, and corresponds to only the resistance for a ballistic conductor (no intrinsic scatterer).

An electron can usually exit from a narrow conductor into a wide contact with negligible probability of reflection, and we refer to the wide contact as a 'reflectionless' contact.

The conductance quantum G_0 is

$$G_0 = \frac{2e^2}{h} = (12.9k\Omega)^{-1}$$

(2.28)

12.9 kΩ (or equivalently 7.748×10^{-5} siemens) is the contact resistance of a single-moded conductor.

For a ballistic conductor the applied bias entirely drops at the two interfaces but none inside the conductor. If the conductor has M (transverse) *modes* (i.e., subbands) available, then the contact resistance is $\frac{12.9k\Omega}{M}$. Obviously, the contact resistance is inversely proportional to the number of modes. For a thin rectangular conductor, assuming electron transport is along the length direction, the number of modes M is proportional to the conductor width, $M = Int[\frac{W}{\lambda_f/2}]$. Assuming a Fermi wavelength of 30 nm, the number of modes in a 15 μm wide field-effect transistor is approximately 1000, so the contact resistance is about 12.9 Ω.

2.2.3.2 Landauer formula

A macroscopic conductor usually follows the ohmic scaling law: G=σW/L. For smaller conductors there are two corrections. Firstly, there is an interface resistance (contact resistance) independent of the length L of the sample. Secondly, the conductance doesn't decrease linearly with the width W. Rather, it depends on the number of transverse modes in the conductor and decreases in discrete steps.

The Landauer formula is

16

$$G = \frac{2e^2}{h} MT,$$

(2.29)

where M is number of modes, T is the average probability that an electron injected at one end of the conductor will transmit to the other end. For a ballistic conductor $T = 1$.

The Landauer formula can be rewritten as

$$R = G^{-1} = \frac{h}{2e^2 M} + \frac{h}{2e^2 M} \frac{1-T}{T}.$$

(2.30)

The resistance R is given by the contact resistance, which is independent of T, and the 'actual' resistance of the conductor, respectively. If $T = 1$ the second term vanishes (ballistic).

For a wide conductor with many modes the conductance is

$$G = e^2 W N_s (\upsilon_f T / \pi),$$

(2.31)

where W is the width, N_s is a constant $(m/\pi\hbar^2)$, v_f is Fermi velocity and T is transmission.

The Einstein relation describing the relationship between conductivity and diffusion coefficient is

$$\sigma = e^2 N_s D.$$

(2.32)

The transmission probability through a conductor of length L is

$$T = \frac{L_0}{L + L_0},$$

(2.33)

where L_0 is a characteristic length of the order of a mean free path.

Thus the conductance can be written as

$$G = \frac{\sigma W}{L + L_0} .$$

(2.34)

Note if $L \ll L_0$ then G approaches a constant of $\frac{\sigma W}{L_0}$. If $L \gg L_0$ then the resistance is

proportional to L (Ohm's law resumes).

2.2.3.3 The location of resistance

Consider a conductor with M modes sandwiched between two contacts. This conductor is also called a 'waveguide'. For simplicity, we assume that there is only one scatterer (**X** in the Figure 2.2) with transmission probability T. The positive direction is defined as from left to right.

On the left of **X**, the $+k$ state can enter the conductor from left electrode without reflection, so the Fermi energy for $+k$ state is the same as left electrode, i.e., μ_1. Similarly, the Fermi energy of $-k$ state on the right of **X** is μ_2.

The distributions of electrons of $+k$ states on the right and electrons of $-k$ states on the left are not as simple. Assuming zero temperature, the states of both $+k$ and $-k$ directions below μ_2 are fully occupied. Between μ_1 and μ_2 the situation is more complex since electrons get scattered at **X**. In the near left and near right regions (within a few energy relaxation lengths to **X**) the electron distributions are highly non-equilibrium distributions, so no Fermi distributions can be achieved.

However, farther from the scatterer, Fermi distributions are reestablished (Far left and Far right as shown in Figure 2.2).

The corresponding quasi-Fermi levels F′ for $-k$ states in the far left region and F″ for $+k$ states in the far right region can be estimated by noting that the total number of electrons should be conserved,

$$F' = \mu_2 + (1-T)[\mu_1 - \mu_2],$$

(2.35a)

18

$$F'' = \mu_2 + T[\mu_1 - \mu_2].$$
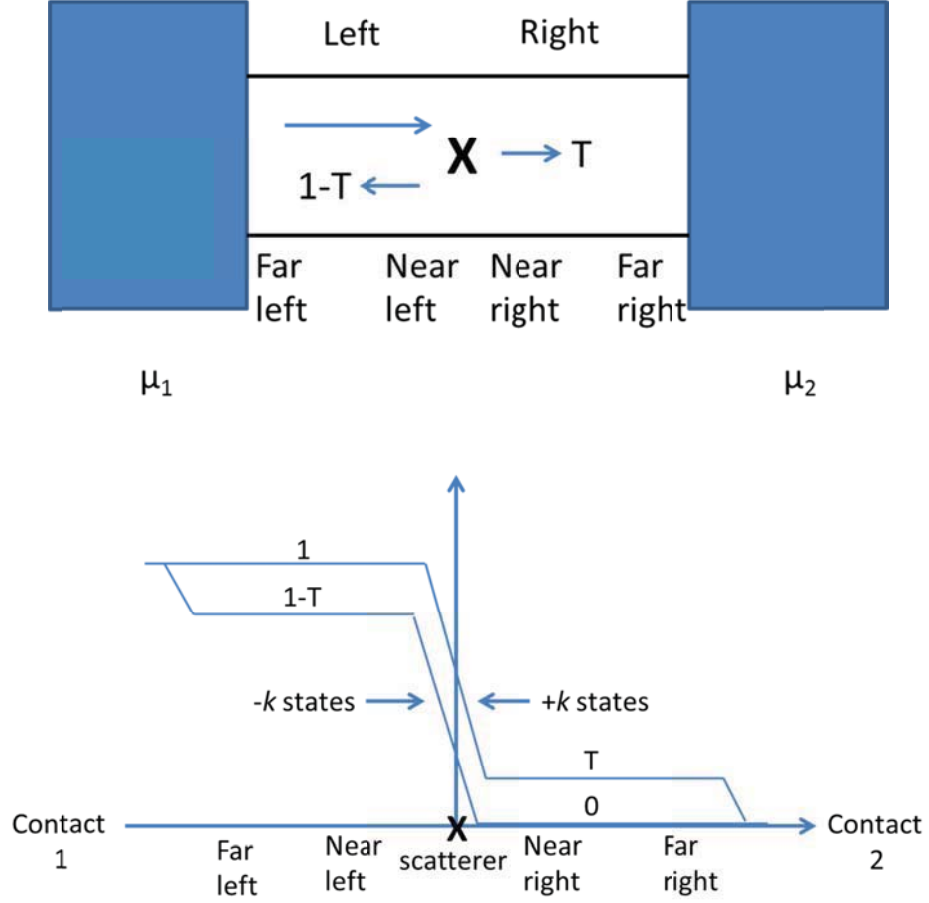
Figure 2.2 Upper: a schematic view of one waveguide (conductor) sandwiched between two electrodes. The left electrode has a higher electrochemical potential (μ_1) than the right electrode (μ_2). Lower: The normalized electrochemical potential for both $-k$ and $+k$ states.

These are the inelastic processes that are responsible for the energy relaxations in the near left and near right regions.

If we assume $\mu_1 = 1$ and $\mu_2 = 0$ we can plot the normalized potential of electrons at different positions (Figure 2.2 lower panel). The contact resistance of $-k$ states locates at the left interface while that contact resistance of $+k$ states locates at the right interface. There is a sharp drop of potential across the scatterer for both $-k$ and $+k$ states.

The scatterer resistance and the contact resistance are:

$$G_S^{-1} = \frac{h}{2e^2 M} \frac{1-T}{T},$$ (2.36a)

$$G_C^{-1} = \frac{h}{2e^2 M}.$$ (2.36b)

The potential drop I/G_S indeed occurs right across the scatterer. On the other hand, the corresponding energy dissipation occurs over an energy relaxation length which is the distance required to dissipate the Joule heat associated with G_S^{-1}, i.e. it is not localized at the scatterer.

There is a charge imbalance around the scatterer: electrons pile up to the left of the scatterer while there is a deficit to the right, forming a mesoscopic dipole around each obstacle known as a 'resistivity dipole'. This build-up of charge takes place over a screening length which is a few angstroms in metals but can be hundreds of angstroms in typical semiconductors.

The screening length can be expressed by a distance of β^{-1} as

$$\beta^{-1} = \sqrt{a_B d/2},$$ (2.37)

where a_B is the Bohr radius,

$$a_B = 4\pi\varepsilon\hbar^2 / me^2,$$ (2.38)

d is the thickness of the 2-D electron system, ε is the dielectric constant of the material, m is the effective electron mass. For example, for a 10 nm thick GaAs 2-D semiconductor, $m \sim 0.07 m_0$, $\varepsilon = 12.6\varepsilon_0$, then the Bohr radius is about 10 nm, and the screening length is about 5 nm. In metals the density of states is much higher so the screening length is much shorter.

2.2.4 Non-equilibrium Green's Function (NEGF)

2.2.4.1 Correlation and scattering functions

In a semiclassical picture, it is enough to describe a multiple-electron system by distribution function $f(k)$, which specifies the number of electrons occupying a particular state k. However, in ***phase-coherent*** conductors electron correlation has to be considered, since the phase-relaxation length is not very short. Phase correlation is nothing but the correlation between electrons with different states. In this case, density matrix $\rho(k, k') = \Psi_k \Psi_{k'}^*$, (rather than $f(k)$!) is appropriate to describe the system, which includes additional information regarding phase-corrections.

In general, a two-time-dependent correlation function of the form $G^n(k, k'; t, t')$ (***correlation function*** G^n or $-iG^<$) is needed to describe the correlation between the amplitude in state k at time t and that in state k' at time t'. Density matrix $\rho(k, k'; t)$ is a 'subset' of the correlation function obtained by setting $t' = t$.

$$\rho(k, k'; t) = [G^n(k, k'; t, t')]_{t'=t}, \tag{2.39}$$

In a steady-state $\Psi(t) = \Psi_0 e^{-i\omega t}$ and by using Fourier transformation we can get the energy-resolved information $G^n(k, k'; E)$. This is convenient to describe scattering processes which transfer electrons from one energy to another. If we are only interested in steady-state transport, $G^n(k, k'; E)$ is enough to describe correlation and we don't need $G^n(k, k'; t, t')$.

The occupation $f(k)$ function can be written in terms of the correlation function

$$f(k) = \int \frac{1}{2\pi} G^n(k, k; E) dE \tag{2.40}$$

This is true in any representation. For example in real space the electron density is

$$\underline{n}(r) = 2 \times \int \frac{1}{2\pi} G^n(r, r; E) dE \tag{2.41}$$

where a factor of 2 assumes degeneracy of the two spin components.

G^n refers to the correlation of electrons, while G^p (or $+iG^>$) refers that of **holes**. The inflow of electrons can alternatively be viewed as outflow of holes, whose number is given by $(1-f)$.

In the semi-classical picture the scattering function $S^{out}(\mathbf{k},t)$ tells us the rate at which electrons are scattered out of a state $\mathbf{k}$ assuming it is initially full. Like correlation function, in the quantum mechanical picture we need to generalize this concept to include phase-correlation

$$S^{out}(\mathbf{k},t) \rightarrow \Sigma^{out}(\mathbf{k},\mathbf{k}';t,t')$$

Again, in steady-state $\Sigma^{out}(\mathbf{k},\mathbf{k}';E)$ is enough to describe the **outscattering**.

Similarly, Σ^{in} describes the **inscattering**.

The set of four functions G^n, G^p, Σ^{in} and Σ^{out} provides us with the language needed to include phase-correlations into a transport problem. In standard literature the counterpart is $-iG^<$, $+iG^>$, $-i\Sigma^<$ and $+i\Sigma^>$, respectively. The classical analog is f, $(1-f)$, S^{in} and S^{out}, respectively.

2.2.4.2 Self-energy and the Green's function

Consider a model of a conductor coupled with several leads. The **Green's function** gives us the response at any point (inside or outside the conductor) due to an excitation at any other. For non-interacting transport the only excitations we need to consider are those due to waves incident from the leads. The real power of Green's function is evident when we include the interaction effect (electron-electron or electron-phonon). Such interactions give rise to excitations within the conductor, and can not be described by simple S-matrix.

In Green's function concept, the response R is related to the excitation S

$$R=GS, \tag{2.42}$$

22

where G is Green's function.

Or, we can express the problem as

$$\Psi = GS = [E-H]^{-1}S,$$
(2.43)

where Ψ is the wavefunction, H is the Hamiltonian operator and S an equivalent excitation term due to a wave incident from one of the leads in the multiple-terminal problem.

$$H \equiv \frac{(i\hbar\nabla + eA)^2}{2m} + U(r)$$
(2.44)

The inverse of a differential operator is **not** uniquely specified unless the boundary conditions are given. Commonly, two different Green's functions (retarded and advanced) are defined corresponding to two different boundary conditions.

The Green's function G(x, x′) can be viewed as the wavefunction at x resulting from a unit excitation applied at x′. Retarded Green's function (G^R) represents the outgoing waves that originate at the point of excitation while advanced Green's function (G^A) represents the incoming waves that disappear at the point of excitation (Figure 2.3).

One way to incorporate the boundary conditions (far from excitation, e.g. is it an outgoing wave (retarded) or an incoming wave (advanced)?) is to add an infinitesimal imaginary part to the energy. In general the retarded Green's function is defined as

$$G^R = [E - H + i\eta]^{-1} \quad (\eta \to 0^+),$$
(2.45)

while the advanced Green's function is defined as

$$G^A = [E - H - i\eta]^{-1} \quad (\eta \to 0^+),$$
(2.46)
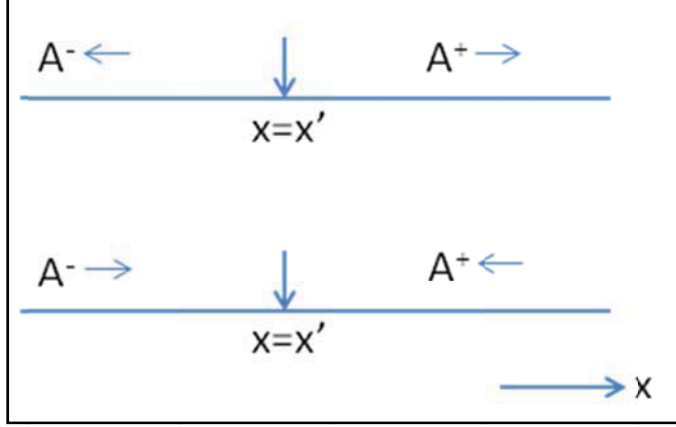
Figure 2.3 Retarded (upper) and advanced (lower) Green's function for a 1D system. A denotes the amplitude of wavefunctions.

The small imaginary part of the energy introduces an imaginary component to the wavenumber.

$$k \rightarrow k(1 + i\delta), \tag{2.47}$$

From hereon we will generally refer to the *retarded* Green's function as just the 'Green's function'.

To study the response to excitation, we need to solve the differential equation for the Green's function

$$[G^R]^{-1}G^R(r;r') = [E - H + i\eta]G^R(r;r') = \delta(r - r') \quad (\eta \rightarrow 0^+), \tag{2.48}$$

where delta function is a unit excitation, G^R is a differential operator, G^R(r; r′) is the response function we need to find.

A common approach to solve such a differential equation like the above equation is to *discretize* the spatial coordinate so that the Green's function becomes a matrix.

$$G^R(r;r') \rightarrow G^R(i;j), \tag{2.49}$$

where the indices i and j denote points on a discrete lattice.

The above equation becomes a matrix equation (the method of *finite differences!*)

$$[(E+i\eta)I - H]G^R(i;j) = I.$$

(2.50)

Note H in (2.50) is the matrix representation of the Hamiltonian operator. Now we can calculate G^R by inverting the matrix $[(E+i\eta)I - H]$ numerically.

Keep in mind that we are dealing with a model of one conductor coupled with several semi-infinite leads. To describe this system, the **overall** Green's function can be written as

$$G^R = [EI - H_c + \Sigma^R]^{-1},$$

(2.51)

where

$$\Sigma^R = \sum_p \Sigma_p^R \text{ and } \Sigma_p^R(i,j) = t^2 g_p^R(p_i, p_j).$$

(2.52)

H_c is the Hamiltonian of isolated conductor, Σ_p^R is an effective Hamiltonian arising from the interaction of the conductor with lead p, t is the coupling between conductor and lead and $g_p^R = [(E+i\eta)I - H_p]^{-1}$ the Green's function for the isolated semi-infinite lead p. The overall Green's function G^R represents the propagation of electrons between two points inside the conductor, taking the effect of leads into account through the term Σ^R. Σ^R is often referred as '**self-energy**' due to the leads. The interaction of the electrons with phonons and other electrons is also called self-energy. The advanced Green's function G^A and the advanced self-energy Σ^A are the Hermitian adjoints of the corresponding counterparts

$$G^A = [G^R]^+ \text{ and } \Sigma^A = [\Sigma^R]^+,$$

(2.53)

G^R describes the coherent evolution of an electron from the moment it is injected until it loses coherence either by disappearing into a lead or by scattering into a different state

(due to electron-phonon or electron-electron interactions) where a new coherent trajectory is initiated. The self-energy Σ^R describes the effect of the leads and the interactions on the electron dynamics.

The correlation function and the Green's function has the following relation

$$G^n + G^p = i[G^R - G^A] \equiv A .$$
(2.54)

The spectral function A represents a generalized density of states, showing the nature of the allowed electronic states, regardless of whether they are occupied (G^n) or not (G^p). Another relation is

$$\Sigma^{in} + \Sigma^{out} = i[\Sigma^R - \Sigma^A] \equiv \Gamma ,$$
(2.55)

The function Γ determines the rate of loss of electrons by scattering. A and Γ are related by

$$A = G^R \Gamma G^A = G^A \Gamma G^R ,$$
(2.56)

At equilibrium, all states are occupied according to a single Fermi function $f_0(E)$ determined by the electrochemical potential. If we are interested in the equilibrium quantities only, the retarded Green's function contains all the information we need. We can calculate the spectral function A using $G^n + G^p = i[G^R - G^A] \equiv A$. Then the correlation functions can be calculated by

$$G^n(E) = f_0(E)A(E), \ G^p(E) = (1 - f_0(E))A(E) .$$
(2.57)

On the other hand, the *central result of the NEGF* is a *kinetic equation* relating the correlation functions to the scattering functions:

$$G^n = G^R \Sigma^{in} G^A, \ G^p = G^R \Sigma^{out} G^A .$$
(2.58)

The inscattering function Σ^{in} tells us the rate at which electrons come in, so that it seems reasonable in the above equation that the electron correlation function G^n should be proportional to it. Similarly it is reasonable that the hole correlation function G^p be proportional to the outscattering function Σ^{out}.

In the following I will describe the self-energy and correlation function in an analogy way.

The correlation function $G^n(\mathbf{r}, \mathbf{r}')$ is a quantum generalization of the electron occupation (or electron density in real space representation). Let's think about the human population in Houghton and Chicago. The on-site correlation function ($G^n(\mathbf{r}, \mathbf{r}')$, or $\rho(\mathbf{r})$), shows how happy people feel with each other in Houghton. The happier, the lower the 'energy' is. The off-site correlation function shows how happy people in Houghton are with people in Chicago. Again, the happier, the lower the energy is.

The self-energy represents the dynamic change of electrons: scattering (from one place to another place, or from one state to another state). Specifically, self-energy is related to the interaction between conductor and leads, or the phase-breaking interactions (electron-electron, or electron-phonon) inside the conductor. In analogy, the self-energy can be thought as the population transfer between Houghton and Chicago. In general, the higher the population, the higher the transfer rate is. This relation can be reflected by equation $G^n = G^R \Sigma^{in} G^A$, $G^p = G^R \Sigma^{out} G^A$.

Furthermore, the SCF iteration method can be useful in the field of sociology. One can estimate the population distribution across the US, or even across the whole world. The central idea is, the realistic population distribution corresponds to the ground state, which has the lowest energy. Thus, it is essential to parameterize the 'self-energy' and 'correlation function' in the SCF iteration method.

2.3 The SIESTA code

2.3.1 Introduction

The full name of SIESTA is 'Spanish Initiative for Electronic Simulations with Thousands of Atoms' which is developed in Europe[56]. SIESTA can do standard DFT electronic structure calculations and *ab-initio* molecular dynamics simulations. The TranSIESTA module[57] by which electronic transport calculations can be performed has also been incorporated into SIESTA starting from version 3.0.

The main features of the program:

- Standard LDA or GGA approximations.
- Norm-conserving pseudopotentials in the fully non-local form.
- Flexible linear combination of atomic orbitals (LCAO) as basis set. Off-site orbitals (ghost atoms) are applicable.
- Electron density is projected onto a real-space grid.
- Written in Fortran 90. Parallel calculations can be performed under MPI.

The main properties that can be determined are the following:

- Total and partial energies.
- Atomic forces and stress tensor.
- Electron density and electronic structure.
- Geometry relaxation.
- Constant-temperature molecular dynamics.
- Non-equilibrium electron transport transmission functions and I-V characteristics.

2.3.2 Application of pseudopotential

First-principles ionic pseudopotentials are extracted from atomic calculations by some scheme. In the first step, a neutral (screened) atomic pseudopotential V^l (l being the angular momentum quantum number) is obtained[58]. To apply PP to crystals or molecules,

an ionic (unscreened) PP V_{ion}^1 is obtained in the second step by subtracting from V^1 the Coulomb and exchange-correlation potentials.

Louie *et al*. proposed the following formulism[58],

$$V_{ion}^{l\sigma}(\vec{r}) = V^{l\sigma}(\vec{r}) - V_{ee}(\rho^v(\vec{r})) - V_{xc}^{\sigma}(\rho^v(\vec{r}) + \rho^c(\vec{r}), \xi(\vec{r})), \qquad (2.59)$$

where $\xi(\vec{r}) = \dfrac{\rho_+^v(\vec{r}) - \rho_-^v(\vec{r})}{\rho^v(\vec{r}) + \rho^c(\vec{r})}$, σ is the spin component.

In this formalism, the total exchange and correlation potential, including the nonlinear core-valence term, is subtracted from the screened potential. To avoid the complexity of taking into account the full core charge with its very high Fourier components, Louie replaced the full core electron density by a partial core electron density. This partial core electron density is equal to the true core electron density outside some radius r_0 and arbitrary inside. Louie found r_0 may be chosen as the radius where the core charge density is from 1 to 2 times larger than the valence charge density, so that most of the overlap between core and valence electron density is found for $r > r_0$. The partial core electron was chosen to be

$$\rho_{partial}^c(r) = \begin{cases} A \sin(Br)/r & \text{if } r < r_0 \\ \rho^c(r) & \text{if } r > r_0, \end{cases} \qquad (2.60)$$

where A and B are determined by the value and the gradient of the core electron density at r_0.
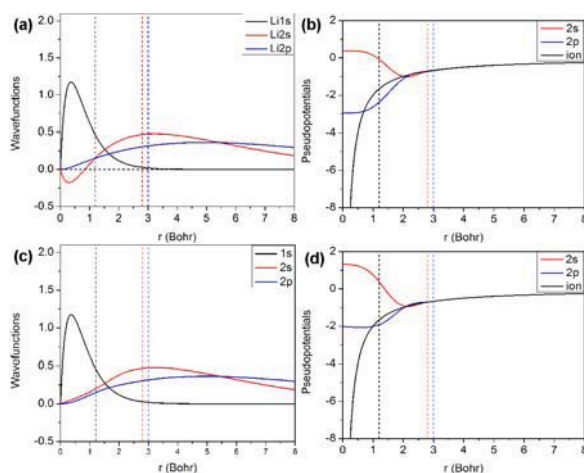
Figure 2.4 (a) Electron wave functions of all-electron (AE) calculation, (b) pseudopotentials without partial core correction, (c) AE 1s wave function and pseudo 2s and 2p wave functions, and (d) pseudopotentials with partial core correction.

Table 2.1 The valence orbitals eigenvalues: AE (all electron) calculation vs. PP (pseudopotential) calculations. LDA functional is used.

AE

nl	Spin	Occupation	Energy level (eV)
2s	-0.5	1.0000	-0.23265113
2s	0.5	0.0000	-0.13826778
2p	-0.5	0.0000	-0.09844391
2p	0.5	0.0000	-0.02981598

PP, no core correction

nl	Spin	Occupation	Energy level (eV)
2s	0.5	1.0000	-0.23263631
2s	0.5	0.0000	-0.12074134
2p	0.5	0.0000	-0.10765243
2p	0.5	0.0000	-0.02565891

PP, core correction

nl	Spin	Occupation	Energy level (eV)
2s	0.5	1.0000	-0.23264902
2s	0.5	0.0000	-0.13847716
2p	0.5	0.0000	-0.09862258
2p	0.5	0.0000	-0.02974995

2.3.3 Calculate work function by SIESTA

The work function W of a metal is closely related to its Fermi energy yet the two quantities are not exactly the same. This is due to the surface effect of a real-world solid: a real-world solid is not infinitely extended. Indeed, the charge distribution in those cells near the surface will be distorted significantly from that in a cell of an ideal infinite solid, resulting in an effective surface dipole distribution.

The work function of the metal with surface is defined as $W = -E_f + W_S$ where E_f is Fermi level of metal, and W_S accounts for the potential difference due to effective surface dipole.

In the Siesta program, the Fermi level given in the output files is ill-defined[59]. For example, in a gold bulk calculation including only 1 atom in the primitive cell using Transiesta's PP with a moderate accuracy (16x16x16 k sampling, 200 Ry), the Fermi level calculated by Siesta is -3.32 eV, without defining zero of the energy level for gold.

However, SIESTA calculates the deformation energy δV, which is defined as the difference of crystal potential and the superposition of neutral-atom potentials. δV is integrated to zero in one unit cell. In other words, the average value of δV within one unit cell is zero. Thus, with a model of gold surface including vacuum we can determine the work function of gold bulk, as described.

First, we need the information of δV. Siesta (version 3.0-rc2) output provides the VH and VNA files, representing the total electrostatic potential and neutral-atom potential, respectively. Taking use of the 'pot.exe' tool included in Smeagol[60], we can get the plane-average potentials along z direction (the gold surface of interest is perpendicular to z), see Figure 2.5.
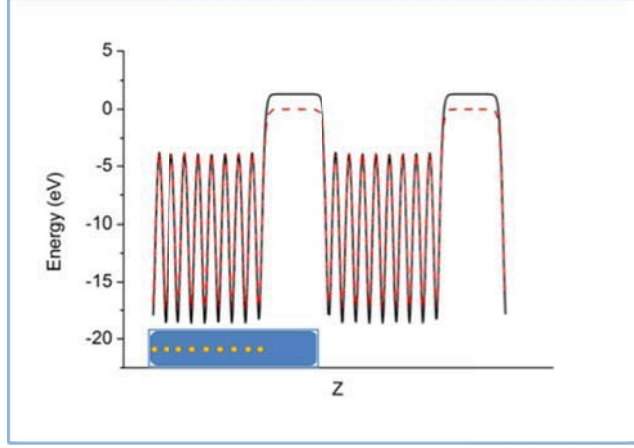
Figure 2.5 Nine layers of gold and vacuum fill in the unit cell, as shown in the insert. The z direction is along gold 111. The planer averaged VH (solid) and VNA (dashed) is plotted along z direction. Two unit cells are included in the plotting. The blue insert represents one repeating cell of the calculated model.

Then, by calculating the difference of (averaged) potentials VH and VNA, we get the (averaged) δV, as plotted in Figure 2.6.

We found that the averaged δV throughout one unit cell (area bounded by solid red lines) is indeed zero. According to the common convention, the potentials of VH, VNA and δV should all converge to zero deep in vacuum. However, only VNA goes to zero in vacuum, as shown in Figure 2.5 and Figure 2.6. This just reflects the fact that the criterion that Siesta uses is, again, to average δV in one unit cell to zero. What potential, i.e., VH, VNA or δV should be considered? It is the δV, since all energy eigenvalues in Siesta take it to be the reference point. In the common convention (we call this convention the reality representation hereafter for simplicity), δV is set to zero in vacuum. As shown in Figure 2.6, the difference of δV between the central gold layer and vacuum is 1.98 eV. This means, the value of δV within the central gold layer in the reality representation is -1.98 eV. Note although that the absolute values of energies are not the same in the reality representation and in the 9-layer-model representation (the calculation model shown in Figure 2.5), the energy difference in any representation is definite.

If we assume δV in the reality representation, as a property of gold crystal, has the same value within the central layer in our nine-layer model (area bounded by dashed lines in

32

Figure 2.6) and within one (111) layer in an infinite gold bulk, we can then calculate the value of E_f of bulk gold in the reality representation. As stated above, the Fermi level of gold infinite bulk is -3.32 eV, and we know that the zero energy level in the reality representation is -1.98 eV, then the 'real' gold Fermi level is -3.32+(-1.98)= -5.30 eV. How should we interpret this 'real' Fermi level?
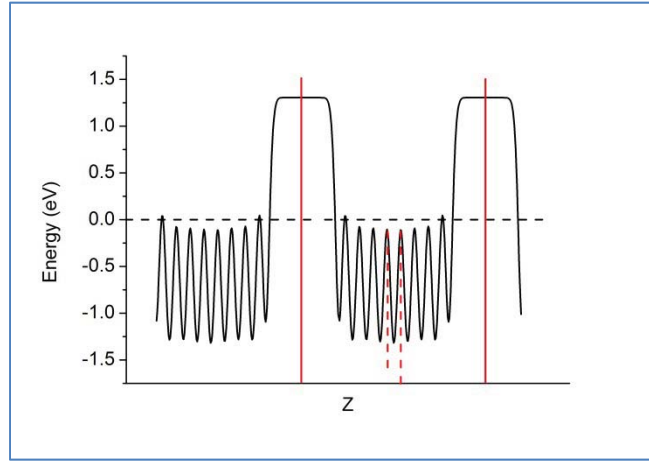
Figure 2.6 The planar averaged δV of nine layers of gold and vacuum. δV=VH-VNA

On one hand, this value (-5.30 eV) reflects the property of infinite gold bulk, since -3.32 eV is the result in an independent infinite bulk calculation. On the other hand, this value reflects the effects of gold (111) surface, since the variation of δV along z direction in Figure 2.6 describes the property of gold (111) surface. Thus, we can argue that, the value of 5.30 eV is the work function of gold bulk along (111) surface, in good agreement with the value of 5.31 eV in experiment[61].

One may wonder how many gold layers are necessary to calculate the work function. For this purpose, we also did similar calculations for models including 3 and 6 gold atomic layers in presence of vacuum. We found that the difference among these models is very small, i.e., the zero energy level in the reality representation calculated within 3-layer model and 6-layer model differs from 9-layer model as zero and 0.03 eV, respectively. Therefore it can be concluded that even 3 gold layers can yield a reasonably good zero energy point in gold bulk in our computational model.

Now let's consider the work function of graphene which is deposited on gold (111) surface. The lattice constants of graphene and gold bulk are 2.46 Å and 4.08 Å, respectively. When graphene is deposited on gold (111) surface, good lattice matching can be formed (Figure 2.7). Although the primitive cell of graphene and gold surface is different due to different crystal symmetry, one common unit call can be 'made' which contains 8 carbon atoms in graphene layer and 3 gold atoms in gold (111) surface, respectively. The lattice mismatch between graphene and gold is about 1.5%. In our calculation, we make the lattice parameters of graphene fixed and make the wettice parameters of gold match that of graphene, since the band structure around Fermi level is more sensitive in the case of graphene than gold. We take the geometry as shown in Figure 2.7, *i.e.*, within each unit cell, one gold atom of the (111) surface is on top of one carbon atom of one sublattice of graphene, one gold atom is on top of one carbon atom of the other sublattice of graphene, while the last gold atom is on top of the center of one graphene hexagonal ring.
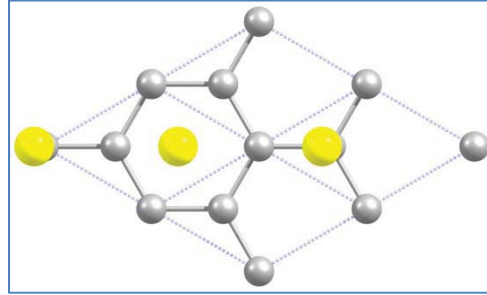
Figure 2.7 The lattice matching between graphene and gold (111) surface

We note that the procedure needed to calculate the work function of graphene deposited on gold surface is essentially the same as the one we used to calculate the work function of gold surface without graphene. On one hand, the gold Fermi level as a bulk property, should not be changed by the deposited graphene, since in reality the number of atoms in gold bulk should be much higher than that in one graphene monolayer. On the other hand, the variation of deformation energy δV along z direction should reflect the properties of both gold-graphene interface and graphene-vacuum interface. In Figure 2.8 we plotted the planar average δV as a function of z coordinate, with one graphene layer deposited on the right surface (left panel) and two graphene deposited on both surfaces.

34
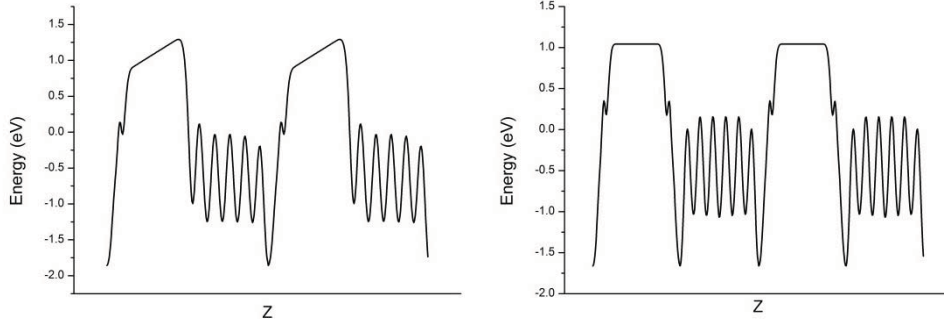
Figure 2.8 The planer averaged δV of gold layers with one (left) and two (right) layers of graphene deposited as a function of z. As Figure 2.5 and Figure 2.6, two unit cells in calculation are shown.

As shown above, if only one graphene sheet is deposited on one side of gold layers, the left and right surfaces of gold become asymmetric. This asymmetry induces a numerical error, i.e., the value of δV is not constant in the vacuum region. In contrast, if both gold surfaces are deposited by graphene, δV is constant in vacuum and a good evaluation of δV difference between the region deep inside gold and vacuum can be pursued. Adopting the calculation model of the right panel of Figure 2.8 we obtain δV to be 1.65 eV, indicating that the value of δV in gold bulk is -1.65 eV in the model containing two graphene sheets. With the same method we used to calculate the work function of gold (111) surface without graphene, we get the work function of gold with graphene deposited on (111) surface as 4.97 eV, i.e., 0.33 eV smaller than gold without graphene deposition.

Chapter 3   The Effect of Single-Atom Doping on the Electronic Transport Properties of C_{60} Fullerene[1]

3.1 Introduction

C_{60} is a true nanoscale single molecule. Its electronic structure and energy levels can be considerably affected by modifying a single atom in its structure. Thus, doping of fullerenes can be generally expected to change their electronic conductivity due to modification in the density of states near the Fermi surface. Indeed, a recent experimental study[62] has shown that the NC_{59} molecule acts as a molecular rectifier in a double barrier tunnel junction via the single electron tunneling effect.

Following the semiconductor analogy, one may find that B and N atoms substituting C atoms in the fullerene cage can act as "acceptors" and "donors", respectively, thus modifying its electron transport properties similar to what happens to Si. In order to realize such *p*- and *n*-type doped fullerenes, there have been several attempt in the recent years to synthesize BC_{59}[63] and NC_{59}[64]. These experimental efforts have been complimented by several theoretical studies focused mainly on the calculations of the stability and electronic properties of BC_{59}[65] and NC_{59}[66,67].

While BC_{59} and NC_{59} offer a substitutional approach to modify the electronic structure of fullerene for electronic device applications, endohedral fullerenes encapsulating atoms or molecules inside the fullerene cage provide an alternative and additional approach to altering the electronic properties of fullerenes, not available in bulk semiconductors or any other materials. Generally, noble gases-[68] or metal-[69] endofullerenes have been characterized. A few studies have also focused on N-encapsulated endofullerene. These studies suggest that molecular nitrogen can be considered as a van der Waals molecule trapped inside the fullerene cage[70]. Surprisingly, B-encapsulated endofullerenes have not

---

yet been investigated, although encapsulation of a smaller boron atom inside the cage can be expected to form a stable B@C_{60} endofullerene.

In this chapter, we consider B and N doped fullerenes, namely the B@C_{60} and N@C_{60} endofullerenes and the substitutional derivatives, BC_{59}, and NC_{59}, where the dopant atom has replaced one carbon atom on the cage. The aim of the present study is two-fold: (i) To understand the effect of a single-atom change in nanoscale structure on the electronic structure and electron transport and (ii) to determine the effect of the chemical nature (B vs N) as well as the geometrical position (i.e. substitutional vs. interstitial) of the dopant on current-voltage (i.e., *I-V*) characteristics of fullerenes.

3.2 Computational Method

The electron transport calculations were performed with the use of density functional theory (LDA-DFT) together with the non-equilibrium Green's Function (NEGF) method. A schematic illustration of the central scattering region of the model architecture is shown in Figure 3.1, where semi-infinite gold contacts are represented by four 6×6 **R** gold bilayers along the (001) direction on either side of the contacts.

For the electron transport, the current via a molecule can be obtained as

$$I = \frac{e}{h} \int_{-\infty}^{\infty} dE \ T(E,V) \big[f(E - \mu_1) - f(E - \mu_2) \big], \qquad (3.1)$$

where μ_1 and μ_2 are the electrochemical potentials in the two contacts under an external bias V, $f(E)$ is the Fermi-Dirac distribution function. The transmission function, $T(E,V)$ is an important intrinsic factor describing the quantum mechanical transmission probabilities for electrons. The semi-infinite effect of the left (right) electrode is taken into account by introducing the self-energy Σ_L (Σ_R) in the effective Hamiltonian[55]. It is worth noting that the transmission depends on both the electron energy E and the applied external bias V.
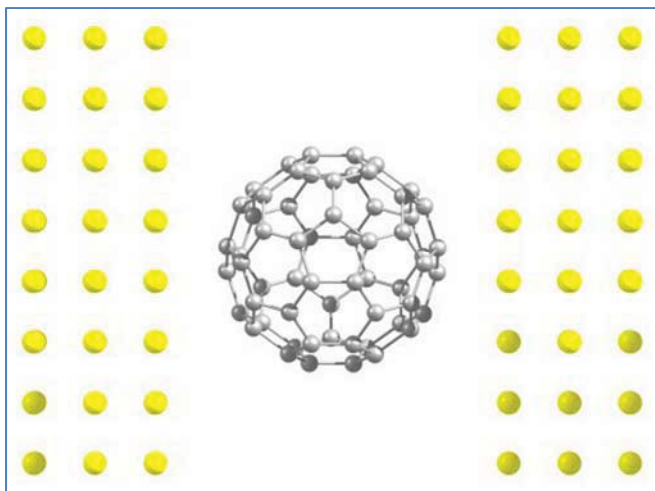
Figure 3.1 A schematic illustration of Au-C_{60}-Au system.

3.3 Results and Discussion

3.3.1 Ground State

There are two C-C bond lengths (R_{C-C}) in the optimized fullerene configuration; 1.45 Å for pentagons (type I) and 1.40 Å for hexagons (type II), which compare well with the previously calculated values of 1.45 and 1.37 Å, respectively[71]. Similarly, the calculated gap of about 1.3 eV between the highest occupied molecular orbital (HOMO) and the lowest occupied molecular orbital (LUMO) is in agreement with the previous studies[72].

In the endofullerenes (B@C_{60} and N@C_{60}), both B and N atoms occupy the center of the fullerene cage, with bond length, R_{B-C} or $R_{N-C,}$ of 3.58 Å. There appears to be no distortion in the surrounding cage due to the atomic dopants. For the substitutional fullerenes, BC_{59} and NC_{59}, the overall distortion in the cage induced by the substituted dopants is found to be small in agreement with previous studies[67]. The structural distortion in the substitutional derivatives is also reflected in the electronic polarization; the calculated value of the dipole moment is 0.71 and 1.62 debye for BC_{59} and $NC_{59,}$ respectively.

3.3.2 Transport Properties:
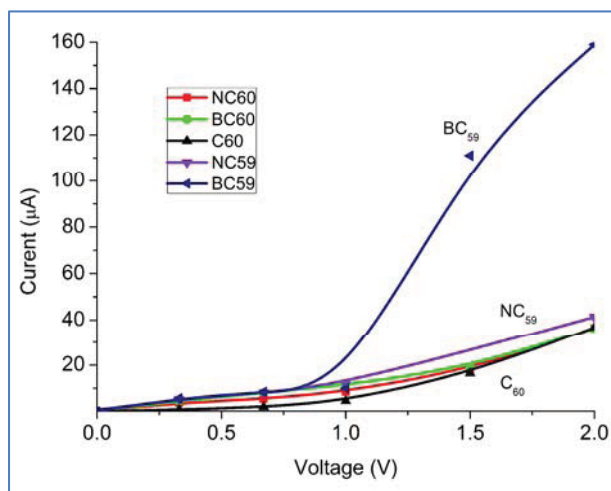
Figure 3.2 The current-voltage characteristic of C_{60}, BC_{59}, NC_{59}, BC_{60} and NC_{60}.

We begin with a pristine C_{60} molecule to benchmark our results, since its electronic transport properties have been studied extensively[73-75]. An inspection of the calculated current (I)-voltage (V) characteristics of C_{60}, shown in Figure 3.2 suggests a metal-like conduction in the low bias range of -1 to +1 V. With the increase in the external bias to 2V, a significant increase in current occurs. This can be interpreted in terms of the transmission function, which characterizes the intrinsic transport characteristics of the system. The transmission function as a function of the applied bias and the density of states for the C_{60} molecule is shown in

Figure 3.3. In general, every transmission peak in the bias window corresponds to a certain molecular orbital (MO), including the intrinsic orbitals of the molecule and the hybridized orbitals of the molecule with the gold leads. For Au-C_{60}-Au, a large HOMO-LUMO gap reflects itself in a vanishing transmission near the Fermi region. The closest transmission peak at ~ -0.8 eV is due to the HOMO-derived states whereas the peak ~ 0.8 eV is due to the LUMO-derived states (

Figure 3.3) resulting in significantly higher currents at the higher bias relative to those at lower ones. Note that the bias-induced shift of the molecular orbitals results in a shift of transmission peaks, as shown in

Figure 3.3. These results are consistent with previously reported theoretical studies on C_{60}[74,75].
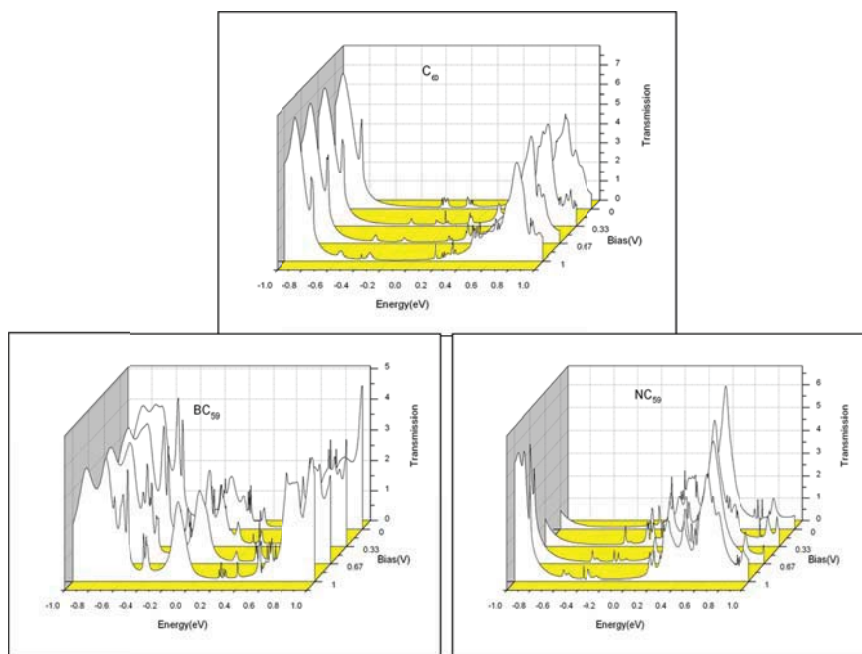
Figure 3.3 The bias-dependence of transmission functions of C_{60}, BC_{59} and NC_{59}. Zero of the energy is aligned to the Fermi energy.

Figure 3.2 also shows the *I-V* characteristics of B and N doped fullerenes, where substantial device conduction was predicted for BC_{59} at higher bias. Specifically, the current rises at a much faster rate for BC_{59}. Also, the magnitude of the current (I) for BC_{59} at a higher bias voltage, (e.g. 2V), is significantly higher than those in other fullerenes (Figure 3.2). In the low-bias range (<1V), the current remains nearly the same in the pristine and doped fullerenes (Figure 3.2). It appears that the role of the substitutional B is significantly different from either substitutional N or encapsulated B and N in the cage in determining the electronic transport properties of the doped fullerenes.

Analysis of transmission functions indicates that the atomic dopants at the endohedral site in the cage contribute to the formation of HOMOs and LUMOs in B@C_{60} and N@C_{60}. There exist inter-band states induced by B and N in the vicinity of the Fermi level (as also seen in the calculated density of states - not shown here). Boron appears to couple with contact Au atoms, whereas Nitrogen couples with the C atoms in the cage to form the states near the Fermi energy. We note that the charge transfer between the endohedral dopants (B, N) and the fullerene cage is found to be negligibly small.

For BC_{59}, an examination of the transmission functions (

Figure 3.3) reveals the appearance of diffusive transmission peaks near the Fermi region. This is further confirmed by the calculated density of states. Interestingly, the molecular orbitals near HOMO of BC_{59} and NC_{59} are dominated by the contact Au orbitals. Moreover, the peak at ~ -0.6 eV for BC_{59} is rather delocalized within the gold contact leading to a very diffusive transmission without showing a distinguishable peak. One can then conclude that the coupling of the Au contact and BC_{59} opens the electron transport channels due to the delocalized Au-B hybrid states, resulting in rather high currents for the case of substitutional B relative to the case of substitutional N in the fullerene cage. A stronger tendency of boron molecular orbitals to hybridize with Au orbitals has been shown to be due to the electron deficient nature of B in our previous studies on the electronic transport of boron nanostructures[76].

It is tempting to interpret the calculated results of the effect of the B and N substitutions on the I-V characteristics of fullerene in terms of the bulk semiconductor physics. The considerably larger magnitude of the current for BC_{59} relative to NC_{59} at higher bias voltages suggests that the doped fullerene molecule shows a better "hole" conduction than "electron" conduction. Although, the present study focuses on the calculations of current due to "electron transport", the ease of "hole" conduction over electron conduction in doped fullerene can be also understood from the electronic structure and electron transport of the pristine fullerene. The electrons in the hexagonal carbon rings are known to be highly localized and do not lend themselves easily to participate in electron transport. Thus the fullerene molecule does not offer sufficient electron charge

41

carriers for transport. Any additional electron, for example the one available from the substitution of a C atom by N thus acts as an electron trapped on a semiconductor quantum dot, yielding non-vanishing – albeit small - current. Substitution by an electron deficient atom, such as B, which creates a hole in fullerene structure, attracts electrons from the adjoining carbon atoms as well as the metal electrodes in the bonding region, which in turn move easily at higher external bias. Thus, a hole assisted electron transport mechanism in B-doped (p-type) fullerene appears to provide a higher electron conductivity. This suggests that fullerene can be an attractive candidate for p-type (B-doped) nanoelectronic devices.

The transport properties of substitutional fullerenes, BC_{59} and NC_{59}, were also studied previously[77]. The DFT-based calculations using the contact-fullerene distance of ~3.5 Å find a non-linear I-V characteristic for the doped fullerenes in the bias window of 0-1V. On the other hand, similar calculations[77] on BC_{59} and NC_{59} find that doping by B and N leads to a higher HOMO-LUMO gap and a smaller tunneling current with respect to that in the pristine fullerene. These findings are in marked contrast with the findings of the present study, which suggests the presence of mid-gap states associated with dopants in the HOMO-LUMO gap of C_{60}. It should be pointed out that the previous study[77] used asymmetric electrode architecture - considering three layers of Au (100) in the left lead and two layers of Au (100) in the right lead in the device architecture with the contact-fullerene distance to be 2.1 Å. Therefore, we suggest that the results of their calculations may be an artifact of the device model used in their calculations.

3.4 Summary

In an attempt to understand the effect of atomic-level changes on electronic structure and electron transport of molecular and nano-scale architecture, we have performed first-principles electronic structure calculations on C_{60} and its B and N doped derivatives. The cage structure of C_{60} allowed two different configurations, namely - endohedral ($B@C_{60}$ and $N@C_{60}$) and substitutional BC_{59} and NC_{59} – to be investigated. The calculated results clearly reveal that at the nanoscale, even a single atom change in the structure brings noticeable changes in the electronic and geometrical structures. Further, the

electron transport property of the nanoscale system gets substantially modulated by a single-atom change in the structure. Specifically, B and N doping of fullerene appears to lead to higher current than the pristine fullerene. However, the substitutional derivatives, BC_{59} and NC_{59}, in which the dopant atom occupies a site previously occupied by a C atom on C_{60} wall, give higher magnitude of current than the endohedral derivatives, $B@C_{60}$ and $N@C_{60}$. This is attributed to the dominance of hybrid states involving the contact gold atoms in forming the molecular orbitals near the Fermi region, which opens new transmission channels for the substitutional dopants. Finally, the calculations predict a much higher value of current for BC_{59} compared to all other species considered here, suggesting its application as an effective p-type semiconductor in electronic devices.

Chapter 4   Bilayer Graphene Nanoribbons - Stacking Dependent Electronic Structure and Transport Properties[2]

4.1 Introduction

A bilayer (b) graphene nanoribbon (GNR) system consists of two monolayers of GNR, typically arranged in the Bernal (AB) or AA stacking arrangements. Such a bilayer system with smooth edges has been successfully fabricated by unzipping multiwalled CNTs [78], by plasma etching [79] and chemical route [80]. It can be a channel material for a field-effect transistor due to the opening of its gap by a perpendicularly applied electric field [81-83]. It has been suggested that the application of bGNRs in nanoscale electronic devices is advantageous due to their low sensitivity to external perturbations [84]. Therefore, the unique electronic properties offered by a bilayer GNR system can add another dimension to the possibility of the use of carbon-based transistors in the post-silicon era.

In a bGNR configuration, the stacking of hexagonally linked sp^2-bonded nanoribbons facilitates an interlayer interaction between π electrons which leads to the modification of its electronic properties relative to those of monolayer nanoribbons. Also, similar to the single-layer GNR, the edge chemistry is expected to have profound effect on the electronic properties of bGNR. For example, a GNR with homogeneous armchair or zigzag shaped edges is predicted to have finite gaps in the ground state, with the edge states forming the top of the valence band and the bottom of the conduction band [85]. Furthermore, this gap appears to scale inversely with the width of the GNR [85]. Such an interesting electronic structure of the GNR in general and bGNR in particular has attracted a great deal of attention in their electron transport properties [79,86-89]. For the bGNR, in particular, the electron transport studies have been performed using a part of the channel-forming single-layer GNR as a contact [90,91]. Such a configuration has limited practical applications as it has the potential of introducing unwanted asymmetry in the

---

[2] Chapter 4 is reprinted with permission from (Carbon, 50, 784 (2012)). Copyright (2012) Elsevier. See Appendix D for documentation of permission to republish this material.

structure. In the present study, we investigate the role of interplanar interaction in determining the transport properties of a bilayer GNR system by considering a practically realizable device configuration in which GNRs are suspended between gold electrodes. Thus, the device configuration considered in the present study is capable of exploiting the presence of the transmission channel due to the interlayer interaction between GNRs and the effect of interface between GNR and metal electrodes for electronic transport.

4.2 Computational Model

The local spin density approximation (LDA) of the exchange [92] and correlation functional [93] forms within density functional theory, incorporated in the SIESTA program package is used [56]. It should be pointed out that the LDA-DFT method has been shown to provide reasonably good descriptions of the physics and chemistry of graphitic systems [94,95], though it underestimates the band gap of the semiconducting materials. Enhanced conductivity features in the current-voltage characteristics of the bilayer GNR configuration considered are clearly demonstrated by the LDA-DFT method employed. It is worth noting that the LDA-DFT method mimics features of the electronic band structure obtained by many-electron Green's function approach within the *GW* approximation reasonably well [96].

Norm-conserving pseudopotentials and double-zeta basis sets with polarization functions were used for all atoms in electronic structure calculations [56]. The k-space integration was done with a grid of 1x1x32 k-points. For the contact Au atoms, the chosen Au pseudopotential and basis sets reproduce the electronic properties of the bulk Au near the Fermi region and has been successfully applied to investigate electronic transport properties of the Au-C_{60}-Au system [1].

The bias-dependent electron transmission and current are calculated using the non-equilibrium Green's functional (NEGF) method based on the Keldysh formalism, see Chapter 3 for details.

4.3 Results and Discussion

4.3.1 Structural Properties

A bilayer GNR configuration consisted of hydrogen passivated zigzag graphene nanoribbons (zGNR) with a width of 13.4 Å is considered. It has six primitive cells of graphene and is denoted as 6-zGNR. In a zGNR, the ribbon edges order magnetically due to localization of the unpaired electrons. A parallel alignment of the spin states of both edges results into the ferromagnetic (FM) spin configuration, whereas anti-parallel alignment yields the antiferromagnetic (AF) spin configuration. The calculated ground state of a pristine 6-zGNR has AF ordering between two edges, though the coupling between carbon atoms on the same edge is ferromagnetic.

The calculated results on pristine 6-zGNR employing our modeling elements agree very well with the previously reported results [85,97,98]. For example, the energy difference between AF and FM coupling of edges is about 0.006 eV per 6-zGNR cell which is comparable with 0.004eV per cell predicted for 8-zGNR [85]. Note that ref. 11 uses the same computation method as we do, and it is shown this energy difference decreases with zGNR width. The calculated C-C bond length varies from 1.39 Å to 1.45 Å as also predicted in earlier studies. The magnetic moment of the edge carbon atoms of bare zGNR is about 1.16 μ_B. This magnetic dipole is dramatically suppressed (≈ 0.2 μ_B) in the presence of passivating hydrogen atoms. Since the bare (i.e. edge unpassivated) bilayer configuration of zGNRs is predicted to be unstable [99], we consider a bilayer configuration consisting of hydrogen passivated GNRs which are shown to thermodynamically stable [85,97-100]. A full optimization of the pristine bilayer GNRs with smooth edges led to formation of (6, 6) single-wall armchair CNT as also reported previously [99].

Following the stacking nomenclature of graphite, we classify the stacking arrangements to be either AA or AB as shown in Figure 4.1; all carbon atoms of the hexagon rings are near-neighbors (i.e. top of each other) in the AA stacking whereas only half of the atoms are near neighbor and the other half of the atoms are above and below the empty centers of the hexagonal rings of GNR in the Bernal (AB) configuration. The AA bilayer only

has one form of edge alignment whereas AB has two types of edge alignments, namely α and β alignments. Previous studies [100-102] have shown the α alignment to be energetically more stable and non-magnetic whereas the energetically less favorable β alignment does have magnetic properties [103] which can be explained by Stoner's criteria for itinerant magnetism.
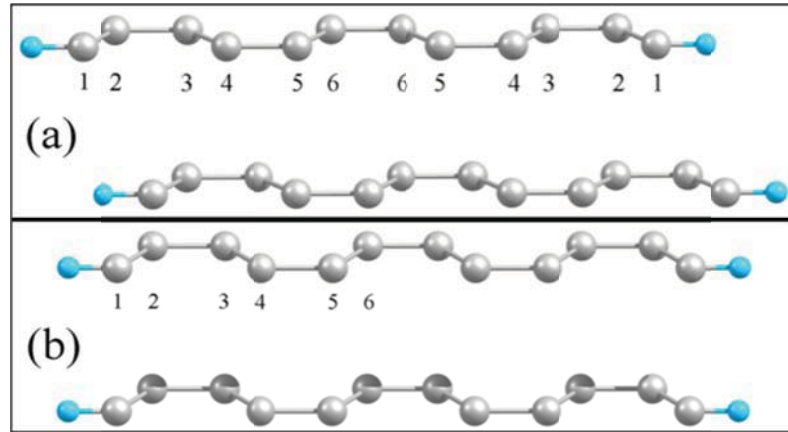

Figure 4.1 Bilayer GNR configurations (a) AB and (b) AA. (C in grey and H in blue).

The calculated results confirm the AB-α stacking arrangement to be energetically preferred for the passivated bilayer zGNRs, though the energy difference between AA and AB-α is relatively small (≈0.03 eV/atom) at the LDA-DFT level of theory. The calculated value of the binding energy of the AB-α configuration is 0.018 eV/atom in excellent agreement with the previously reported value of 0.017 eV/atom [102]. The AA stacking arrangement consisting of individually optimized 6-zGNR is predicted to be non-magnetic with an interlayer separation of 3.06 Å and binding energy of 0.015 eV/atom. We define the binding energy to be the difference between the total energy of a bilayer and twice the value of the total energy of a passivated (AF) single-layer zGNR.

4.3.2 Electronic Properties

Figure 4.2 shows the electronic band structures of single-layer and bilayer 6-zGNRs along the high symmetry points in the k-space suggesting that the presence of the interlayer coupling significantly modifies the subband curvature and subband spacing of the AA stacking configuration relative to those for the AB stacked GNRs and the single-

layer GNR. Note that our calculated band structures for the AB-α bilayer configuration are consistent with the results of previous theoretical study [102]. It is noted recently using generalized gradient approximation, it is found that ferromagnetic and antiferromagnetic configurations for both the intralayer and interlayer spin arrangements give the lowest energy in all considered magnetic models. However, in our calculation all magnetic states converge to the non-magnetic one, suggesting the spin states are functionally dependent.

In the band structure of the passivated zGNRs, only π edge states exist due to the saturation of dangling edge bonds by hydrogen atoms (Figure 4.2 (top)). The calculated projected density of states (PDOS) of zGNR whose qualitative features agree well with the previous LDA-DFT calculations [96] is shown in Figure 4.3. We find that the peaks near Fermi level can be attributed to edge atoms suggesting that the electronic bands near the Fermi energy are composed of π edge states of the zGNR. The localized nature of these π edge states leads to magnetic instability in the system which opens up gap in the band at Fermi energy. It is expected that a graphene nanoribbon with sufficiently large width is likely to mimic the band structure of a graphene sheet with zero band gap.

For the AB-α bilayer configuration, the stacking sequence facilitates the interlayer coupling which leads to a significant energy dispersion of electronic bands near the Fermi surface relative to that for the single-layer GNR, though the band gap changes from 0.35 eV for single-layer GNR to 0.29 eV for the bGNR. This is in contrast to that of the AA-stacked bilayer configuration where two degenerate p_z-subbands associated with each single layer cross at the Fermi level yielding a finite density of states near Fermi energy (Figure 4.3).

The magnetic properties of the monolayer GNR are eliminated in the AA and AB-α GNRs leading to nonmagnetic ground state of both bilayer configurations. The presence of the interlayer interaction between GNRs appears to shift the peaks originated from the edge states away from the Fermi level (Figure 4.3 (right)); the shift is relatively larger for the AA stacking arrangement relative to that of the AB-α stacking arrangements.

This effect is more pronounced in the AA stacking of GNRs because of significant interlayer bonding between all carbon atoms on top and bottom GNRs. In contrast, only half of the carbon atoms in the AB stacking of the bGNR interact significantly.
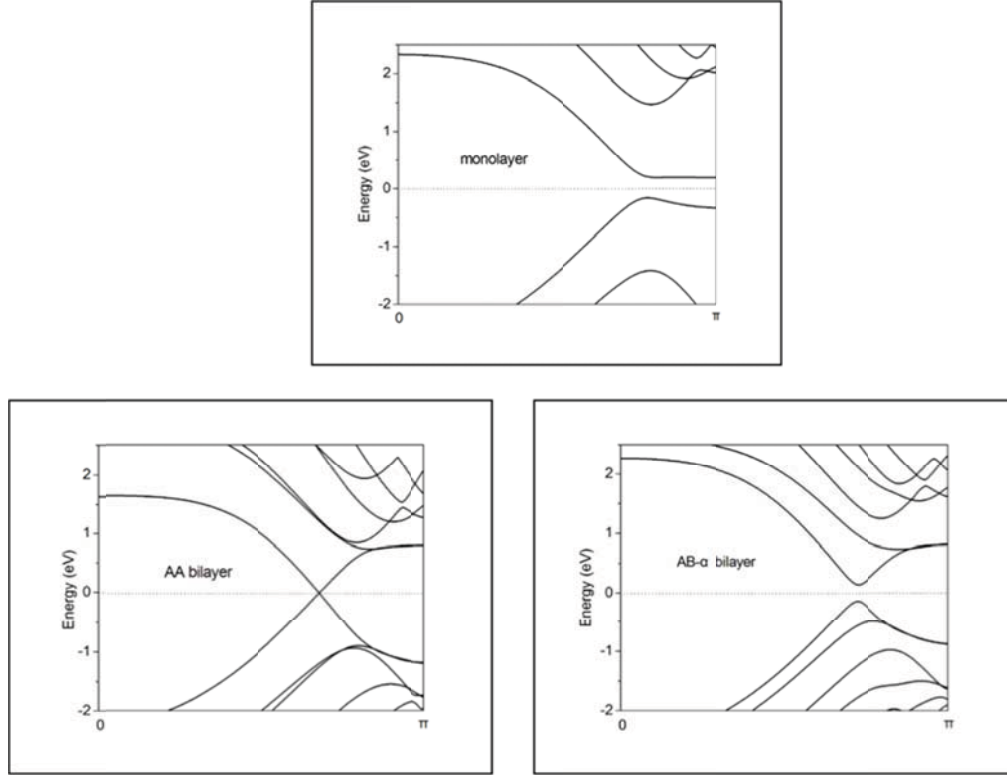

Figure 4.2 The electronic band structures of passivated zGNRs : (top)single-layer GNR, (bottom left) AA bGNR, and (right) AB-α bGNR. Zero of the energy is aligned to the Fermi energy.

Thus, as expected, the AB-α stacking has an interlayer coupling strength between the AA stacking and the single-layer GNR. Consequently, the single-layer GNR has a finite gap and is magnetic, the AB-α stacked bilayer has a finite gap and is non-magnetic, and the AA stacked bilayer GNR is non-magnetic with zero gap. The difference between AB and AA stackings can also be thought of in an analogy way. In AA stacking case each edge of a monolayer constituent (totally 4 edges) can interact with the edge of another layer on the same side, thus decreases the degree of unsaturation, making the bilayer structure more like a rolled graphene sheet without edges. In AB stacking case, none of the 4 edges decreases the unsaturation, so it is more like a simple stacking of two independent monolayer GNRs.

49
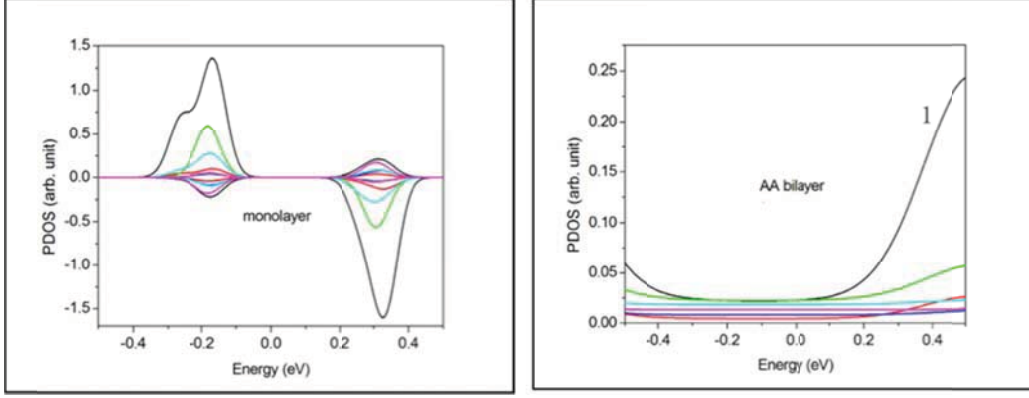
Figure 4.3 Density of states(DOS) projected on carbon atoms of passivated zGNRs: (left) single-layer GNR, (right) AA bGNRs. Black, red, green, blue, cyan and magenta represent the PDOS of the 1st, 2nd,…, 6th carbon atom counted from ribbon border to the central region. The magnitude of PDOS decreases as we move away from edge atom (1). See, Figure 4.1. For the case of single-layer GNR, both spin up and spin-down components of PDOS are shown. Zero of the energy is aligned to the Fermi energy.

In order to investigate the evolution of the band structure of the AA GNRs due to interlayer interactions, we calculated the changes in the band structure with the change in the interlayer spacing of the AA bilayer configuration.

Figure 4.4 The electronic band structures of the AA bGNRs as a function of the interlayer spacing. Zero of the energy is aligned to the Fermi energy.

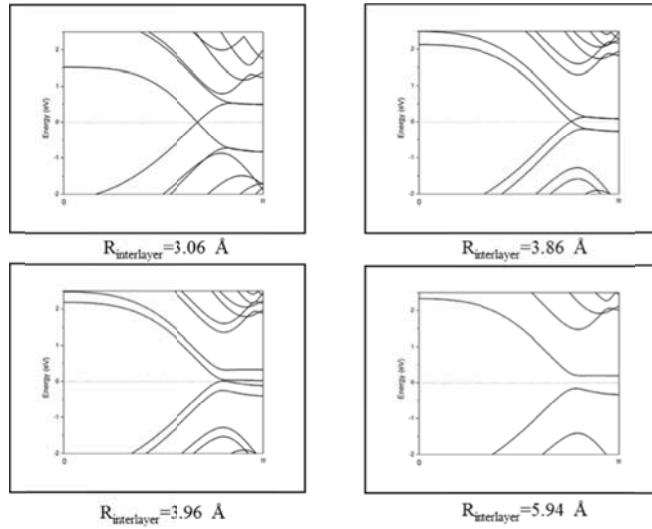For a large interlayer spacing of 5.94 Å, each band is two-fold degenerate due to negligible interaction between the two passivated single-layer GNRs. The calculated band gap is the same as that of the single-layer GNR. As the interlayer separation between the GNRs decreases, the coupling between the two begins to dominate in determining the band structure; eventually leading to the crossing of linear valence and conduction bands at the Fermi level (Figure 4.4).

4.3.3 Transport Properties

The Au (111) surface is chosen to be the contact lead for transport calculations since its lattice parameter matches well with that of the GNR, thus minimizing the interfacial lattice distortions in the device configuration. The lattice vector 'a' of Au (111) has a length of 5.00 Å, while the double length of GNR shown as vector 'b' is 4.92 Å, as shown in Figure 4.5. There exists a weak interaction between the gold contact and the passivated GNR. Consequently, Au atoms do not lead to charge transfer or doping in GNRs as also reported previously [104].
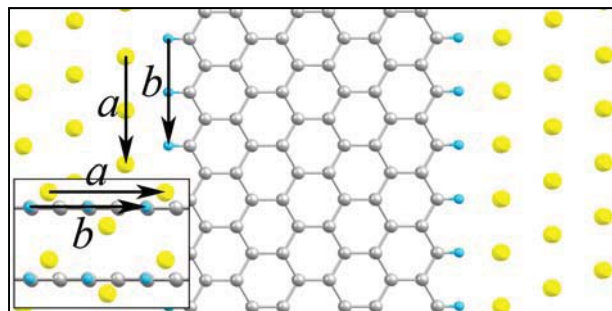
Figure 4.5 A top view of the suspended passivated AA bGNR coupled with semi-infinite bulk gold electrodes. The distance between GNR and gold is 2 Å, while the distance between two gold electrodes is 17.4 Å. The insert shows the lattice matching of GNR and gold leads. Symbols: C in grey, H in blue, and Au in yellow.

The *I-V* characteristics of the AA bilayer and monolayer configurations are shown in Figure 4.6. The results predict substantial device conduction for AA relative to that of the monolayer. This is consistent with the calculated band structure and density of states of these configurations. The calculated current of the AA bilayer equilibrium configuration

at a given bias cannot be regarded as a sum of current due to individual GNRs. At a relatively large interlayer spacing (~6 Å), the calculated current is indeed approximately twice the current calculated for a monolayer passivated GNR (Figure 4.6). We notice that the increase in the interlayer spacing does not change the details of gold contacts with the GNRs, keeping the interfacial configurations to be the same. We have also calculated the electronic transport properties of the AB bilayer configuration predicting a much smaller current compared with the AA-stacked bilayer at a given bias. Considering the asymmetric coupling to electrodes on the left and right side of each layer of GNR for the AB bilayer, a larger vacuum gap acts as a higher energy barrier decreasing the current at a given bias.
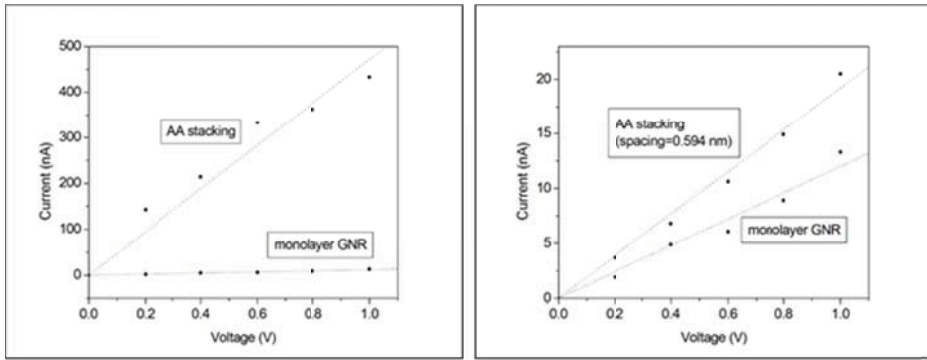
Figure 4.6 I-V characteristics of the single-layer GNR and the AA bGNR (left) AA bGNR with the equilibrium interlayer spacing of 0.306 nm, (right) AA bGNR with a large interlayer spacing of 0.594 nm.

Analysis of transmission functions shown in Figure 4.7 confirms the role of interlayer coupling in facilitating the transmission channel for the AA stacking arrangement for the passivated zGNRs. An additional inter-band state appears in the vicinity of the Fermi level with a decrease in the interlayer separation of the bilayer GNRs. Thus, the interlayer interactions mainly due to delocalized electronic states in the AA stacked bilayer appear to play a critical role on the metal-like conducting behavior of these GNRs.

Figure 4.7 The transmission function of the AA bGNR at zero bias: (i) (dotted line) interlayer spacing=0.594 nm and (ii) (solid line) interlayer spacing=0.306 nm. Zero of the energy is aligned to the Fermi energy.

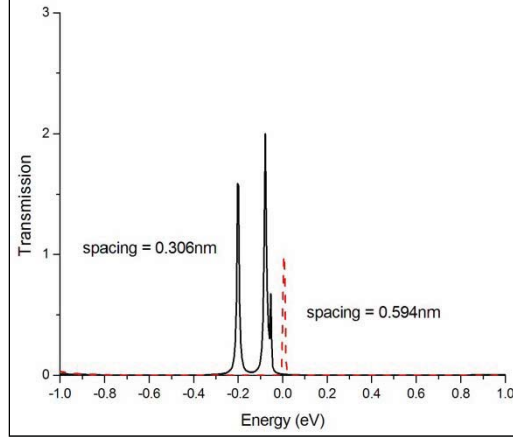We note there is a recent work by Sun [105], with a contact model similar to ours using the tight-binding method. In a recent paper, based on tight-binding method it was argued that the conduction of AB BGNR is larger than that of AA BGNR at small bias voltage, due to a higher DOS at Fermi level. However, the cited Nakada's work (ref (22) in Sun's paper) which supports Sun's argument is somewhat out of date. When spin-polarization is taken into account, both monolayer zGNR and bilayer AB zGNR are found to have a finite gap. We think the difference in our work is due to the considered spin polarization, which induces an opening of energy gap in AB BGNR.

4.4 Summary

First principles electronic structure calculations together with non-equilibrium Green's Function method were performed on a bilayer GNR system in two different stacking arrangements. The calculations reveal that a bilayer GNR system in the AA stacking configuration exhibits substantially enhanced electron transmission as well as tunneling currents compared to single-layer GNRs. The AA bGNR system has a non-vanishing transmission near Fermi energy. In contrast, either a single-layer or AB-α bilayer GNRs has a large transmission gap. The calculated enhanced conducting features of the AA bilayer are closely related to the interacting π-orbitals of the two GNRs. Considering that the graphene bilayers with the AA stacking configuration can be synthesized [106], their

53

predicted enhanced conductivity can play an important role in the development of future nanoscale electronic devices.

Chapter 5   Graphene/h-BN Hybrid Structure – the Effect of Strain[3]

5.1 Introduction

The hexagonal boron nitride (h-BN), with a similar lattice constant but different boron and nitrogen sublattices is suggested to be a suitable choice as a substrate to introduce the inequivalence in the graphene lattice. This inequivalence is expected to induce a finite energy gap in graphene in the ground state, which is important for device applications. On the other hand, the choice of SiC [15,107,108] or the O-terminated SiO_2 substrate [109] was found to introduce a non-zero gap of about ~0.2 eV in graphene. Furthermore, theoretical calculations based on tight binding model have investigated the influence of electric field on the band structure of a graphene/BN bilayer predicting an increase in its energy gap [110].

Considering that the presence of strain can also affect the electronic properties of a given system, in the present study, we propose to investigate the effect of strain applied to a graphene/BN bilayer on its energy gap. We will also examine the role of interplanar interaction in determining the electronic properties of a bilayer system by comparing the results of graphene/BN with a BN bilayer. Note that both theoretical and experimental studies have investigated the effect of intraplanar strain on the electronic properties of a graphene monolayer reporting the shift of the Fermi crossing away from the high-symmetry k points [111-113].

5.2 Computational Method

Total energy calculations were performed in the framework of the local density approximation of the exchange and correlation functional to density functional theory (LDA-DFT) as implemented in the SIESTA computational code[114]. We make use of

Troullier–Martins pseudopotential[115] and double-ζ basis sets with polarization functions for all atoms. The calculated equilibrium configurations associated with the graphene/BN and BN bilayers are fully relaxed, with residual forces smaller than 0.01 eV/Å.

The graphene/BN bilayer consists of a stacking of one BN monolayer and one graphene monolayer, both of a sp^2-bonded hexagonal structure. Following the stacking nomenclature of graphite, we define the arrangements to be AA (i.e. C atoms are on top of either B or N atoms of the BN layer), AB(nitrogen) (i.e. one C atom is on top of a N atom and the other C atom is on top of the center of the hexagon of the BN layer), and AB(boron) (i.e. a C atom is on top of a B atom and the other C atom is on top of the center of the hexagon of the BN layer). Similarly, the stacking arrangements in a BN bilayer are AA (i.e. B_I is positioned at top of B_{II} and N_I is positioned at top of N_{II}), AA' (i.e. B_I is positioned at top of N_{II} and N_I is positioned at top of B_{II}), AB(boron) (i.e. B_I is on top of B_{II} , while N_I is on the center of hexagon of the second BN layer), AB(nitrogen) (i.e. N_I is on top of N_{II} , while B_I is on the center of hexagon of the second BN layer), and AB (i.e. B_I is on top of N_{II} and N_I is on top of the center of hexagon of the second BN layer). Here, the subscripts I and II refer to the atoms associated with first and second layers of BN, respectively. The stacking configurations considered for graphene/BN and BN bilayers are shown in Figure 5.1.
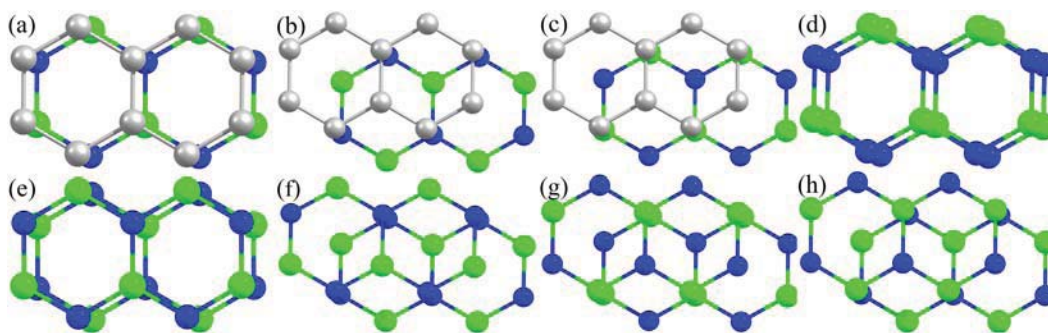

Figure 5.1 A schematic diagram of the stacking arrangements considered for graphene/BN and BN bilayers. The grey, green and blue represent carbon, boron and nitrogen atoms, respectively.

5.3 Results and Discussion

5.3.1 Structural Properties

Figure 5.2 shows a representative calculated energy surface for the graphene/BN and BN bilayers where a variation in the interplanar separation is used to represent the strain applied to the bilayer along the vertical direction.
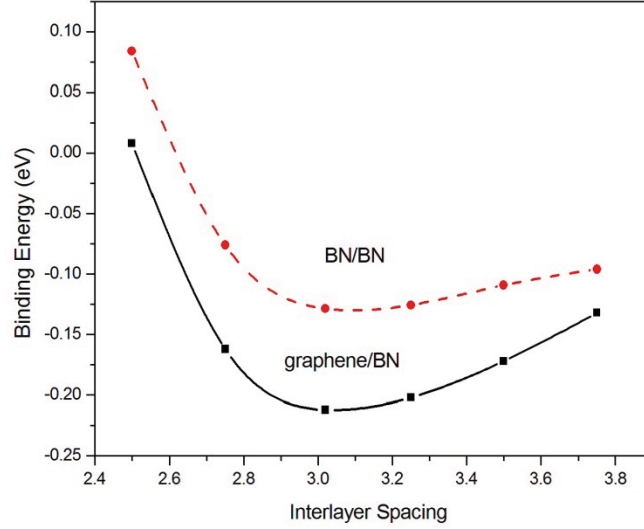

Figure 5.2 Binding energy (E_B) vs. interlayer separation (Z) for graphene/BN and BN bilayers of the lowest energy stacking patterns (panel (a) and panel (h) in Figure 5.1).

The calculated structural parameters, namely intraplanar bond length (i.e. near-neighbor distance, R) and interplanar separation, Z together with the binding energy (E_B) of the graphene/BN and BN bilayers are given in Table 5.1. E_B is defined as total energy of a bilayer minus the sum of total energies of corresponding constituent monolayers. At the LDA-DFT level of theory, the total energy of a graphene and BN monolayer is -310.436 eV and -350.872 eV, respectively. We note that monolayers of BN have been fabricated with an aim to explore their potential applications in electronics [116,117].

For the graphene/BN bilayer, the calculated results predict the AB (boron) stacking arrangement to be energetically preferred, though the energy differences between the AB (boron) and other two are relatively small (~0.01 eV/atom). In the equilibrium AB (boron) configuration, the interplanar spacing is 3.022 Å and the intraplanar bond length (for both R_{B-N} and R_{C-C}) is 1.429 Å.

It is to be noted here that calculations find the AB stacking configuration (R = 1.422 Å, Z

= 3.022 Å, E_B = -0.24 eV) to be energetically preferred over the AA configuration (R = 1.423 Å, Z = 3.225 Å, E_B = -0.186 eV) for the graphene bilayer.

Table 5.1 Structural properties of the bilayer systems: graphene/BN, and BN.

System	Label (Figure 5.1)	Stacking configuration	Binding energy (eV)	(intraplanar) Bond length, R (Å)	Interplanar separation Z (Å)
graphene/BN	a	AA	-0.168	1.427	3.208
graphene/BN	b	AB(nitrogen)	-0.171	1.427	3.244
graphene/BN	c	AB (boron)	-0.207	1.429	3.022
BN/BN	d	AA	-0.101	1.437	3.429
BN/BN	e	AA'	-0.129	1.437	3.103
BN/BN	f	AB	-0.133	1.438	3.071
BN/BN	g	AB(nitrogen)	-0.099	1.438	3.357
BN/BN	h	AB (boron)	-0.128	1.438	3.065

Our results are in agreement with the previous theoretical results obtained for graphene on the h-BN substrate where the AB (boron) stacking arrangement was found to be preferred over the other two stacking arrangements at the LDA-DFT level of theory [17].

For the BN bilayer, the AB stacking arrangement is predicted to be the optimal configuration which is closely followed by the AA' and AB (boron) stacking arrangements. The calculated R_{B-N} remains nearly the same for all the stacking arrangements whereas the calculated interplanar separation does vary with the stacking arrangements. The calculated R_{B-N} of 1.44 Å for the BN bilayer is slightly different from the typical value of 1.42 Å in the sp^2 network of carbon atoms. Note that the calculated R_{B-N} of about 1.45 Å for the monolayer BN is in agreement with the results of the previous theoretical studies [118-122].

The AA' stacking configuration of the BN bilayer reflects the atomic arrangement of the bulk h-BN for which the experimental values of the lattice constants, a and c are 2.505 and 6.662 Å, respectively[123]. In the AA' stacking configuration, the calculated values of a and c are 2.489 and 6.206 Å, respectively, indicating that a BN bilayer system may not be appropriate to simulate the structural properties of the bulk h-BN.

5.3.2 Electronic Structure

Band structures of the energetically preferred stacking arrangements for graphene/BN and BN bilayers (i.e. AB (boron) and AB for graphene/BN and BN bilayer respectively) along the high symmetry points in k-space are shown in Figure 5.3. In the graphene/BN bilayer, we find that the bands near Fermi level have characteristic graphene like features with linear dispersion. The degeneracy of bands at the so-called Dirac points, K and K' appears to be lifted leading to an energy gap of about 0.12 eV. This is in contrast to the case of the BN bilayer where a direct energy gap of about ~4.3 eV at K in the k-space is predicted.
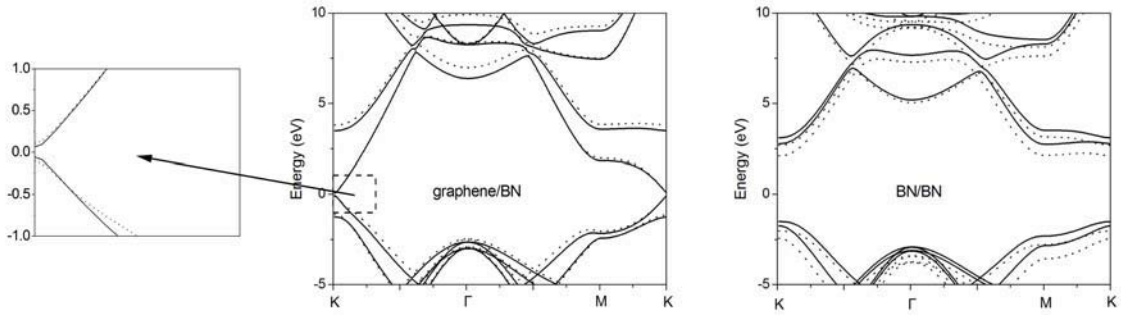

Figure 5.3 Band structure of the equilibrium (solid lines) and strained (dotted lines) configuration of graphene/BN and BN bilayers. The left panel shows the band structure near K point.

The opening of energy gap in graphene/BN can be attributed to the interplanar interaction between graphene and BN monolayers. Carbon atoms in graphene appear to experience a slightly different electrostatic potential due to inhomogeneous charge distribution present in BN, thus making them to be inequivalent[6]. This is confirmed by the valence band charge density plots of the constituent BN and graphene monolayers (Figure 5.4). The valance band charge density contours of BN monolayer consists of a pattern of curved triangles, reflecting the different electronegativity of boron and nitrogen. Indeed, the charge density around nitrogen is about three times as that around boron. In contrast, the charge contours of graphene monolayer reveal near similarity of two carbon sublattices. On the other hand, neutral pristine graphene bilayer bulk is gapless [124] while a gap can be opened if the symmetry of two carbon monolayers is broken, e.g., in presence of a transverse electric field [125].
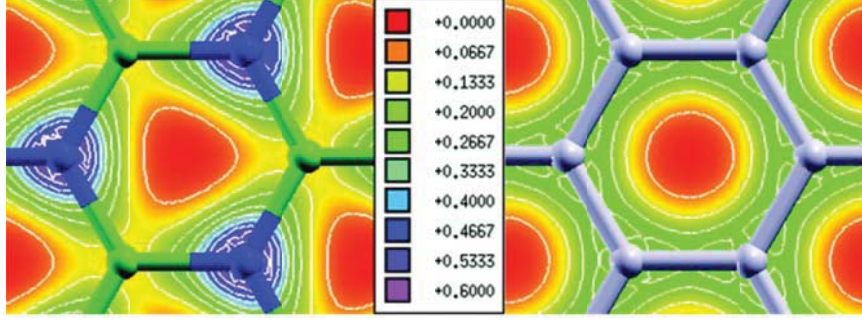
59

Figure 5.4 The valance band charge density contours of BN (left) and graphene (right) of the graphene/BN bilayer. The central panel shows the scale of charge density, in unit of $e^-/Bohr^3$.

A large energy gap predicted for the BN bilayer is due to the partial ionic character of the chemical bond between boron and nitrogen in the lattice. In the equilibrium configuration, the interplanar interaction appears to slightly reduce the energy gap of the BN bilayer relative to that calculated (~4.5 eV) for the BN monolayer.

LDA approximation within DFT frame generally underestimates the bad gap, so the band gaps calculated here are more semiquantitative. Nevertheless, the different reasons causing the gap variation in graphene/BN and BN/BN bilayers, as well as the gap variation feature under strain are clearly demonstrated at the LDA level.

5.3.3 Strain-modulated Band Structure

In the following, we restrict ourselves to investigate the effect of small strains (≤10%) on the band structure considering that small strains are not likely to lead to significant distortions in the atomic arrangements in the constituent monolayers. For example, the monolayer BN is found to be slightly buckled in graphene/BN; the difference in the Z-coordinate (i.e. c-axis perpendicular to the plane) of B and N is ~0.008 Å with B moving towards the graphene. The simulated pressure is perpendicular to the intraplanar C-C bonds, and magnitude of the strain was simulated by varying the interplanar separation, Z in graphene/BN and BN bilayers.

Figure 5.5 shows the variation of the band gap at K with the strain for graphene/BN and BN bilayers. The nature of the strain-modulated gap at K in the *k*-space for graphene/BN

is significantly different from that exhibited by the BN bilayer.

For the graphene/BN bilayer, the strain increases the strength of the interaction between the constituent monolayers which, in turn, increases the energy gap at the k-point of K. For small strains considered, the relationship is predicted to be linear; the gap is about ~0.2 eV for ~9% strain applied along the c-axis.

At the equilibrium configuration of graphene/BN, the upper valence band is dominated by C-p_z orbitals leading to linear dispersion of the π band near the Fermi level. A higher degree of interplanar interaction leads to somewhat flattening of bands near the Fermi level which can be attributed to the change in the nature of the upper valence band. Note that the projected density of states of graphene/BN (not shown here) finds an increased contribution from N-p_z orbitals in forming the upper valence band with increase in the strain.

The calculated results do not show such a drastic variation in the band gap of the BN bilayer with the increase in the strain; the band gap at K is slightly decreased for ~10% strain relative to that for the equilibrium configuration. For the BN bilayer, the upper valance band is composed of the N-p_z orbitals whereas the lower conduction band is dominated by B-p_z orbitals. Their positions with respect to Fermi level remain nearly the same in the *k*-space for small strains considered. Note that our calculated values of the c-axis compressibility in units of $(10^{-12}$ cm^2/dyne$)$ are 2.92 and 3.31 for graphene/BN and BN bilayers, respectively as compared to the experimental value of 2.44 $(10^{-12}$ cm^2/dyne$)$ for the c-axis compressibility of the graphite crystal at 0K [126].

5.4 Summary

The LDA-DFT level of theory predicts the equilibrium configurations of graphene/BN and BN bilayers to be AB (boron) and AB stacking configurations, respectively. The calculated band gaps are 0.12 and 4.3 eV for graphene/BN and BN bilayers in their energetically preferred equilibrium configurations. The strain-induced modulation of the band gap is investigated by varying the interplanar separation of the constituent monolayers.
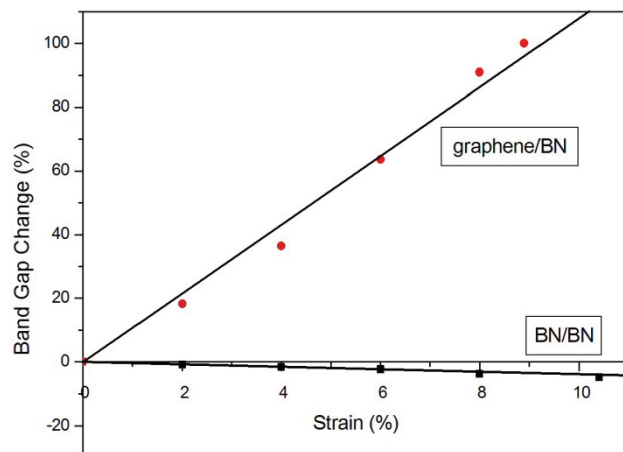
Figure 5.5 Variation of the band gap with the perpendicular strain applied in graphene/BN and BN bilayers.

The magnitude of the band gap appears to be directly related to the uniaxial strain applied along the c-axis for the graphene/BN bilayer. On the other hand, the band gap of BN bilayer remains nearly the same for small strains considered. The increased inhomogeneity of different carbon sublattices due to a stronger interplanar interaction is likely to be cause of larger band gaps at higher strains applied for the graphene/BN bilayer.

Chapter 6   Graphene/h-BN Hybrid Structure – the Effect of Electric Field[4]

6.1 Introduction

There appears to be sufficient progress in fabricating the graphene/BN hybrid configurations with the expectation that these hybrid structures may deliver alternative device configurations that a single-layer graphene doesn't. Liu *et al.*[127] have reported chemical vapor deposition of h-BN on graphene. The fabricated graphene-BN films have thicknesses of about two to a few layers. On the other hand, Dean[22] and Tang[128] have also deposited graphene on the h-BN. Very recently Britnell *et al.*[129] reported the fabrication of a graphene-based device where up to 30 layers of h-BN were sandwiched between two graphene monolayers. Such vertical graphene heterostructures were shown to act as an effective field-effect tunneling transistor with a room-temperature switching ratio of about 50[129]. Theoretically, it has been predicted that there appears a relationship between the band gap tunability and the number of h-BN layers representing the h-BN substrate in the presence of an external electric field for a bilayer graphene system[130].

Trilayer graphene has also been shown to exhibit stacking-dependent electronic properties under the influence of a perpendicular electric field, with the semiconducting ABC stacked trilayer showing a large tunable gap relative to the metallic ABA stacked trilayer[131-133]. While monolayer graphene keeps its gapless feature in the presence of perpendicular electric field, a BN/graphene/BN trilayer system shows stacking dependent energy gap tunability[20,134,135].

In this study we consider a graphene/BN/graphene trilayer system to investigate the effect of an inserted layer of BN on the electronic properties of the bilayer graphene with and without a perpendicular external electric field. We find that the graphene/BN/graphene trilayer shows a negligible energy gap regardless of the stacking configurations

considered. However, this hybrid trilayer system exhibits interesting stacking dependent gap tunability under the application of the perpendicular external electric field.

We performed electronic structure calculations at the level of van der Waals-density functional theory (vdW-DFT) on trilayers composed of graphene and BN, predicting their stacking-dependent stability, electronic and transport properties under an applied external perpendicular electric field. Note that we have also considered a few selective configurations of the BN/graphene/BN trilayer system to perform the electronic transport calculations which have not been reported previously. Furthermore, use of the vdW-DFT level of theory is expected to provide accurate descriptions of graphene-based trilayer systems considered.

6.2 Methods and Computational Details

In the present vdW-DFT approach, the exchange correlation functional form includes the non-local part of the dispersion correlation and is not a semi-empirical addition to the DFT Hamiltonian[47,114]. Briefly, the vdW energies arising from electron-electron correlation are incorporated into the total exchange-correlation energy as follows:

$$E_{xc}[n(\mathbf{r})] = E_x^{GGA}[n(\mathbf{r})] + E_C^{LDA}[n(\mathbf{r})] + E_C^{nl}[n(\mathbf{r})],$$ (6.1)

where the $E_x^{GGA}[n(\mathbf{r})]$ is the exchange energy described through the semi-local generalized gradient approximation (GGA), $E_C^{LDA}[n(\mathbf{r})]$ is the local part of correlation energy described in the local density approximation (LDA) and $E_c^{nl}[n(\mathbf{r})]$ is the non-local part of correlation energy given by

$$E_c^{nl}[n(\mathbf{r})] = \frac{1}{2} \iint d^3\mathbf{r}_1 d^3\mathbf{r}_2 n(\mathbf{r}_1) n(\mathbf{r}_2) \phi(q_1, q_2, r_{12}),$$ (6.2)

where $r_{12} = |\mathbf{r}_1 - \mathbf{r}_2|$, and q_1, q_2 are the values of a universal function $q_0[n(\mathbf{r}), |\nabla n(\mathbf{r})|]$, evaluated at $\mathbf{r}_1$ and $\mathbf{r}_2$. The kernel also has a universal form satisfying (i) E_c^{nl} is strictly zero for any system with constant density; and (ii) the interaction between any two molecules has the correct r^{-6} dependence for large separations r[46,47]. It is to be noted that the vdW functional form implemented in the SIESTA program package has been

successfully applied to systems such as pairs of atoms and molecules, molecules adsorbed on surfaces, molecular solids, and biological systems[136]. For example, in a semiconducting crystal consisting of carbon nanotubes (CNTs), the vdw-DFT approach predicts the wall-to-wall separation to be 3.45 Å, in excellent agreement with corresponding experiment value of 3.4 Å[137].

Norm-conserving pseudopotentials[115] and double-zeta basis sets with polarization orbitals were used for all atoms in electronic structure calculations. A vacuum distance of 15 Å between 2D system images was used. All calculated equilibrium configurations were fully relaxed, with residual forces smaller than 0.01 eV/Å. The reciprocal space integration to optimize the geometrical configuration was initially performed with a grid of $30 \times 30 \times 1$ k-points. Total energy, band structure and density of states of the optimized configurations were then calculated with a grid of $100 \times 100 \times 1$ k-points.

Our trilayers represent commensurate in-plane structures which are analogous to the so-called strained-layer semiconducting superlattices. The lattice constant along the direction perpendicular to the graphene plane is taken to be 30 Å, and the common lattice constant of the sandwich structure is fully optimized yielding a marginally small isotropic strain in both graphene and BN. Note that the difference in the lattice constants of the graphene and BN is about 1.6%, and graphene is always gapless under isotropic strain[112]. This is not the case with uniaxial strain where one needs to be careful in the determination of points of high symmetry in the reciprocal space since the position of the point K in the high symmetry of the graphene Brillouin zone is misplaced[138,139].

The zero-bias conductance, bias-dependent electron transmission and current are calculated using the non-equilibrium Green's functional (NEGF) method based on the Keldysh formalism, see Chapter 3 for the details.

For the contact Au atoms used in the transport calculations, the chosen Au pseudopotential and basis sets representing 5d and 6s valence electrons reproduced the electronic properties of the bulk Au near the Fermi region and have been successfully applied to investigate electronic transport properties of Au-C_{60}-Au[1] and Au-graphene-Au systems[3]. A grid of the 16x16 k-points perpendicular to the transport direction was used.

The distance between gold and the nearest monolayer is taken to be 2.1 Å, though the equilibrium binding distance of graphene[140-142] and BN[143] on Au(111) are reported to be about 3.5 and 3.0 Å, respectively. In our test calculations where we increase the distance between the contact Au and graphene (BN) to 3.5 Å, both transmission and the I-V characteristics are found to be very similar to those calculated at the distance of 2.1 Å, though the former case yielded a moderately smaller magnitude of the current at a given applied bias voltage.

6.3 Results and Discussion

For the geometry and electronic structure calculations, we used van der Waals (vdW) corrected density functional theory (DFT) method implemented in the SIESTA electronic structure program package[47,114]. In previous studies[2,3,94,144], the local density approximation (LDA)-DFT method has been found to be satisfactory in reproducing interlayer spacings in graphitic systems. However, LDA tends to underestimate the interlayer binding energies[118] compared with experiments[145,146] due to its localized nature. The inclusion of a vdW term representing dispersive forces in the electronic Hamiltonian becomes essential in obtaining accurate predictions in geometry and in particular energetics for graphene-based materials[24,141,147-150]. For example, the calculated binding energy per atom for graphite is 17 meV at the LDA-DFT level of theory, while inclusion of the vdW term yields a binding energy per atom of 45 meV, in excellent agreement with experiment[145,146]. When graphene is deposited on top of a BN substrate, the interface bonding is exclusively due to long-range van der Waals forces[24]. The vdW-DFT method has also been found to provide accurate descriptions of geometrical and electronic structures, band energy, and electron tunneling between metallic surfaces, including graphene[141,147-149]. If vdW corrections are not included, significant overestimation of the structural corrugation in the observed Moiré pattern is found[147].

6.3.1 Structural Properties

 A trilayer consisting of graphene and BN has more stacking possibilities than those in a graphene/BN bilayer, since each adjacent bilayer can be stacked in three distinct

arrangements[2]. Here we restrict ourselves to investigate only three trilayer stacking arrangements, namely AAA (hexagonal), ABA (Bernal) and ABC (rhombohedral), which may be considered as the most typical configurations[135]. The ABA stacked trilayer is taken to be composed of the AB (boron) bilayer configuration which was predicted to be the most stable stacking arrangement for a graphene/BN bilayer at the vdW-DFT level of theory[151]. In the AB (boron) bilayer configuration, the boron sublattice of one layer is on top of one carbon sublattice of the other layer, while the nitrogen sublattice is on top of the center of one hexagonal carbon ring[2]. The vdW-DFT interlayer spacing for AB (boron) configuration of the graphene/BN bilayer found by us is 3.32 Å and is in agreement with the value of 3.35 Å obtained from calculations using the random-phase approximation to the correlation energy[24].

Figure 6.1 shows the stacking arrangements considered for the graphene/BN/graphene trilayer. In the AAA stacking (Figure 6.1 (a)), all three constituent layers project themselves to the same image on a plane parallel to them, i.e., each adjacent layer pair is AA stacked. In the ABA stacking (Figure 6.1 (b)), the two graphene layers have the same projection on this plane and the BN layer is AB (boron) stacked to both graphene layers.
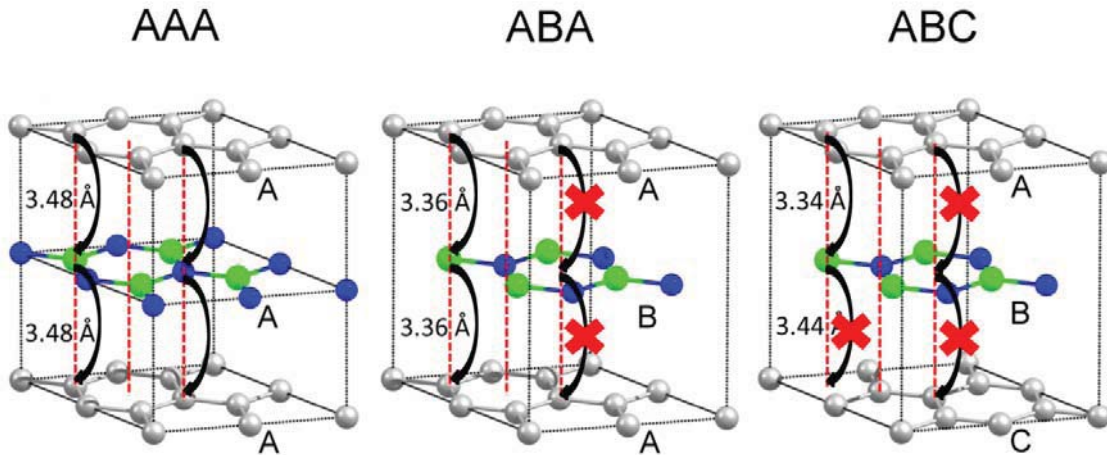

Figure 6.1 A schematic diagram of the stacking arrangements considered for graphene/BN/graphene. The AAA, ABA and ABC stackings are represented in (a), (b) and (c), respectively. The gray, green, and blue spheres represent carbon, boron, and nitrogen atoms, respectively. The black curved arrows show the possible atomic coupling between adjacent layers, while the red crosses show the couplings which in practice are not available.

Finally, the ABC stacking (Figure 6.1 (c)) represents the case where all three layers have different projections on this plane. While the BN layer is AB (boron) stacked to the upper graphene layer, it is AB (nitrogen) stacked to the lower graphene layer.

Table 6.1 gives the calculated values of binding energy, intraplanar bond length (R), intraplanar lattice constant (a) and interplanar spacing (Z) for various graphene/BN/graphene and BN/graphene/BN trilayer stacking configurations. In the present calculation all three layers in one trilayer system are in the same modeling box, yielding the same lattice constant for all layers. The binding energy is defined as the difference in total energy of an assembled trilayer system and that of the corresponding individual total energies of the isolated constituent monolayers, and is normalized to the formula unit.

The ABA stacking arrangement for graphene/BN/graphene is predicted to be the most stable configuration with R of 1.451 Å and Z of 3.36 Å. Note that the calculated R of graphene and a BN monolayer are 1.448 and 1.459 Å, respectively.

Table 6.1 Structural properties of graphene/BN/graphene and BN/graphene/BN at the vdW-DFT level of theory.

System	Stacking configuration	Binding energy/ formula unit (eV)	(intraplanar) bond length R (Å)	interplanar spacing Z (Å)
graphene/BN/graphene	AAA	0.254	1.451	3.48
graphene/BN/graphene	ABA	0.289	1.451	3.36
graphene/BN/graphene	ABC	0.283	1.451	3.34, 3.44
BN/graphene/BN	AAA	0.241	1.454	3.52
BN/graphene/BN	ABA	0.273	1.455	3.37
BN/graphene/BN	ABC	0.274	1.455	3.38, 3.38

The calculated R of graphene/BN/graphene is a weighted mean of the bond lengths of the constituent layers, and is independent of the stacking arrangements (Table 6.1).

On the other hand, the calculated Z of graphene/BN/graphene (~3.36 Å) gets modified slightly relative to that in the constituent bilayers (~3.32 Å). Z also depends on the stacking arrangements following the order of $Z_{AAA} > Z_{ABC} > Z_{ABA}$ which is directly related to the order of $Z_{AA} > Z_{AB\ (nitrogen)} > Z_{AB\ (boron)}$ calculated for graphene/BN bilayer at the vdW-DFT level of theory[151]. Comparison of our results with the ABA-stacked trilayer graphene suggests that the substitution of a central graphene with a BN monolayer modifies Z from 3.415 to 3.36 Å at the vdW-DFT level of theory. Note that previously reported results on the trilayer graphene find the interplanar separation to be 3.33 Å at the LDA-DFT level of theory[152]. Thus, a larger interplanar spacing for the AAA stacking is associated with a smaller binding energy; while the ABA stacking has a smaller (averaged) interplanar spacing associated with the higher binding energy for graphene/BN/graphene.

Figure 6.2 shows the stacking arrangements considered for BN/graphene/BN. The ABA and ABC stacked configurations are predicted to be nearly degenerate (Table 6.1) at the vdW-DFT level of theory.
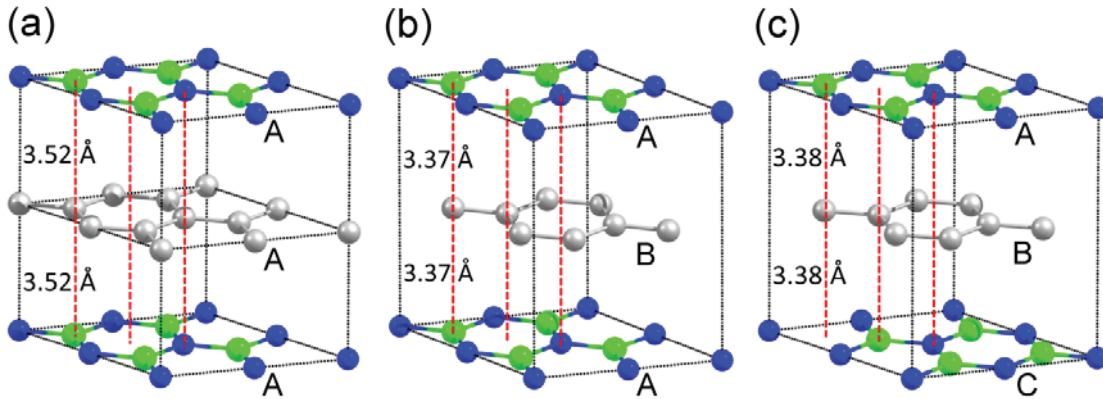

Figure 6.2 A schematic diagram of the stacking arrangements considered for BN/graphene/BN. The AAA, ABA and ABC stackings are represented in (a), (b) and (c), respectively. The gray, green, and blue spheres represent carbon, boron, and nitrogen atoms, respectively.

The calculated R and Z for BN/graphene/BN also follow their respective values in the constituent bilayers. For example, R is independent of the stacking arrangements, and is about the weighted mean of constituent monolayers. The ABA and ABC stacked configurations are both composed of two AB (boron) bilayers with the same interplanar spacing of 3.37 Å (Table 6.1), whereas Z of the AAA-stacked BN/graphene/BN trilayer is calculated to be 3.52 Å.

6.3.2 Electronic Properties

The electronic band structure along the high symmetry points in k-space of the energetically preferred ABA-stacked configurations of graphene/BN/graphene and BN/graphene/BN are plotted in Figure 6.3. We note that the band structure of the graphene/BN bilayer near the Fermi energy is dominated by $C-p_z$ orbitals. The calculated energy gap at K is 43 meV at the vdW-DFT level of theory which is mainly due to the interaction of graphene with the BN monolayer where two sublattices in graphene experience a slightly different electrostatic potential due to inhomogeneous charge distribution present in the heterogeneous BN monolayer[2].

In the ABA-stacked graphene/BN/graphene trilayer, the graphene layers are structurally symmetric. Although the interaction between top and bottom graphene layers with the central BN monolayer lifts the degeneracy of bands associated with graphene near the Fermi energy (Figure 6.3 (b)), it is not sufficiently strong to open the gap at K. No shift of the Dirac point away from the high symmetry K point in the reciprocal space is predicted. The calculated band gap remains nearly zero (≈1 meV) for the ABA-stacked graphene/BN/graphene. This is also the case with the AAA and ABC-stacked trilayers where the gap is calculated to be 4 and 6 meV, respectively. It therefore appears that the central BN layer has a much weaker impact on both top and bottom graphene in the trilayer configuration as compared to the case of graphene/BN bilayer. Note that trilayer graphene in AAA, ABA, and ABC-stacked configurations all have a zero gap at the vdW-DFT level of theory[151].
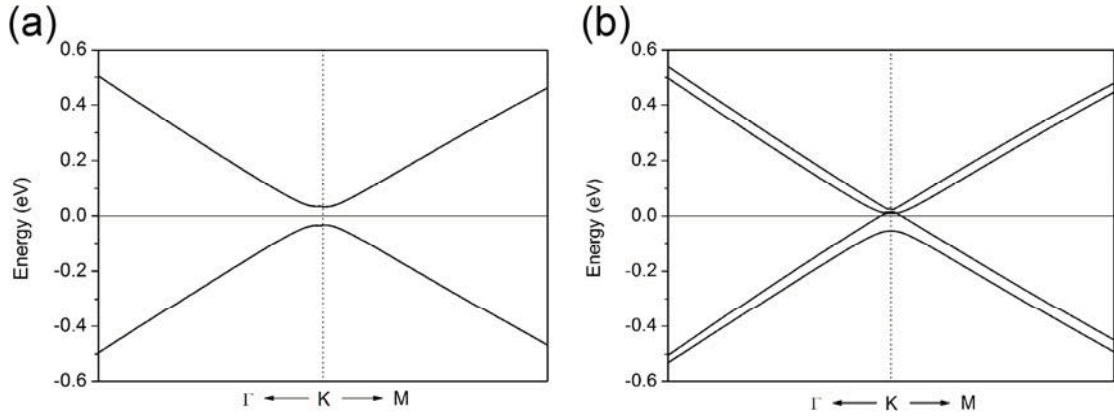
Figure 6.3 The calculated band structures of (a) ABA-stacked BN/graphene/BN and (b) ABA-stacked graphene/BN/graphene. Zero of the energy is aligned to the Fermi level.

For the case of BN/graphene/BN trilayer, the band gap appears to be relatively more sensitive to the stacking arrangements. The band gap for AAA, ABA and ABC stacking arrangements are calculated to be 116, 57 and 5 meV, respectively at the vdW-DFT level of theory. The difference in band gap values can be understood by a straightforward analysis. In AAA stacking, while one carbon sublattice is coupled with boron sublattices in both BN layers, the other carbon sublattice is coupled with nitrogen sublattices. The high asymmetry in electronegativity between boron and nitrogen sublattices induces a significant corresponding asymmetry in the two carbon sublattices of the central graphene layer. In ABA stacking, while one carbon sublattice (sublattice I) is coupled with two boron sublattices, the other carbon sublattice (sublattice II) is in between the centers of BN hexagonal rings (Figure 6.2 (c)). Compared with AAA stacking, in ABA stacking the asymmetry in two carbon sublattices induced by the difference between boron and nitrogen is lower because carbon sublattice II is relatively far from both boron and nitrogen. On the other hand, top and bottom BN layers in the ABC-stacked configuration do not induce an asymmetry between two carbon sublattices of the central layer (Figure 6.2 (c)), leading to a tiny band gap of 5 meV, as also predicted by previous calculations[20]. As a consequence, AAA shows the highest energy gap, followed by ABA, while ABC stacking exhibits a virtually negligible gap.

6.3.3 Effect of Electric Field on Band Structure.

Figure 6.4 shows a variation of the minimum energy gap under the influence of the electric field applied perpendicular to the layered configurations. The direction of applied field is from bottom layer to top layer, and we restrict ourselves to electric field strengths below 1 V/nm, considering that the breakdown field of BN sheets is reported to be 0.7 V/nm[22]. It is to be noted here that the AAA and ABA stacked graphene/BN/graphene (BN/graphene/BN) configurations exhibit mirror symmetry about the central layer, and the ABC stacked BN/graphene/BN trilayer exhibits the point symmetry about the midpoint of two (left most) two carbon atoms shown in Figure 6.2 (c). Thus, no changes in the electronic properties are expected when the direction of electric field is reversed for these trilayers. On the other hand, the ABC stacked graphene/BN/graphene trilayer has neither mirror symmetry nor point symmetry. However, reversal of the electric field is expected to have a minimal effect due a lack of effective interaction between top and bottom graphene layers, as will be shown below.
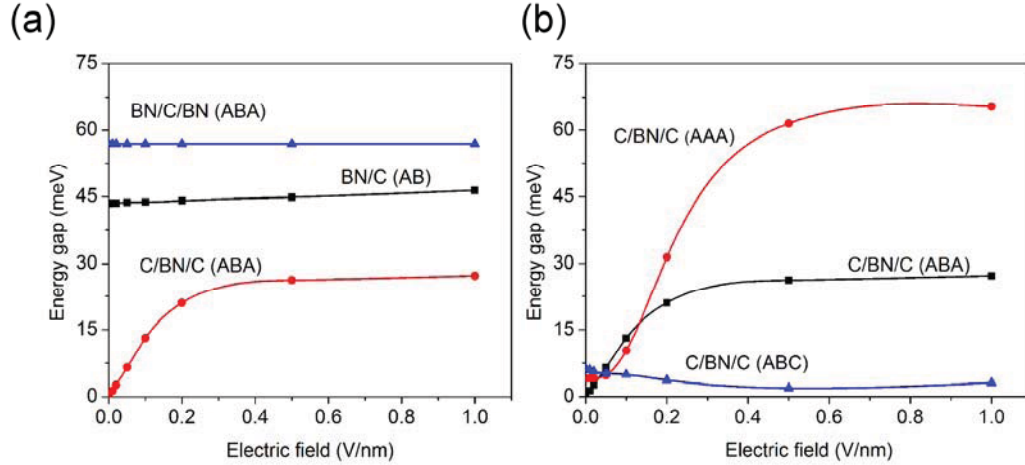
Figure 6.4 The minimum energy gap as a function of perpendicular electric field: (a) ABA-stacked BN/graphene/BN, ABA-stacked graphene/BN/graphene and AB-stacked BN/graphene, (b) AAA-, ABA- and ABC-stacked graphene/BN/graphene.

A distinct behavior in electronic properties is exhibited by the graphene/BN/graphene and BN/graphene/BN trilayers in the presence of the perpendicular external field; the former configuration shows a significant modulation of band gap whereas the latter

configuration does not show any modulation in its band gap (Figure 6.4 (a)). This difference is consistent with the previously reported LDA-DFT calculations[20].

For the ABA-stacked BN/graphene/BN trilayer, we find an invariable band gap of 57 meV with the applied electric field up to 1 V/nm. On the other hand, the ABA-stacked graphene/BN/graphene trilayer shows gap tunability with the applied electric field up to 0.5 V/nm, where the gap saturates at about 27 meV, showing virtually no further changes with increasing electric field up to 1 V/nm. Thus, graphene/BN/graphene behaves more like a graphene bilayer, but with a weaker and indirect (via BN layer) graphene-graphene interaction and a less tunable band gap. In a separate calculation on graphene bilayer, we found a nearly linear relationship between the energy gap and the magnitude of an external electric field ranging from 0 to 1 V/nm, in excellent agreement with experimental results[153]. Also, our vdW-DFT results for graphene/BN bilayer are in agreement with the previous theoretical study showing a much weaker, but linear response of the energy gap to the external electric field[19].

As shown in Figure 6.4 (b), the stacking arrangements in the graphene/BN/graphene trilayer appear to play a major role on the field tunability of the band gap. Both AAA and ABA stacking configurations show significant gap variation with the applied electric field, whereas the ABC stacked configuration shows little change (even a small reduction) in the energy gap with increasing applied perpendicular electric field (Figure 6.4 (b)). This is in sharp contrast to that the behavior found in a graphene trilayer, where ABC stacking configuration exhibits a larger band gap modulation than the AAA or ABA stacking configurations[132].

A band gap in the hybrid graphene/BN bilayer in the presence of an external field applied perpendicularly is attributed to the different electrostatic potential experienced by the carbon sublattices in graphene due to the inhomogeneous charge distribution present in BN[2,19]. Thus, the stacking sequence which would facilitate a larger interlayer coupling to introduce high asymmetry in the sublattices of graphene is likely to lead to a significant energy dispersion of electronic bands near the Fermi surface.
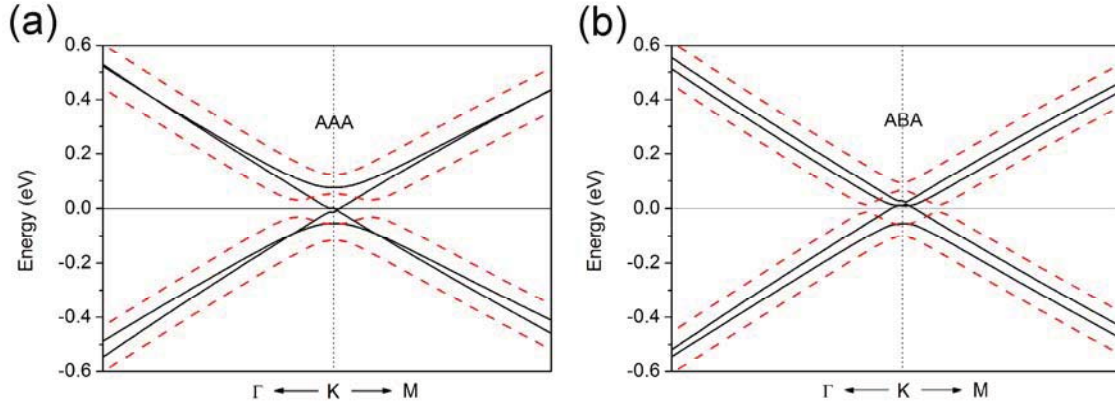
Figure 6.5 Electronic band structures of (a) AAA- and (b) ABA-stacked graphene/BN/graphene trilayers. Solid black: field=0. Dashed red: field=0.5 V/nm. Zero of the energy is aligned to the Fermi level.

For graphene/BN/graphene, topology of the AAA stacking provides a significant interlayer bonding, since all carbon atoms in graphene and all boron and nitrogen atoms in BN are placed at the same in-plane atomic positions (i.e., on top of each other). This facilitates a relatively strong coupling between top and bottom graphene layers (Figure 6.1). In ABA stacking, only half of the carbon atoms interact significantly, resulting in a weaker coupling between graphene layers compared with AAA. In ABC stacking, no carbon atoms of the top graphene can interact with the bottom layer via BN, so the coupling in this configuration is weakest. Note that the 'Mexican hat' pattern in band structures shown in Figure 6.5 is the signature of biased coupled graphene bilayer, where the magnitude of the minimal energy gap reflects the coupling strength between two graphene layers. Thus we argue that AAA and ABA stacked graphene/BN/graphene trilayers just behave like graphene bilayers but with weaker coupling, while ABC stacked graphene/BN/graphene trilayer behaves like two uncoupled graphene monolayers when an electric field is applied. For the case of trilayer graphene, on the other hand, it has been argued that the loss of mirror symmetry in the ABC-stacked trilayer introduces asymmetry in the sublattices, which is enhanced by the external electric field compared to the cases of AAA- or ABA-stacked configurations[142,154].

6.3.4 Electronic Transport Properties

The contact leads for transport calculations are composed of semi-infinite Au-(111) surfaces which comprised of 6 (top) and 7 (bottom) atomic layers. For trilayers, the distance between gold and the nearest monolayer is taken to be 2.1 Å, while the distance between the left and the right gold electrodes is 11 Å. The Mulliken population analysis suggests that no charge transfer takes place between Au atoms and graphene or BN monolayers, though a relatively strong interaction exists between gold and the monolayers in this device configuration. For example, the average valence charge of carbon atoms in the gold-(ABA) graphene/BN/graphene-gold configuration is 4.0045 e⁻.
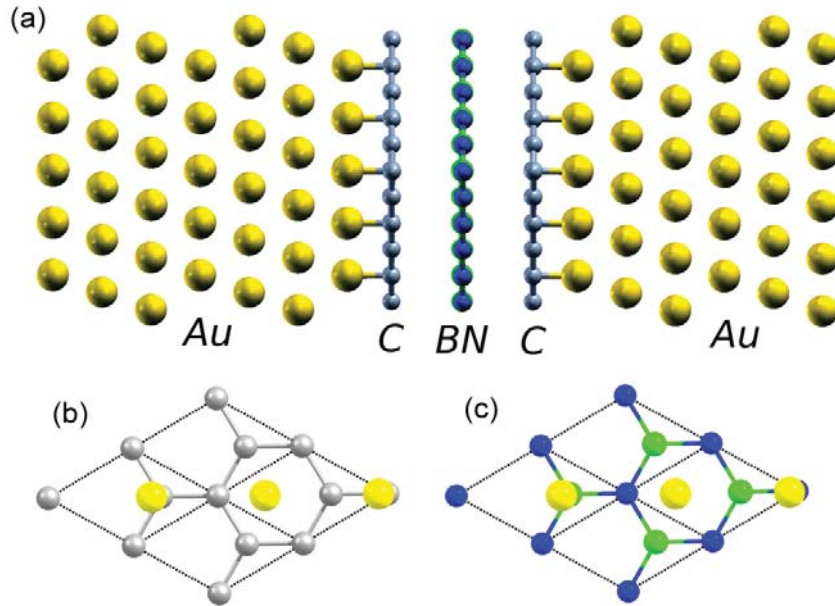
Figure 6.6 (a) A side view of the ABA stacked graphene/BN/graphene trilayer coupled with semi-infinite bulk gold contacts. (b) Contact detail between gold and graphene in panel (a). (c) Contact detail between gold and BN in a BN/graphene/BN transport calculation. Symbols: C in grey, B in green, N in blue and Au in yellow.

Note that the lattice mismatch between the Au-(111) surface and graphene is about 1.5%. Such a device configuration (Figure 6.6) has been commonly used in previous theoretical studies investigating interactions between graphene and metallic systems[140,142,149]. The calculated *I-V* characteristics of the ABA-stacked trilayers for the perpendicular applied

bias are shown in Figure 6.7. The results show a nearly metal-like conduction for both graphene/BN/graphene and BN/graphene/BN in the low-field regime.

This is consistent with zero-field transmission functions of these configurations as shown in Figure 6.8 (a).

It is clear from the figure that both graphene/BN/graphene and BN/graphene/BN trilayers have a non-negligible transmission at the Fermi energy. With increase in the bias voltage, both graphene/BN/graphene and BN/graphene/BN trilayers exhibit a low-gap, p-type semiconducting behavior. Interestingly, the zero-field gap-opening in BN/graphene/BN does not appear to suppress the current. In fact, the magnitude of the calculated current is even slightly higher than that in the case of graphene/BN/graphene at a given applied bias voltage.
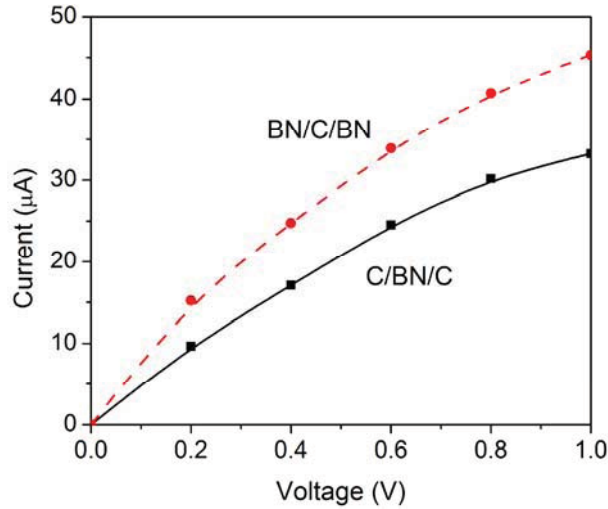
Figure 6.7 I-V characteristics of the ABA-stacked graphene/BN/graphene and ABA-stacked BN/graphene/BN trilayers coupled with gold contacts (see, Figure 6.6).

We attribute this to the difference in the effect of the external electric field on the band gap of the two systems – a nearly field-independent band gap of the BN/graphene/BN trilayer versus a variable band gap of the graphene/BN/graphene system. Additionally, the difference in the nature of chemical bonding at the Au-graphene and Au/BN interfaces, as shown in Figure 6.9, also contributes to a higher current in the Au-BN/graphene/BN-Au system than in the Au-graphene/BN/graphene-Au.

76

There exists a relatively strong bonding between gold and boron/nitrogen atoms of BN relative to gold and carbon atoms (Figure 6.9) which provides additional conduction channels for BN/graphene/BN.
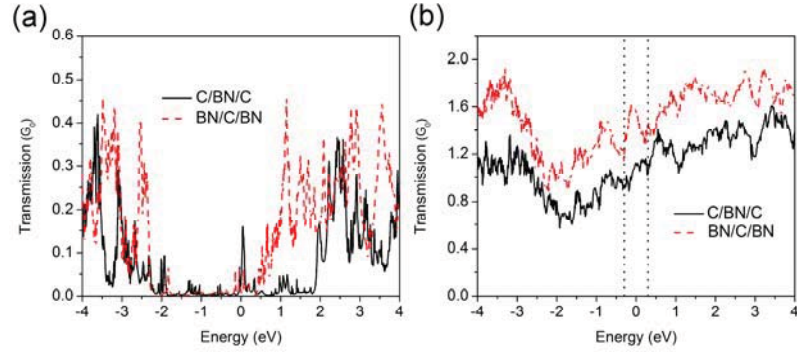

Figure 6.8 Transmission function as a function of energy of ABA-stacked graphene/BN/graphene and ABA-stacked BN/graphene/BN trilayers: (a)bias =0 (b)bias =0.6 V. Zero of the energy is aligned to the Fermi level.

This is confirmed by the presence of additional conduction band-derived states in the finite field transmission function of BN/graphene/BN shown in Figure 6.8 considering that the transmission function, in general, reflects the intrinsic transmission characteristics of the trilayer system. 6.4 Summary

Electronic structure calculations at the level of vdW-DFT theory together with non-equilibrium Green's Function method were performed on mixed trilayers composed of graphene and BN. These trilayers exhibit strong stacking dependence on the inter-layer interactions and the electronic band structure. The binding energy for the graphene/BN/graphene system shows the order ABA>ABC>AAA whereas the order is ABC~ABA>AAA for BN/graphene/BN trilayer. In both cases, AAA stacking yields significantly lower binding energies than that for ABA or ABC stacking.
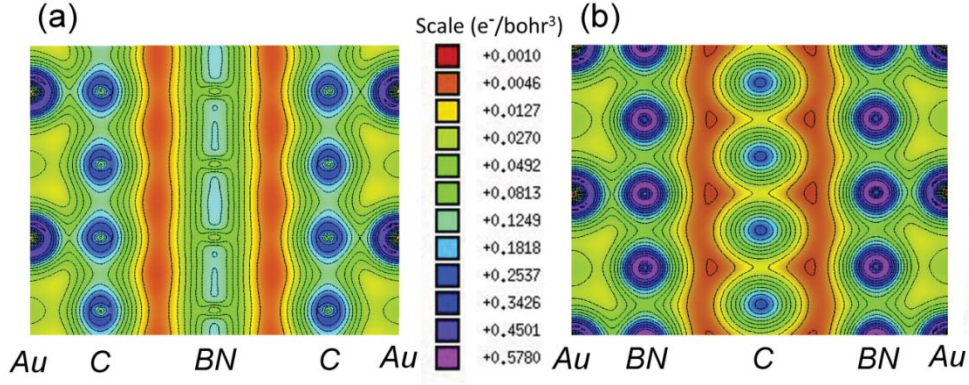
Figure 6.9 The valence charge density contours of (a) ABA-stacked graphene/BN/graphene, and (b) ABA-stacked BN/graphene/BN trilayers coupled with gold contacts.

The graphene/BN/graphene trilayer shows almost zero (~ 1 meV) gap in the band structure at K point for ABA stacking and very small, 4 meV and 6 meV, gap for the AAA and ABC stacking configurations, respectively. The BN/graphene/BN trilayer, on the other hand, shows a finite band gap that depends on the stacking arrangement in the order: AAA>ABA>ABC.

The presence of an external electric field applied perpendicular to the planes of the trilayers shows remarkable differences in the tunability of the band gap of the two cases. Whereas the zero-field band gap in the case of BN/graphene/BN trilayer remains unaffected by the external field, the graphene/BN/graphene trilayer in its AAA and ABA stacking configurations exhibit spectacular tunability in the low field (i.e., below 0.5 V/nm) regime. The calculations reveal that in the low-field regime, both graphene/BN/graphene and BN/graphene/BN show a metal-like conduction that changes to a low-gap semiconductor, with p-type I-V characteristics. Since thicker layers of two-dimensional sheets of graphene, BN and their hybrid structures are more easily accessible in the experiments, both graphene/BN/graphene and BN/graphene/BN graphene trilayers can be useful for applications in nanoscale devices, as the present study shows.

Chapter 7　Interaction of Nucleobases with Silicon Nanowires[5]

7.1 Introduction

Silicon prefers the so-called sp^3 tetrahedral coordination in a lattice. Unsaturated dangling bonds on the surface of a silicon nanowire (SiNW) are highly reactive. As a consequence, SiNWs grown in experiments tend to be passivated [35]. The nature of the surface passivation is an important aspect in determining the properties of SiNWs, especially for those with smaller diameters. For example, hydrogen termination yields p-type characteristics of SiNWs [155] while phosphorus passivation is predicted to further increase the p-doping level in SiNWs [156]. In describing the interaction of a SiNW with an analyte molecule on its surface, as a SiNW would be used in a realizable sensor, the inclusion of a passivation layer is paramount.

In this chapter, we present the results of our first-principles study of a hydrogen passivated SiNW interacting with deoxyribonucleic acid (DNA) and ribonucleic acid (RNA). Since full scale quantum mechanical calculations consisting of DNA-strands are prohibitively expensive, we begin with the nucleobases, the building blocks of the genetic macromolecules (DNA/RNA) to discover factors that play an important role in these kinds of interactions. We will consider the interaction of a passivated SiNW with adenine (A), cytosine (C), guanine (G), thymine (T) and uracil (U). Since the interaction of nucleobases with graphene [157] and metallic carbon nanotubes (CNTs) [158] is predicted to be dominated by the so-called van der Waals (vdW) forces, our focus will be to identify the type of interaction for the case of SiNWs which are semiconducting in nature. It is expected that a complete understanding of the underlying physics and chemistry of the sensing mechanism of DNA would help in developing SiNW based biomolecular sensing devices.

7.2 Computational Method

---

[5] Chapter 7 is reprinted with permission from (Chemical Physics Letters, 553, 55 (2012)). Copyright (2012) Elsevier. See Appendix F for documentation of permission to republish this material.

The local density approximation (LDA) of the exchange and correlation functional forms within density functional theory, as incorporated in the SIESTA program package was used [56]. We make use of Troullier-Martins type pseudopotentials [115] and double-ζ basis sets with polarization functions for all atoms in our electronic structure calculations. A minimum vacuum distance of 15 Å between neighboring system images was used. The k-space integration was done with a 1x1x4 sampling grid. The calculated equilibrium configurations are fully relaxed, with residual forces smaller than 0.04 eV/Å.

7.3 Results and Discussion

7.3.1 Nucleobases

The total energy and optimized geometrical structure of the isolated nucleobases were found prior to the nucleobase-SiNW complex calculations. The bond lengths and bond angles of the optimized equilibrium structures for the nucleobases are in good agreement with earlier reported studies [159,160]. The calculated binding energy for each nucleobase at the LDA-DFT level of theory, defined as the total energy difference between the equilibrium configuration of the molecules and the isolated individual atoms, is 6.82, 6.76, 6.87, 6.83 and 6.76 eV for A, T, G, C, and U respectively.

7.3.2 Passivated Silicon Nanowires

In this study, a SiNW is constructed of [100] bulk silicon with a square cross section of dimension 14 Å (Figure 7.1). The surface dangling bonds are passivated with hydrogen [35]. Thus, all Si atoms are sp^3 coordinated as in bulk, with no dangling bonds on the surface of the SiNW. The resulting passivated SiNW is finite in the two dimensions of its cross-section, and infinite (periodic) in length.

In the optimized passivated SiNW, the bond distance between silicon and hydrogen atoms, R_{Si-H}, is 1.52 Å. At the core of the SiNW, the calculated silicon-silicon bond length, R_{Si-Si}, is 2.33 Å. The silicon-silicon bond is slightly shortened to 2.32 Å at the surface of the SiNW. The calculated bond lengths are in excellent agreement with the

results of the GGA-DFT level of theory where R_{Si-Si} (core) and R_{Si-Si} (surface) were calculated to be 2.36 and 2.35 Å, respectively [161].
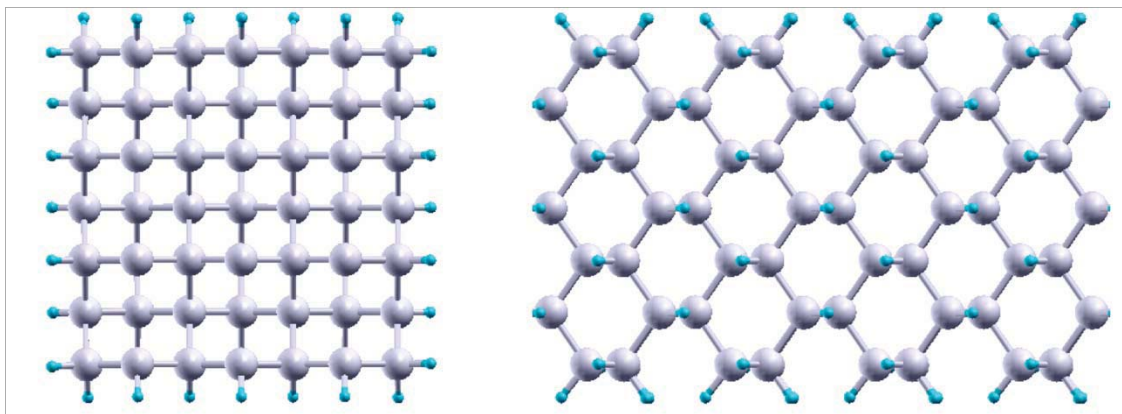

Figure 7.1 Hydrogen passivated SiNW. Silicon: grey (grey), hydrogen: light blue (grey). Left: cross-section view. Right: top view of surface of wire.

7.3.3. Nucleobases with SiNW

In the calculations aimed to obtain the equilibrium configurations, the nucleobases were allowed to approach one surface in a direction perpendicular to the axis of the tube. The plane of the hexagon/pentagon rings of the nucleobases is parallel to the surface of the SiNW. Unlike small diameter carbon nanotubes (CNTs) where the tube curvature has an effect on the binding energy [158], a SiNW has flat surfaces due to the passivating hydrogen atoms. In order to simulate an electronic environment resembling more closely the situation in DNA and RNA, the N atom of the base molecules linked to the sugar ring in a nucleic acid was terminated with a methyl group [157,158,162,163].

The equilibrium configurations (Figure 7.2) of the bioconjugated SiNW are obtained by a full optimization of the nucleobase-SiNW complex in which all atoms were free to relax. No significant changes in the bond lengths of the nucleobases are seen in the equilibrium configurations. Likewise, the surface bond lengths of the passivated SiNW remain nearly the same. Only a few passivating hydrogen atoms that are near an oxygen atom of the nucleobases experience perturbations (about 0.2 Å). The calculated distance between a nucleobase and SiNW is about 2.0-2.1 Å which is defined as the separation between the hexagonal ring-center of the molecule and the passivated surface.

81
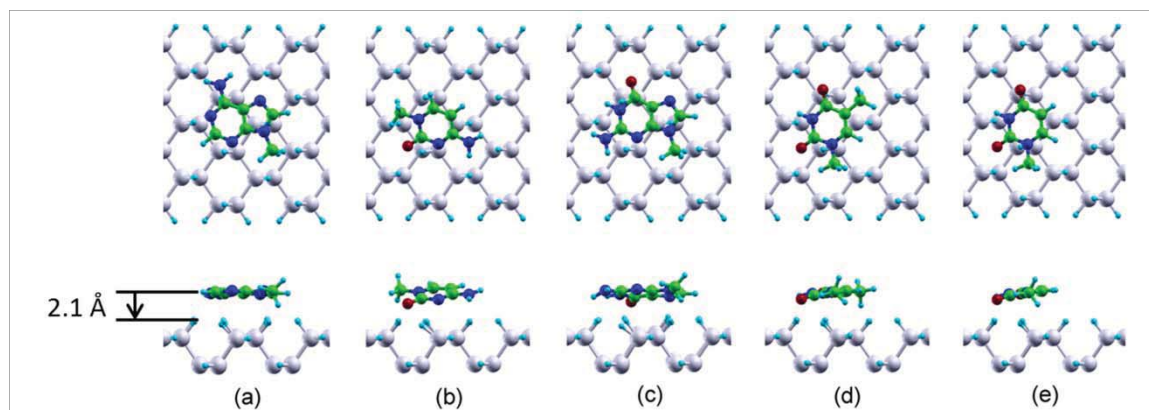
Figure 7.2 Top and side views of the equilibrium configurations of nucleobases interacting with a SiNW: (a) adenine, (b) cytosine, (c) guanine, (d) thymine and (e) uracil. Silicon: grey (grey), hydrogen: light blue (grey), nitrogen: dark blue (black), carbon: green (dark grey), oxygen: red (black).

Interestingly, the nucleobases show a slight tilt towards the underlying passivated surface with the estimated tilt angle being 2º, 17º, 12º, 5º, and 5º for A, C, G, T, and U, respectively in the equilibrium configurations. The tilt angle describes the orientation of the ring plane of the nucleobases and is defined as the angle between the base ring plane and the plane defined by frozen hydrogen atoms of the passivation surface layer of the SiNW. It appears that adenine which contains no oxygen atom yields a nearly parallel configuration to the surface. On the other hand, the presence of one or two oxygen atoms in other nucleobases can facilitate a weak O⋯H-Si interaction which seems to provide tilting of the nucleobases on the surface of SiNW. The nucleobases C and G are levered out-of-plane to a greater degree by their single oxygen atom, than are U and T which possess two distributed oxygen atoms that provide a level of counterbalance.

The interaction strength between a nucleobase and a SiNW can be characterized by the binding energy (E_b), defined as the total energy difference between the equilibrium configuration of the complex (Figure 7.2) and the isolated individual constituents (base molecules and SiNW). The calculated binding energy is 1.74, 1.72, 2.12, 1.64 and 1.53 eV for A, C, G, T and U, respectively. Thus, the guanine-SiNW complex exhibits a

slightly higher binding energy than the other four bases, which show a similar binding strength. This is somewhat similar to nucleobases interacting with a semiconducting boron nitride nanotube (BNNT) [162], but significantly different from the case of nucleobases interacting with a metallic carbon nanotube (CNT) which follows the order of G>A>T>C~U [158]. Since the E_b associated with CNTs was found to be correlated with the polarizability of individual bases, it was suggested that the interaction of nucleobases with CNTs was governed by a dispersion force like van der Waals which varies with the polarizability of the interacting entity [158]. For the case of BNNT, it was suggested that dispersive forces with a marginal contribution from electrostatic forces provide for the stability of the bioconjugated complex [162].

Since the passivated SiNW have sp^3-like bonding, we do not expect the van der Waals like dispersive interactions to play any role in the stabilization of the bioconjugated complex consisting of the passivated SiNW. Instead, a noticeable degree of charge transfer from the nucleobase to the passivated SiNW suggests the interaction to be dominated by electrostatic forces. Mulliken population analysis indicates the transfer of 0.3, 0.3, 0.4, 0.2 and 0.2 electrons from A, C, G, T and U, respectively to the passivated SiNW. On the other hand, charger transfer between a nucleobase and a CNT or a BNNT is much less significant [158,162]. The amount of charge transferred from a nucleobase to the SiNW also agrees with the rank order of the binding energy calculated for the complex. This is consistent with the results of a previous investigation which used classical molecular dynamics simulations on the nucleobases interacting with a Si (111) surface functionalized with alkyl-amine molecules. It was suggested that the interactions involving the ring hydrogen bond donors and acceptors of the nucleobases mainly provide the stability of the bioconjugated complexes [163,164].

Figure 7.3 shows the calculated density of states (DOS) for the passivated SiNW which suggests it is semiconducting with a band gap of about 0.82 eV. The projected density of states finds both the valence band maximum and conduction band minimum to be associated with the Si atoms, thus reflecting the electronic structure of core of the SiNW [165].

For the cases of the conjugated SiNWs, there appears to be no change in the band gap values; the calculated gap is 0.80, 0.80, 0.79, 0.81 and 0.81 eV for A, C, G, T and U - conjugated SiNWs. As shown in Figure 7.3 the electronic states at the valence band maximum and conduction band minimum remain associated with the Si atoms of the wire of the nucleobase-SiNW complex. For each complex, the electronic states contributed by the nucleobase fall outside the gap; i.e., below the valence band maximum or above the conduction band minimum. This is in contrast to the case of nucleobase interactions with a semiconducting BNNT where a mid-gap state appears representing a mixing of electronic states of the nucleobases and the BNNT [162]. In the case of BNNT, boron and nitrogen atoms are exposed to the external environment without any passivation, facilitating a direct hybridization of states between boron/nitrogen and nucleobases. In the present work, the silicon atoms are protected by the hydrogen passivation, leading to a much weaker interaction between nucleobases and silicon atoms. Thus, the interaction between the nucleobases and the passivated SiNW does not modify the semiconducting nature of SiNWs.

7.4 Summary

The interaction of the nucleobases with a hydrogen passivated SiNW was investigated using a first principles method based on density functional theory. The equilibrium configurations of the nucleobase-SiNW complexes have the nucleobases lying with their ring planes nearly parallel to the surface of the nanowire. The tilt of the C, G, T, and U nucleobases exhibits a weak O···H-Si interaction.

Except for G, the base molecules exhibit almost similar interaction strengths with a SiNW. The magnitude of the calculated binding energy exhibits the following order: G>A≈C≈T≈U. Charge transfer by each nucleobase in forming a nucleobase-SiNW complex also follows this trend. An examination of the density of states for a passivated SiNW and the nucleobase-SiNW complexes shows semiconducting behavior and that the band gap remains defined by states contributed by the Si atoms of the nanowire.
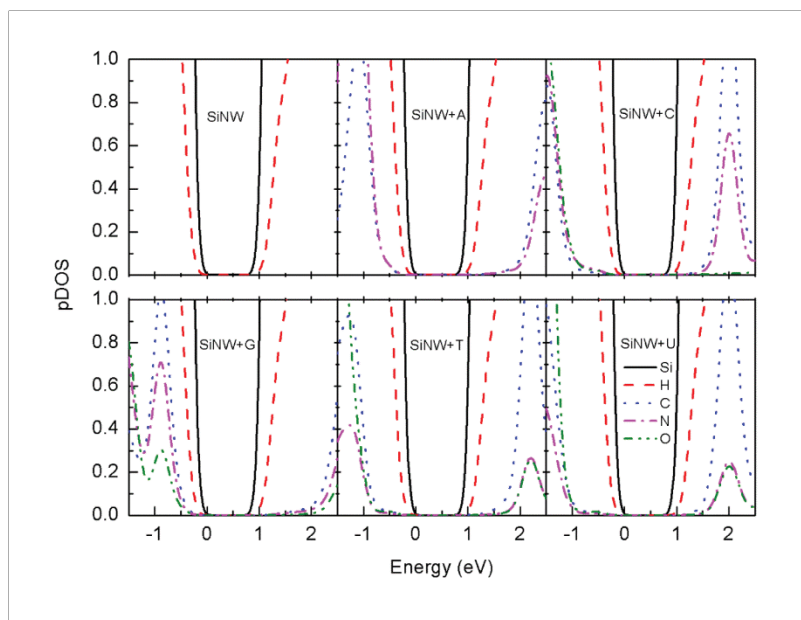
Figure 7.3 The calculated species-resolved projected density of states (pDOS) of pristine and conjugated SiNWs.

No mid-gap states are created in forming the complexes. The calculated band gap of the passivated SiNW is essentially unchanged in the interaction. As such, the nature of bonding between a nucleobase and a hydrogen passivated SiNW is dominated by electrostatic interactions with the band gap of the complex defined by the passivated SiNW.

Appendix A

List of Related Publications

☺Applicability of CNTs and BNNTs as Biosensors: Effect of Molecular Adsorption on the Transport Properties of Boron Nitride Nanotubes and Carbon Nanotubes

Zhong X., Mukhopadhyay S., Pandey R., Karna SP.

(accepted by Applied Physics Letters)

☺A Theoretical Study of Semiconducting Nanomembranes, BN, AlN and GaN: Structural, Mechanical, Electronic Properties and Strain- and Field-induced Band Gap Modulation

Amorim RG., Zhong X., Mukhopadhyay S., Pandey R., Rocha AR., Karna SP.

(accepted by Journal of Physics: Condensed Matter)

☺Interaction of Nucleobases with Silicon Nanowires: A First-principles Study

Zhong X., Slough WJ., Pandey R., Friedrich C.

Chemical Physics Letters, 553, 55 (2012)

☺Electronic Structure and Quantum Transport Properties of Trilayers Formed from Graphene and Boron Nitride

Zhong X., Amorim RG., Scheicher R., Pandey R., Karna SP.

Nanoscale, 4, 5490 (2012)

☺Stacking Dependent Electronic Structure and Transport in Bilayer Graphene Nanoribbons

Zhong X., Pandey R., Karna SP.

Carbon, 50, 784 (2012)

☺ Effect of Electric Field on the Band Structure of Graphene/Boron Nitride and Boron Nitride/Boron Nitride Bilayers

Balu R., Zhong X., Pandey R., Karna SP.

Applied Physics Letters, 100, 052104 (2012)

☺ First-principles Study of Strain-induced Modulation of Energy Gaps of Graphene/BN and BN Bilayers

Zhong X., Yap YK., Pandey R., Karna SP.

Physical Review B, 83, 193403 (2011)

☺ Anisotropy and Transport Properties of Tubular C-BN Janus Nanostructures

Wu MM., Zhong X., Wang Q., Sun Q., Pandey R., Jena P.

The Journal of Physical Chemistry C, 115, 23978 (2011)

☺ Can Single-atom Change Affect Electron Transport Properties of Molecular Nanostructures such as C_{60} Fullerene?

Zhong X., Pandey R., Rocha AR., Karna SP.

Appendix B

Scaling of Siesta Code

The calculation efficiency of the Siesta code installed on the group cluster 'Rama' (http://rama.phy.mtu.edu/, built with Rocks Cluster Distribution 5.4.2 (with CentOS 5.5)) has been evaluated. Figure A.1 represents the calculation time versus number of atoms using the Siesta code ((3x3) carbon nanotube, 1 processor).
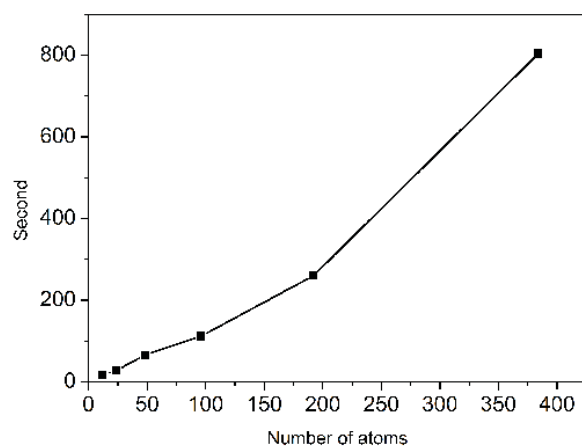
Figure A.1 Calculation time versus number of atoms.

Appendix C

Copyrights (This letter is for Chapter 3)

Appendix D

Copyrights (This letter is for Chapter 4)

Title: Stacking dependent electronic structure and transport in bilayer graphene nanoribbons

Author: Xiaoliang Zhong,Ravindra Pandey,Shashi P. Karna

Publication: Carbon

Publisher: Elsevier

Date: March 2012

Copyright © 2012, Elsevier

Logged in as:
Xiaoliang Zhong
Account #:
3000583356

Order Completed

Thank you very much for your order.

This is a License Agreement between Xiaoliang Zhong ("You") and Elsevier ("Elsevier"). The license consists of your order details, the terms and conditions provided by Elsevier, and the payment terms and conditions.

Get the printable license.

License Number	3121430363852
License date	Apr 03, 2013
Licensed content publisher	Elsevier
Licensed content publication	Carbon
Licensed content title	Stacking dependent electronic structure and transport in bilayer graphene nanoribbons
Licensed content author	Xiaoliang Zhong,Ravindra Pandey,Shashi P. Karna
Licensed content date	March 2012
Licensed content volume number	50
Licensed content issue number	3
Number of pages	7
Type of Use	reuse in a thesis/dissertation
Portion	full article
Format	both print and electronic
Are you the author of this Elsevier article?	Yes
Will you be translating?	No
Order reference number	
Title of your thesis/dissertation	ELECTRON TRANSPORT IN LOW-DIMENSIONAL NANOSTRUCTURES – THEORETICAL STUDY WITH APPLICATION

Appendix E

Copyrights (This letter is for Chapter 6)

Appendix F

Copyrights (This letter is for Chapter 7)

Bibliography

(1)   Zhong, X.; Pandey, R.; Rocha, A. R.; Karna, S. P. *The Journal of Physical Chemistry Letters* **2010**, *1*, 1584.

(2)   Zhong, X.; Yap, Y. K.; Pandey, R.; Karna, S. P. *Physical Review B* **2011**, *83*, 193403.

(3)   Zhong, X.; Pandey, R.; Karna, S. P. *Carbon* **2012**, *50*, 784.

(4)   Zhong, X.; Amorim, R. G.; Scheicher, R. H.; Pandey, R.; Karna, S. P. *Nanoscale* **2012**, *4*, 5490.

(5)   Zhong, X.; Slough, W. J.; Pandey, R.; Friedrich, C. *Chemical Physics Letters* **2012**, *553*, 55.

(6)   Castro Neto, A. H.; Guinea, F.; Peres, N. M. R.; Novoselov, K. S.; Geim, A. K. *Reviews of Modern Physics* **2009**, *81*, 109.

(7)   Geim, A. K.; Novoselov, K. S. *Nat Mater* **2007**, *6*, 183.

(8)   Katsnelson, M. I. *Materials Today* **2007**, *10*, 20.

(9)   Bourzac, K. *Nature* **2012**, *483*, S34.

(10)   Abergel, D. S. L.; Apalkov, V.; Berashevich, J.; Ziegler, K.; Chakraborty, T. *Advances in Physics* **2010**, *59*, 261

(11)   Kunstmann, J.; Ouml; zdogbrevean, C.; Quandt, A.; Fehske, H. *Physical Review B* **2011**, *83*, 045414.

(12)   Park, J.; Mitchel, W. C.; Brown, G. J.; Elhamri, S.; Grazulis, L.; Smith, H. E.; Pacley, S. D.; Boeckl, J. J.; Eyink, K. G.; Mou, S.; Tomich, D. H.; Hoelscher, J. E. *Applied Physics Letters* **2011**, *98*, 203102.

(13)   Shinde, P. P.; Kumar, V. *Physical Review B* **2011**, *84*, 125401.

(14)   Gorjizadeh, N.; Kawazoe, Y. *Journal of Nanomaterials* **2010**, *2010*, 513501.

(15)   Zhou, S. Y.; Gweon, G. H.; Fedorov, A. V.; First, P. N.; de Heer, W. A.; Lee, D. H.; Guinea, F.; Castro Neto, A. H.; Lanzara, A. *Nat Mater* **2007**, *6*, 770.

(16)   Kang, Y.-J.; Kang, J.; Chang, K. J. *Physical Review B* **2008**, *78*, 115404.

(17)   Giovannetti, G.; Khomyakov, P. A.; Brocks, G.; Kelly, P. J.; van den Brink, J. *Physical Review B* **2007**, *76*, 073103.

(18)   Xia, F.; Farmer, D. B.; Lin, Y.-m.; Avouris, P. *Nano Letters* **2010**, *10*, 715.

(19)   Balu, R.; Zhong, X.; Pandey, R.; Karna, S. P. *Applied Physics Letters* **2012**, *100*, 052104.

(20)   Ramasubramaniam, A.; Naveh, D.; Towe, E. *Nano Letters* **2011**, *11*, 1070.

(21)   Sławińska, J.; Zasada, I.; Klusek, Z. *Physical Review B* **2010**, *81*, 155433.

(22)   Dean, C. R.; Young, A. F.; MericI; LeeC; WangL; SorgenfreiS; WatanabeK; TaniguchiT; KimP; Shepard, K. L.; HoneJ *Nat Nano* **2010**, *5*, 722.

(23)   Xue, J.; Sanchez-Yamagishi, J.; Bulmash, D.; Jacquod, P.; Deshpande, A.; Watanabe, K.; Taniguchi, T.; Jarillo-Herrero, P.; LeRoy, B. J. *Nat Mater* **2011**, *10*, 282.

(24)   Sachs, B.; Wehling, T. O.; Katsnelson, M. I.; Lichtenstein, A. I. *Physical Review B* **2011**, *84*, 195414.

(25)   Sakai, Y.; Koretsune, T.; Saito, S. *Physical Review B* **2011**, *83*, 205434.

(26)   Nitzan, A.; Ratner, M. A. *Science* **2003**, *300*, 1384.

(27)   He, H.; Pandey, R.; Karna, S. P. *Nanotechnology* **2008**, *19*, 505203.

(28)   Ravindran, S.; Chaudhary, S.; Colburn, B.; Ozkan, M.; Ozkan, C. S. *Nano Letters* **2003**, *3*, 447.

(29)   Pasupathy, A. N.; Bialczak, R. C.; Martinek, J.; Grose, J. E.; Donev, L. A. K.; McEuen, P. L.; Ralph, D. C. *Science* **2004**, *306*, 86.

(30)   He, H.; Pandey, R.; Karna, S. P. *Chemical Physics Letters* **2007**, *439*, 110.

(31)   Joachim, C.; Gimzewski, J. K.; Schlittler, R. R.; Chavy, C. *Physical Review Letters* **1995**, *74*, 2102.

(32)   Kroto, H. W.; Heath, J. R.; O'Brien, S. C.; Curl, R. F.; Smalley, R. E. *Nature* **1985**, *318*, 162.

(33)   Oshiyama, A.; Saito, S.; Hamada, N.; Miyamoto, Y. *J. Phys. Chem. Solids* **1992**, *53*, 1457.

(34)   Ma, D. D. D.; Lee, C. S.; Au, F. C. K.; Tong, S. Y.; Lee, S. T. *Science* **2003**, *299*, 1874.

(35)   Rurali, R. *Reviews of Modern Physics* **2010**, *82*, 427.

(36)   Wu, Y.; Cui, Y.; Huynh, L.; Barrelet, C. J.; Bell, D. C.; Lieber, C. M. *Nano Letters* **2004**, *4*, 433.

(37)   Byon, K.; Tham, D.; Fischer, J. E.; Johnson, A. T. *Applied Physics Letters* **2005**, *87*.

(38)   Bunimovich, Y. L.; Shin, Y. S.; Yeo, W.-S.; Amori, M.; Kwong, G.; Heath, J. R. *Journal of the American Chemical Society* **2006**, *128*, 16323.

(39)   Fan, W.; Zhang, R. Q.; Rocha, A. R.; Sanvito, S. *J. Chem. Phys.* **2008**, *129*.

(40)   Chen, K.-I.; Li, B.-R.; Chen, Y.-T. *Nano Today* **2011**, *6*, 131.

(41)   Chiesa, M.; Cardenas, P. P.; Otón, F.; Martinez, J.; Mas-Torrent, M.; Garcia, F.; Alonso, J. C.; Rovira, C.; Garcia, R. *Nano Letters* **2012**, *12*, 1275.

(42)   Patolsky, F.; Lieber, C. M. *Materials Today* **2005**, *8*, 20.

(43)   Cui, Y.; Wei, Q.; Park, H.; Lieber, C. M. *Science* **2001**, *293*, 1289.

(44)   Patolsky, F.; Zheng, G.; Lieber, C. M. *Nat. Protocols* **2006**, *1*, 1711.

(45)   Szabo, A.; Ostlund, N. S. *Modern quantum chemistry: introduction to advanced electronic structure theory*; Dover Publications, 1996.

(46)   Dion, M.; Rydberg, H.; Schröder, E.; Langreth, D. C.; Lundqvist, B. I. *Physical Review Letters* **2004**, *92*, 246401.

(47)   Román-Pérez, G.; Soler, J. M. *Physical Review Letters* **2009**, *103*, 096102.

(48)   Runge, E.; Gross, E. K. U. *Physical Review Letters* **1984**, *52*, 997.

(49)   Hohenberg, P.; Kohn, W. *Physical Review* **1964**, *136*, B864.

(50)   Kohn, W.; Sham, L. J. *Physical Review* **1965**, *140*, A1133.

(51)   Parr, R. G.; Weitao, Y. *Density-functional theory of atoms and molecules*; Oxford University Press, USA, 1994; Vol. 16.

(52)   Capelle, K. *Brazilian Journal of Physics* **2006**, *36*, 1318.

(53)   Perdew, J. P.; Burke, K.; Ernzerhof, M. *Physical Review Letters* **1996**, *77*, 3865.

(54)   Becke, A. D. *The Journal of Chemical Physics* **1993**, *98*, 1372.

(55)   Datta, S. *Electronic transport in mesoscopic systems*; Cambridge university press, 1997.

(56)   José, M. S.; et al. *Journal of Physics: Condensed Matter* **2002**, *14*, 2745.

(57)   Brandbyge, M.; Mozos, J.; eacute; Luis; Ordej; oacute; n, P.; Taylor, J.; Stokbro, K. *Physical Review B* **2002**, *65*, 165401.

(58)   Louie, S. G.; Froyen, S.; Cohen, M. L. *Physical Review B* **1982**, *26*, 1738.

(59)   Junquera, J.; Zimmer, M.; Ordej; oacute; n, P.; Ghosez, P. *Physical Review B* **2003**, *67*, 155327.

(60)   Rocha, A. R.; Garcia-suarez, V. M.; Bailey, S. W.; Lambert, C. J.; Ferrer, J.; Sanvito, S. *Nat Mater* **2005**, *4*, 335.

(61)   http://invsee.asu.edu/nmodules/engmod/propwf.html.

(62)   Zhao, J.; Zeng, C.; Cheng, X.; Wang, K.; Wang, G.; Yang, J.; Hou, J. G.; Zhu, Q. *Physical Review Letters* **2005**, *95*, 045502.

(63)   Zou, Y. J.; Zhang, X. W.; Li, Y. L.; Wang, B.; Yan, H.; Cui, J. Z.; Liu, L. M.; Da, D. A. *Journal of Materials Science* **2002**, *37*, 1043.

(64)   Rockenbauer, A.; Csányi, G.; Fülöp, F.; Garaj, S.; Korecz, L.; Lukács, R.; Simon, F.; Forró, L.; Pekker, S.; Jánossy, A. *Physical Review Letters* **2005**, *94*, 066603.

(65)   Andreoni, W.; Gygi, F.; Parrinello, M. *Chemical Physics Letters* **1992**, *190*, 159.

(66)   Wang, S.-H.; Chen, F.; Fann, Y. C.; Kashani, M.; Malaty, M.; Jansen, S. A. *The Journal of Physical Chemistry* **1995**, *99*, 6801.

(67)   Andreoni, W.; Curioni, A.; Holczer, K.; Prassides, K.; Keshavarz-K, M.; Hummelen, J.-C.; Wudl, F. *Journal of the American Chemical Society* **1996**, *118*, 11335.

(68)   Saunders, M.; Jiménez-Vázquez, H. A.; Cross, R. J.; Poreda, R. J. *Science* **1993**, *259*, 1428.

(69)   Shinohara, H. *Reports on Progress in Physics* **2000**, *63*, 843.

(70)   Barajas-Barraza, R. E.; Guirado-Lopez, R. A. *The Journal of Chemical Physics* **2009**, *130*, 234706.

(71)   Feyereisen, M.; Gutowski, M.; Simons, J.; Almlof, J. *The Journal of Chemical Physics* **1992**, *96*, 2926.

(72)   Lin, F.; Sørensen, E. S.; Kallin, C.; Berlinsky, A. J. *Physical Review B* **2007**, *75*, 075112.

(73)   Park, H.; Park, J.; Lim, A. K. L.; Anderson, E. H.; Alivisatos, A. P.; McEuen, P. L. *Nature* **2000**, *407*, 57.

(74)   Nakanishi, S.; Tsukada, M. *Physical Review Letters* **2001**, *87*, 126801.

(75)   Taylor, J.; Guo, H.; Wang, J. *Physical Review B* **2001**, *63*, 121104.

(76)   Lau, K. C.; Pandey, R.; Pati, R.; Karna, S. P. *Applied Physics Letters* **2006**, *88*, 212111.

(77)   Zhang, X.-J.; Long, M.-Q.; Chen, K.-Q.; Shuai, Z.; Wan, Q.; Zou, B. S.; Zhang, Y. *Applied Physics Letters* **2009**, *94*, 073503.

(78)   Jiao, L.; Zhang, L.; Wang, X.; Diankov, G.; Dai, H. *Nature* **2009**, *458*, 877.

(79)   Han, M. Y.; Ouml; zyilmaz, B.; Zhang, Y.; Kim, P. *Physical Review Letters* **2007**, *98*, 206805.

(80)   Li, X. L.; Wang, X. R.; Zhang, L.; Lee, S. W.; Dai, H. J. *Science* **2008**, *319*, 1229.

(81)   Oostinga, J. B.; Heersche, H. B.; Liu, X.; Morpurgo, A. F.; Vandersypen, L. M. K. *Nat Mater* **2008**, *7*, 151.

(82)   Szafranek, B. N.; Schall, D.; Otto, M.; Neumaier, D.; Kurz, H. *Applied Physics Letters* **2010**, *96*.

(83)   Sai-Kong, C.; Dawei, S.; Kai-Tak, L.; Samudra, G. S.; Gengchiau, L. *Electron Devices, IEEE Transactions on* **2010**, *57*, 3144.

(84)   Lin, Y. M.; Avouris, P. *Nano Letters* **2008**, *8*, 2119.

(85)   Son, Y.-W.; Cohen, M. L.; Louie, S. G. *Physical Review Letters* **2006**, *97*, 216803.

(86)   Barraza-Lopez, S.; Vanević, M.; Kindermann, M.; Chou, M. Y. *Physical Review Letters* **2010**, *104*, 076807.

(87)   Wang, X.; Ouyang, Y.; Li, X.; Wang, H.; Guo, J.; Dai, H. *Physical Review Letters* **2008**, *100*, 206803.

(88)   Wakabayashi, K.; Takane, Y.; Yamamoto, M.; Sigrist, M. *New J. Phys.* **2009**, *11*.

(89)   Chen, J.-c.; et al. *Journal of Physics: Condensed Matter* **2010**, *22*, 035301.

(90)   Li, T., S.; Huang, Y., C.; Chang, S., C.; Chuang, Y., C.; Lin, M., F. *Eur. Phys. J. B* **2008**, *64*, 73.

(91)   Bhattacharya, S.; Mahapatra, S. *Physics Letters A* **2010**, *374*, 2850.

(92)   Ceperley, D. M.; Alder, B. J. *Physical Review Letters* **1980**, *45*, 566.

(93)   Perdew, J. P.; Zunger, A. *Physical Review B* **1981**, *23*, 5048.

(94)   Trickey, S. B.; uuml; ller-Plathe, F.; Diercksen, G. H. F.; Boettger, J. C. *Physical Review B* **1992**, *45*, 4460.

(95)   Marini, A.; Garc; iacute; a, G.; aacute; lez, P.; Rubio, A. *Physical Review Letters* **2006**, *96*, 136404.

(96)   Yang, L.; Park, C.-H.; Son, Y.-W.; Cohen, M. L.; Louie, S. G. *Physical Review Letters* **2007**, *99*, 186801.

(97)   Lee, H.; Son, Y.-W.; Park, N.; Han, S.; Yu, J. *Physical Review B* **2005**, *72*, 174431.

(98)   Wassmann, T.; Seitsonen, A. P.; Saitta, A. M.; Lazzeri, M.; Mauri, F. *Physical Review Letters* **2008**, *101*, 096402.

(99)   Saxena, S.; Tyson, T. A. *Carbon* **2010**, *48*, 1153.

(100)   Barone, V.; Hod, O.; Scuseria, G. E. *Nano Letters* **2006**, *6*, 2748.

(101)   Sahu, B.; Min, H.; MacDonald, A. H.; Banerjee, S. K. *Physical Review B* **2008**, *78*, 045404.

(102)   Lima, M. P.; Fazzio, A.; da Silva, A. J. R. *Physical Review B* **2009**, *79*, 153401.

(103)   Guo, Y.; Guo, W.; Chen, C. *The Journal of Physical Chemistry C* **2010**, *114*, 13098.

(104)   Pinto, H.; Jones, R.; Goss, J. P.; Briddon, P. R. *Physical Review B* **2010**, *82*, 125407.

(105)   Sun, S.-J.; Chang, C., P. *Eur. Phys. J. B* **2008**, *64*, 249.

(106)   Liu, Z.; Suenaga, K.; Harris, P. J. F.; Iijima, S. *Physical Review Letters* **2009**, *102*, 015501.

(107)   Mattausch, A.; Pankratov, O. *Physical Review Letters* **2007**, *99*, 076802.

(108)   Varchon, F.; Feng, R.; Hass, J.; Li, X.; Nguyen, B. N.; Naud, C.; Mallet, P.; Veuillen, J. Y.; Berger, C.; Conrad, E. H.; Magaud, L. *Physical Review Letters* **2007**, *99*, 126805.

(109)   Shemella, P.; Nayak, S. K. *Applied Physics Letters* **2009**, *94*, 032101.

(110)   Slawinska, J.; Zasada, I.; Klusek, Z. *Physical Review B* **2010**, *81*, 155433.

(111)   Mohr, M.; Papagelis, K.; Maultzsch, J.; Thomsen, C. *Physical Review B* **2009**, *80*, 205410.

(112)   Gui, G.; Li, J.; Zhong, J. *Physical Review B* **2008**, *78*, 075435.

(113)   Huang, M.; Yan, H.; Chen, C.; Song, D.; Heinz, T. F.; Hone, J. *Proceedings of the National Academy of Sciences* **2009**, *106*, 7304.

(114)   SanchezPortal, D.; Ordejon, P.; Artacho, E.; Soler, J. M. *Int. J. Quantum Chem.* **1997**, *65*, 453.

(115)   Troullier, N.; Martins, J. L. *Physical Review B* **1991**, *43*, 1993.

(116)   Novoselov, K. S.; Geim, A. K.; Morozov, S. V.; Jiang, D.; Katsnelson, M. I.; Grigorieva, I. V.; Dubonos, S. V.; Firsov, A. A. *Nature* **2005**, *438*, 197.

(117)   Kotakoski, J.; Jin, C. H.; Lehtinen, O.; Suenaga, K.; Krasheninnikov, A. V. *Physical Review B* **2010**, *82*, 113404.

(118)   Li, J.; Gui, G.; Zhong, J. *Journal of Applied Physics* **2008**, *104*, 094311.

(119)   Averill, F. W.; Morris, J. R.; Cooper, V. R. *Physical Review B* **2009**, *80*, 195411.

(120)   Topsakal, M.; Akt; uuml; rk, E.; Ciraci, S. *Physical Review B* **2009**, *79*, 115442.

(121)   Azevedo, S.; et al. *Nanotechnology* **2007**, *18*, 495707.

(122)   Azevedo, S.; Kaschny, J. R.; de Castilho, C. M. C.; Mota, F. D. *Eur. Phys. J. B* **2009**, *67*, 507.

(123)   Pease, R. S. *Acta Crystallographica* **1952**, *5*, 356.

(124)   McCann, E.; Fal'ko, V. I. *Physical Review Letters* **2006**, *96*, 086805.

(125)   Ohta, T.; Bostwick, A.; Seyller, T.; Horn, K.; Rotenberg, E. *Science* **2006**, *313*, 951.

(126)   Gauster, W. B.; Fritz, I. J. *Journal of Applied Physics* **1974**, *45*, 3309.

(127)   Liu, Z.; Song, L.; Zhao, S.; Huang, J.; Ma, L.; Zhang, J.; Lou, J.; Ajayan, P. M. *Nano Letters* **2011**, *11*, 2032.

(128)   Tang, S.; Ding, G.; Xie, X.; Chen, J.; Wang, C.; Ding, X.; Huang, F.; Lu, W.; Jiang, M. *Carbon* **2012**, *50*, 329.

(129)   Britnell, L.; Gorbachev, R. V.; Jalil, R.; Belle, B. D.; Schedin, F.; Mishchenko, A.; Georgiou, T.; Katsnelson, M. I.; Eaves, L.; Morozov, S. V.; Peres, N. M. R.; Leist, J.; Geim, A. K.; Novoselov, K. S.; Ponomarenko, L. A. *Science* **2012**, *335*, 947.

(130)   Padilha, J. E.; Pontes, R. B.; Fazzio, A. *Journal of Physics: Condensed Matter* **2012**, *24*, 075301.

(131)   Lui, C. H.; Li, Z.; Mak, K. F.; Cappelluti, E.; Heinz, T. F. *Nat Phys* **2011**, *7*, 944.

(132)   Bao, W.; Jing, L.; Velasco, J.; Lee, Y.; Liu, G.; Tran, D.; Standley, B.; Aykol, M.; Cronin, S. B.; Smirnov, D.; Koshino, M.; McCann, E.; Bockrath, M.; Lau, C. N. *Nat Phys* **2011**, *7*, 948.

(133)   Tang, K.; Qin, R.; Zhou, J.; Qu, H.; Zheng, J.; Fei, R.; Li, H.; Zheng, Q.; Gao, Z.; Lu, J. *The Journal of Physical Chemistry C* **2011**, *115*, 9458.

(134)   Sławińska, J.; Zasada, I.; Kosiński, P.; Klusek, Z. *Physical Review B* **2010**, *82*, 085431.

(135)   Quhe, R.; Zheng, J.; Luo, G.; Liu, Q.; Qin, R.; Zhou, J.; Yu, D.; Nagase, S.; Mei, W.-N.; Gao, Z.; Lu, J. *NPG Asia Mater* **2012**, *4*, e6.

(136)   Langreth, D. C.; et al. *Journal of Physics: Condensed Matter* **2009**, *21*, 084203.

(137)   Kleis, J.; Schröder, E.; Hyldgaard, P. *Physical Review B* **2008**, *77*, 205422.

(138)   Pereira, V. M.; Castro Neto, A. H.; Peres, N. M. R. *Physical Review B* **2009**, *80*, 045401.

(139)   Ribeiro, R. M.; Pereira, V. M.; Peres, N. M. R.; Briddon, P. R.; Neto, A. H. C. *New J. Phys.* **2009**, *11*, 115002.

(140)   Giovannetti, G.; Khomyakov, P. A.; Brocks, G.; Karpan, V. M.; van den Brink, J.; Kelly, P. J. *Physical Review Letters* **2008**, *101*, 026803.

(141)   Vanin, M.; Mortensen, J. J.; Kelkkanen, A. K.; Garcia-Lastra, J. M.; Thygesen, K. S.; Jacobsen, K. W. *Physical Review B* **2010**, *81*, 081408.

(142)   Hamada, I.; Otani, M. *Physical Review B* **2010**, *82*, 153412.

(143)   Laskowski, R.; Blaha, P.; Schwarz, K. *Physical Review B* **2008**, *78*, 045409.

(144)   Saha, S. K.; Waghmare, U. V.; Krishnamurthy, H. R.; Sood, A. K. *Physical Review B* **2008**, *78*, 165421.

(145)   Zacharia, R.; Ulbricht, H.; Hertel, T. *Physical Review B* **2004**, *69*, 155406.

(146)   Benedict, L. X.; Chopra, N. G.; Cohen, M. L.; Zettl, A.; Louie, S. G.; Crespi, V. H. *Chemical Physics Letters* **1998**, *286*, 490.

(147)   Stradi, D.; Barja, S.; iacute; az, C.; Garnica, M.; Borca, B.; Hinarejos, J. J.; aacute; nchez-Portal, D.; Alcam; M.; Arnau, A.; zquez de Parga, A. L.; Miranda, R.; Mart; n, F. *Physical Review Letters* **2011**, *106*, 186102.

(148)   Busse, C.; Lazicacute, P.; Djemour, R.; Coraux, J.; Gerber, T.; Atodiresei, N.; Caciuc, V.; Brako, R.; N'Diaye, A. T.; Bl; uuml; gel, S.; Zegenhagen, J.; ouml; rg; Michely, T. *Physical Review Letters* **2011**, *107*, 036101.

(149)   Slstrokawinacuteska, J.; Dabrowski, P.; Zasada, I. *Physical Review B* **2011**, *83*, 245429.

(150)   Müller-Dethlefs, K.; Hobza, P. *Chemical Reviews* **1999**, *100*, 143.

(151)   Zhong, X.; Pandey, R.; Karna, S. P. *unpublished* **2012**.

(152)   Yan, J.-A.; Ruan, W. Y.; Chou, M. Y. *Physical Review B* **2008**, *77*, 125401.

(153)   Zhang, Y.; Tang, T.-T.; Girit, C.; Hao, Z.; Martin, M. C.; Zettl, A.; Crommie, M. F.; Shen, Y. R.; Wang, F. *Nature* **2009**, *459*, 820.

(154)   Wu, B.-R. *Applied Physics Letters* **2011**, *98*, 263107.

(155)   Yuan, G. D.; Zhou, Y. B.; Guo, C. S.; Zhang, W. J.; Tang, Y. B.; Li, Y. Q.; Chen, Z. H.; He, Z. B.; Zhang, X. J.; Wang, P. F.; Bello, I.; Zhang, R. Q.; Lee, C. S.; Lee, S. T. *ACS Nano* **2010**, *4*, 3045.

(156)   Yang, X. B.; Guo, C. S.; Zhang, R. Q. *Applied Physics Letters* **2009**, *95*, 193105.

(157)   Gowtham, S.; Scheicher, R. H.; Ahuja, R.; Pandey, R.; Karna, S. P. *Physical Review B* **2007**, *76*, 033401.

(158)   Gowtham, S.; Scheicher, R. H.; Pandey, R.; Karna, S. P.; Ahuja, R. *Nanotechnology* **2008**, *19*, 125701.

(159)   Espejo, C.; Rey-González, R. R. *Stabilization and interaction energies of non planar DNA base pairs Guanine-Cytosine and Adenine-Thymine. A study based on the SIESTA method*; Revista Mexicana De Física S: Mexico, MEXIQUE, 2007; Vol. 53.

(160)   Sponer, J.; Hobza, P. *The Journal of Physical Chemistry* **1994**, *98*, 3161.

(161)   Nolan, M.; O'Callaghan, S.; Fagas, G.; Greer, J. C.; Frauenheim, T. *Nano Letters* **2006**, *7*, 34.

(162)   Mukhopadhyay, S.; Gowtham, S.; Scheicher, R. H.; Pandey, R.; Karna, S. P. *Nanotechnology* **2010**, *21*, 165703.

(163)   Monti, S.; Prampolini, G.; Barone, V. *The Journal of Physical Chemistry C* **2011**, *115*, 9146.

(164)   Monti, S.; Cacelli, I.; Ferretti, A.; Prampolini, G.; Barone, V. *The Journal of Physical Chemistry B* **2010**, *114*, 8341.

(165)   Yeh, C.-Y.; Zhang, S. B.; Zunger, A. *Physical Review B* **1994**, *50*, 14405.